

2008

## Femtosecond laser micromachining technology, materials processing and evaluation

George Logan DesAutels  
*University of Dayton*

Follow this and additional works at: [https://ecommons.udayton.edu/graduate\\_theses](https://ecommons.udayton.edu/graduate_theses)

---

### Recommended Citation

DesAutels, George Logan, "Femtosecond laser micromachining technology, materials processing and evaluation" (2008). *Graduate Theses and Dissertations*. 2303.  
[https://ecommons.udayton.edu/graduate\\_theses/2303](https://ecommons.udayton.edu/graduate_theses/2303)

This Dissertation is brought to you for free and open access by the Theses and Dissertations at eCommons. It has been accepted for inclusion in Graduate Theses and Dissertations by an authorized administrator of eCommons. For more information, please contact [mschlange1@udayton.edu](mailto:mschlange1@udayton.edu), [ecommons@udayton.edu](mailto:ecommons@udayton.edu).

**Femtosecond Laser Micromachining Technology, Materials Processing  
and Evaluation**

Dissertation

Submitted to

The School of Engineering of the

UNIVERSITY OF DAYTON

In Partial Fulfillment of the Requirements for

The Degree

Doctor of Philosophy in Electro-Optics

By

G. Logan DesAutels

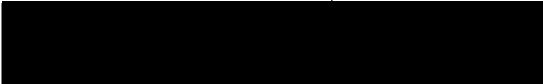
UNIVERSITY OF DAYTON

Dayton, Ohio

May 2008

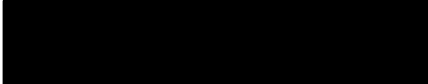
## **Femtosecond Laser Micromachining Technology, Materials Processing and Evaluation**

APPROVED BY:



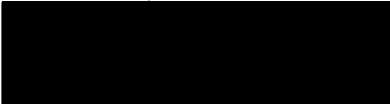
---

Peter E. Powers, Ph.D.  
Advisory Committee Chairman  
Associate Professor, Physics  
& Electro-Optics



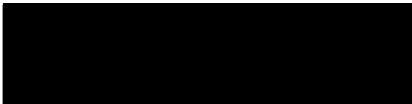
---

Christopher R. Brewer, Ph.D.  
Committee Member  
Technical Advisor  
AFRL/RXPJE, WPAFB, OH



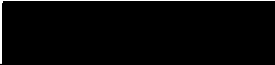
---

Mark A. Walker, Ph.D.  
Committee Member  
Technical Advisor  
AFRL/RXPJE, General Dynamics



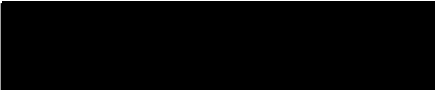
---

Leno M. Pedrotti, Ph.D.  
Committee Member  
Professor, Physics &  
Electro-Optics



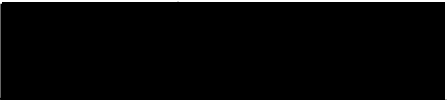
---

Andrew M. Sarangan, Ph.D.  
Committee Member  
Associate Professor, Electro-Optics



---

Malcolm Daniels, Ph.D.  
Associate Dean,  
School of Engineering



---

Joseph Saliba, Ph.D.  
Dean, School of Engineering

## **ABSTRACT**

### **Femtosecond Laser Micromachining Technology, Materials Processing and Evaluation**

Name: DesAutels, G. Logan  
University of Dayton May 2008

Advisor: Dr. Peter Powers

The commercialization of femtosecond lasers has brought nonlinear and micromachining research to a new level of practicality. The unique ability of femtosecond lasers to induce permanent index changes into just about any transparent material is due to fast focusing conditions, which results in the very high intensity needed for nonlinear multi-photon absorption. These index changes have brought about new techniques of micromachining in bulk materials for photonic and electronic (bulk semiconductors) applications alike. In addition, this technology has introduced new devices such as gratings, fiber Bragg gratings (FBGs), waveguides, photonic bandgap structures, and high temperature electronics in silicon carbide (SiC), just to name a few. Lastly, a plausible explanation of the differences of the formation of index changes in bulk crystalline and how it differs from bulk amorphous substrates is developed.

## ACKNOWLEDGEMENTS

This dissertation is dedicated to the two of the most important people in my life that had the most impact on my dream and success of obtaining my PhD. My father, George Leon Desautels (Big Guy), and for my wife, Kristen Elizabeth DesAutels both encouraged and believed in my success. My father was the first to introduce me to physics and continually celebrated in my success through the years from 1988 when I first took physics even with my near failing GPA. He would encourage, not pushed, me to enroll once or twice a year from 8<sup>th</sup> grade until my senior year of high school when I finally enrolled. Somehow he always knew what I would enjoy and what I would do well in. Sadly Big Guy passed on September 16, 2005 before he could witness my graduation so this work is devoted to his memory.

This work is also dedicated to my wife, Kristen, who has not only been enduring my work towards my PhD quest since 1995, but has been the one person in my life that truly believed in me, and undoubting knew I would eventually achieve my goal. Understandingly, I know that all my family, closest friends, co-workers, and professors were optimistic and encouraging me through the years, but Kris really believed, without doubt, that I would succeed. She deserves this dedication moreover for her tolerance for my often selfish obsession of improving my knowledge of physics/Electro-Optics for the pure sake of my love for science.

## TABLE OF CONTENTS

TABLE OF CONTENTS .....	v
LIST OF FIGURES .....	vii
LIST OF TABLES .....	xi
CHAPTER 1 .....	11
1.1 History.....	1
1.2 Femtosecond Pulse Generation.....	2
1.3 Femtosecond Pulse Theory .....	3
1.4 Silicon Carbide (SiC) Interest.....	8
1.2 Outline.....	8
CHAPTER 2 .....	9
2.1 Linear Properties of Samples Tested .....	10
2.2 Femtosecond Beam Characterization .....	21
2.3 Zscan Measurements of SiC .....	27
CHAPTER 3 .....	36
3.1 Lens Design .....	36
3.2 Experimental Setup.....	42
3.3 Threshold Measurements .....	43
3.4 High NA Sample Characterization .....	46
3.5 Grating Production.....	48
CHAPTER 4 .....	50
4.1 Optical Microscopy.....	50
4.2 Fourier Analysis.....	52
4.3 Diffraction Efficiency .....	55
CHAPTER 5 .....	70
5.1 Raman Spectroscopy.....	70
5.2 X-Ray Crystallography .....	81
5.3 Atomic Force Microscopy (AFM) .....	87
5.4 Near Field Scanning Optical Microscopy (NSOM).....	89
5.5 Transmission Electron Microscopy (TEM) .....	92
5.6 Index Modification Degradation over Time .....	99
5.7 Summary of Results.....	104
CHAPTER 6 .....	108
6.1 Introduction.....	108
6.2 Sample Mount Design.....	110
6.3 Experimental Setup.....	110
6.4 Theoretical Results.....	112
6.5 Experimental Results .....	114
6.6 SiC Volume Phase Grating .....	116
6.7 Conclusion .....	119
Appendix.....	120

I. Approximation of $\Delta n$ from Zscan Measurements .....	120
II. Focus Procedure .....	121
III. Error Analyses .....	125
IV. Energy Dispersive X-Ray Spectroscopy (EDS or EDAX) & Scanning Electron Microscope (SEM) .....	129
V. Publications .....	135
REFERENCES .....	136

## LIST OF FIGURES

Figure 1: Femtosecond schematic – above is a basic setup of the MOPA configuration, and below is a basic stretcher/amplifier/compression configuration. ....	3
Figure 2: This figure is an illustration done by Clark-MXR, Inc., which shows how a long pulse ablates away the substrate causing many micro-cracks, surface ripples and surface debris. ....	5
Figure 3: Here is an illustration done by Clark-MXR, Inc., which shows how short femtosecond pulse leaves the surface clean from micro-cracks, debris and no damage to the rest of the surface. ....	6
Figure 4: Illustrated here is how the index change to the substrate occurs at different locations in or on the substrate with different focus locations. ....	7
Figure 5: Images of 6H-SiC semi-insulating (left) and conducting (right) samples prior to micromachining. ....	12
Figure 6 UV-Vis results on semi-insulating and conducting SiC. ....	13
Figure 7: Transmission of SLG versus wavelength. ....	15
Figure 8: Images of SLG microscope slides prior to micromachining. ....	15
Figure 9: Zscan setup using three photocell detectors and a closed aperture (iris). ....	16
Figure 10: Zscan setup using a Dalsa CCD large array camera along with synthetic apertures. ....	17
Figure 11: An example of the $M^2$ for the femtosecond beam. ....	23
Figure 12: Beam profiles of four beams (from left to right): the clear aperture, a beam before the focus, the beam at focus, and a beam after focus with poor phase front causing a higher order spatial profile. ....	24
Figure 13: UV-NIR Ocean Optics spectrum of the Clark-MXR 2010 beam. ....	25
Figure 14: Pulse width of the femtosecond laser using the Clark-MXR auto-correlator. The small peak is only an artifact of the data acquisition software. ....	26
Figure 15: FS nonlinear $\beta$ and $n_2$ with an unexplained $\beta$ -signature. ....	30
Figure 16: The Corrected FS Zscan with the CCD array closer to the focus to eliminate the beam from walking off of the array. ....	31
Figure 17: On the Right is the normalized transmission for the open aperture and on the Left is the normalized transmission for the closed aperture both for the unprocessed SiC semi-insulating sample. The parameters used for this sample were energy of $3\mu\text{J}$ , a 750mm lens, and a 5.1mm entrance aperture. ....	32
Figure 18: Top is the Open ( $\beta$ ) and Closed ( $n_2$ ) Zscan of $E_1 = 40\mu\text{J}$ processed area of SiC, Middle is $E_2 = 20\mu\text{J}$ processed area, and on the Bottom is the $E_3 = 10\mu\text{J}$ processed area of SiC. ....	33
Figure 19: Nonlinear index of refraction in SiC SI as a function of applied fluence. ....	35
Figure 20: Zemax analytic views of the anamorphic lens used spread the focused beam elliptically. Top is a Zemax solid layout displaying each lens and their relative position in the lens tube (on the left is a 100mm focal in x, middle is a 50mm in y, and on the right is the spherical lens), and Bottom is a plot of the ray distribution through focus $\pm 400\mu\text{m}$ , where at defocus = $0\mu\text{m}$ is the anamorphic line shape used for laser processing. ....	39



Figure 21. Shown here is the geometrical Zemax theoretical $M^2$ ( <i>top chart</i> ), a zoomed in theoretical chart with linear fit ( <i>middle chart</i> ), and the experimental ( <i>bottom chart</i> ), which were used to determine the NA of each axis.....	41
Figure 22: Shown here are images of the mounted anamorphic lens in the experimental setup. ....	41
Figure 23: Optical setups for the damage threshold and Z-scan experiments. ....	42
Figure 24 On Top is a plot of the damage threshold (DT) for SiC semi-insulating (SI), SiC conducting, and Fused Silica (FS). On Bottom is the DT plot of SiC semi-insulating, SiC conducting, and FS as a function of fluence. The larger red data points represent where the visible damage begins.....	45
Figure 25 DT optical microscope results using Nomarski DIC and image processing for better viewing purposes for (left) semi-insulating SiC; (right) conducting SiC. Image processing was performed in order to better resolve the modified surface lines.....	47
Figure 26. (Top) SiC grating view with an optical microscope using Nomarski DIC for (left) semi-insulating SiC on a 10X magnification; (right) 50X magnification. (Bottom left) shows the surface of another SiC sample, and (bottom right) shows just 5 $\mu$ m below the surface. Image processing was performed in order to better resolve the modified surface lines.....	49
Figure 27: SLG grating structures view with the optical microscope. On the left is the actual 10x image for a 450 $\mu$ m x 450 $\mu$ m grating with a 10 $\mu$ m grating spacing, and a 3 $\mu$ m line thickness. On the right is the same grating after post image processing to better view the structure.....	51
Figure 28: Grating dimensions: A = 20 $\mu$ m, B = 190 $\mu$ m (consisting of 3 separate overlapped anamorphic lines), C = 3 $\mu$ m, D = 2-5 $\mu$ m, W = 500 $\mu$ m. ....	53
Figure 29: Top shows SiC grating diffraction pattern using a HeNe beam and viewed onto a business card, while Bottom shows the same image only with using the Cohu 4812 CCD camera and Spiricon software.....	57
Figure 30: Theoretical Fourier transform image and line out of the micromachined gratings.....	58
Figure 31: This figure depicts the input 632.8nm HeNe beam and the resulting SiC diffraction pattern of the first order. On the right is the 0-order beam and on the left is the first-order diffracted beam.....	59
Figure 32: (Top) DE versus fluence for 2, 6, 12, and 36 pulses, (Middle) DE versus grating spacing, and (Bottom) DE versus diffraction angle. The red data points (triangle) are the data that was filled in at a later date to verify the trends.....	63
Figure 33: Diffraction efficiency versus Fluence using 36 pulses comparing semi-insulating to conducting SiC.....	65
Figure 34: Discontinuous and continuous grating lines micro-machined in conducting SiC. Top two pictures, grating made using 36 pulses, and the bottom two pictures, grating made using a single pulse. ....	65
Figure 35: Transmission grating with index modulations at a given angle with respect to the input beam. This figure is provided by Barden <i>et al</i> .....	66
Figure 36: (Top) $\Delta n$ versus modulation depth, (Middle) $\Delta n$ versus diffraction efficiency, and (Bottom) zoom of the middle chart – $\Delta n$ versus $\eta$ . ....	69
Figure 37: University of Dayton Renishaw Micro-Raman system.....	71

Figure 38: University of Dayton Raman Spectra on semi-insulating processed and unprocessed SiC: (Top) Raman using 514nm laser source and a 1800 line grating with fluorescence emission causing a slope in the trend and false-broadening of two or three of the peaks, (Middle) is a new Raman scan with the instrument set to use a "photo-bleaching" technique to subtract the fluorescence emission, (Bottom) is a 6H-SiC Raman from Burton <i>et al</i> 6H-SiC Raman spectrum. ....	72
Figure 39: UD Raman of 6H-SiC processed grating subsurface structure and unprocessed regions illustrating peak shifts and broadening: from top to bottom: 150 $\text{cm}^{-1}$ peak, 500 $\text{cm}^{-1}$ peak, 766 $\text{cm}^{-1}$ and 788 $\text{cm}^{-1}$ peaks, and the 965 $\text{cm}^{-1}$ .....	76
Figure 40: Raman spectra in order from the list of possible chemical reactions in the processed SiC specimen. From top left to bottom: Si-Si, SiH, SiN, C=C, CN, CO, Graphite, and a 6H-SiC specimen with C-C reaction and also showing another common SiC peak at 1530. ....	78
Figure 41: Deformation of a crystal lattice that will cause a dislocation in the bulk medium, or an index of refraction change. This dislocation is seen in the center of the bottom image by tilting the page.....	80
Figure 42: SiC sample after being prepped for the x-ray crystallography test. (Left) is energies 1, 2, and 3 at 5x magnification, (middle) is energy 1 area at 20x magnification, and (right) is energy 1 area at 50x magnification. ....	82
Figure 43: UD Oxford Diffraction Xcalibur 3 x-ray diffractometer (XRD), or x-ray crystallography.....	83
Figure 44: Unprocessed SiC: in order from left to right – 0°, 5°, 10°, and 15° scans. Top is the raw images, middle is emboss-processed raw images, and bottom are histograms of the emboss images. ....	84
Figure 45: Processed SiC for $E_1 = 40\mu\text{J}$ area: in order from left to right – 0°, 5°, 10°, and 15° scans. Top is the raw images, middle is emboss-processed raw images, and bottom are histograms of the emboss images. ....	84
Figure 46: Processed SiC for $E_2 = 20\mu\text{J}$ area: in order from left to right – 0°, 5°, 10°, and 15° scans. Top is the raw images, middle is emboss-processed raw images, and bottom are histograms of the emboss images. ....	85
Figure 47: Processed SiC for $E_3 = 10\mu\text{J}$ area: in order from left to right – 0°, 5°, 10°, and 15° scans. Top is the raw images, middle is emboss-processed raw images, and bottom are histograms of the emboss images. ....	86
Figure 48: AFM illustrations from JPK Instruments <sup>35</sup> . ....	87
Figure 49: On the top shows the microscope DIC image of the semi-insulating SiC processed lines and AFM results of a 5.5 $\mu\text{m}$ wide and a 10nm raise surface modification on SI SiC material. On the bottom shows the DIC microscope image of the conducting SiC sample and AFM results of a 3.3 $\mu\text{m}$ wide and a 30nm trench surface modification. This figure is also shown previously. ....	88
Figure 50: (Left) is an example of a far-field imaging system, (Right) is an example of a near-field imaging system.....	90
Figure 51: SiC grating NSOM measurement setup. ....	90
Figure 52 (Left) is topography of the semi-insulating SiC sample, (Right) is the optical output revealing an index change. ....	91
Figure 53: Fixed beam TEM setup – drawing is not to scale. ....	92

Figure 54: Subsurface semi-insulating SiC with FIB preparation: (Left) 10x microscope image of the subsurface grating before FIB, (Right) 20x microscope image of the FIB processed area. ....	93
Figure 55: (Top) is the image of the surface grating TEM that is labeled to identify the key features of the TEM specimen. (Bottom Left & Right) are zoomed images of the labeled top image to give a better image of the processed area. ....	94
Figure 56: TEM of subsurface SiC grating line. ....	96
Figure 57: (Top) is the extra-ordinary and ordinary SiC crystal refraction indices plot as a function of wavelength, (Bottom) is a plot of the SiC crystal indices orientations. .	98
Figure 58: DE versus fluence for two times: Time 0 is when the DE was measured directly after writing the gratings, and Time 1 year is an approximate drop in $\eta$ by 2. ....	100
Figure 59: (Top) is an optical microscope image of a surface grating micromachined in SLG in 2005 and the same grating re-imaged in 2008, (Bottom) are the lineout results for each. ....	101
Figure 60: Subsurface SLG gratings: (Top) are the optical microscope images, (Bottom) are the lineout images. ....	102
Figure 61: Subsurface SiC gratings: (Top) are the optical microscope images, (Bottom) are the lineout images. ....	103
Figure 62: SiC sensor mount milled out of copper. ....	110
Figure 63: SiC temperature sensor experimental setup. ....	111
Figure 64: (Top) shows the deflection ( $\Delta x$ ) as a function of temperature, (bottom) shows the $\Delta x/x$ ratio as a function of temperature, which is a common way of displaying the material expansion. The charts show a max ~5% error bars. ....	115
Figure 65: Shown here is the 6H-SiC thermal coefficient as a function of temperature with maximum 5% error bars. The 2 <sup>nd</sup> order polynomial is given in Equation 49. ....	116
Figure 66: (Left) is the SiC grating at 10X magnification, and (Right) is the SiC grating after 50X magnification. The images were processed to view easier, and the images were obtained using Nomarski DIC on an optical microscope. ....	117
Figure 67: (Above) is the theoretical Fraunhofer diffraction pattern with a lineout of two of the orders, (Below) is the experimental Fraunhofer diffraction pattern with a lineout of two of the orders. ....	118
Figure 68: Focus test for a reflective sample with the assistance from an optical microscope to view increasing damage areas that represent focus position. ....	122
Figure 69: Transmission focus test setup. ....	123
Figure 70: Transmission test output to give an example of how the transmission (%) will vary as a function of focus distance (Z Position). ....	124
Figure 71: Chart of how the measured error for the coefficient of thermal expansion decreases as a function of temperature. ....	128
Figure 72: University of Dayton EDS system (Left) and SEM system (Right). ....	129
Figure 73: University of Dayton NEST Laboratory SEM (Left) and EDS (Right) images. ....	130
Figure 74: University of Dayton EDS results on the black (Top), gray (Middle), and white (Bottom) regions. ....	132

## LIST OF TABLES

Table 1: SiC sample characteristics for semi-insulating and conducting types. These values come from the vendor; semi-insulating SiC comes from Intrinsic Corp, and the conducting SiC comes from Cree Corp. ....	11
Table 2: Provided is the ordinary, $n_o$ , and extraordinary, $n_e$ , as well as the coefficient of linear expansion. ....	12
Table 3: Index of refraction and coefficient of linear expansion for SLG.....	14
Table 4: Nonlinear measurements resulting from the Z-scan experiment. Multiple energies were tested to provide a statistical average. ....	34
Table 5: The anamorphic lens prescription from Zemax.....	38
Table 6: NA values for theoretical and experimental results.....	40
Table 7: DT measured results for two lenses: 125mm focal and the anamorphic lens (High NA). ....	45
Table 8: Processed and unprocessed SiC peak analysis is shown for Figure 39. ....	76
Table 10: Results given for DE, Zscan, and $\Delta n$ measurements. ....	121
Table 11: Uncertainties listed for the DE experimental measured quantities.....	126
Table 12: Uncertainties listed for the SiC temperature sensor experimental measured quantities. ....	127
Table 13: Elements found in the EDS black, gray, white regions. ....	132

# CHAPTER 1

## Introduction

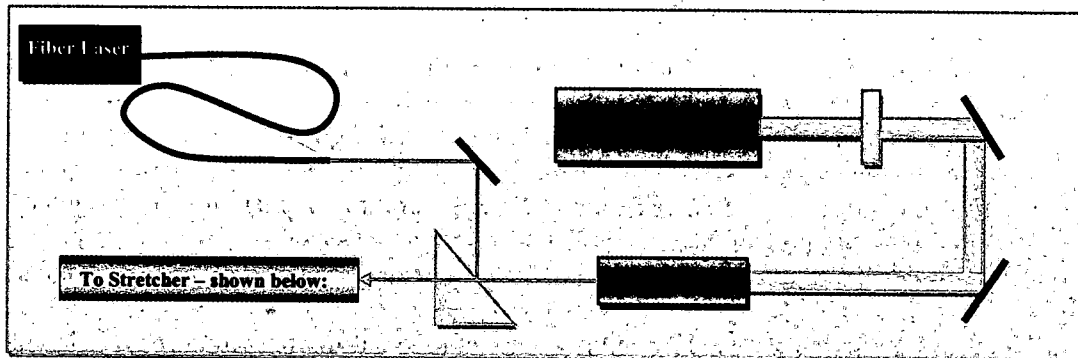
### 1.1 History

Previous researchers have theorized that an ultra-fast pulse is too short to interact at the molecular level, and instead interacts at the atomic electronic level.<sup>1</sup> Here the fs pulse displaces electrons permanently and/or causes lattice changes resulting in a modification to the index of refraction.<sup>2</sup> The modification to the index is localized to a very small volume depending on the NA and energy used. These index alterations can be on the surface or in most cases subsurface in bulk material.

In the early 1960s, upon the invention of the laser, the optics field has generated many new scientific areas, one of them being the femtosecond laser field and its applications. Femtosecond laser science has been a valuable tool for many scientific fields including biology, chemistry, electrical engineering, and optics. Since femtosecond laser pulses are so short, tremendously high peak intensities can be attained from relative low energies. The extremely high intensity is used for nonlinear interactions with atomic states as opposed to interaction at the molecular level as with long pulse (picoseconds) to CW lasers. In general, the femtosecond time regime has nonlinear response interactions with bulk transparent materials capable of producing useful and interesting light-matter interactions.

## 1.2 Femtosecond Pulse Generation

Like most femtosecond laser systems the Clark-MXR CPA 2010 laser system consists of, essentially, three laser systems used to create the amplified 775nm 150fs laser pulse. The femtosecond 775nm pulse derives from an Yb-doped fiber laser system that operates in the nJ-energy range. The output of the fiber laser is then seeded into a Ti-Sapphire crystal rod where a Nd-Yag laser system outputs a 1064nm mW beam that is then doubled to 532nm using a nonlinear BBO Crystal. The 532 YAG beam enters the Ti-Sapphire rod and creates a population inversion within the rod so that the fiber seed laser can benefit from the gain of the population inversion. This is essentially a Master Oscillator Power Amplifier (MOPA) configuration where the seed laser is amplified in the Ti-Sapphire gain medium. In short, the first laser is a fiber seed laser, the second is the Nd-Yag pump laser, and the third is the MOPA Ti-Sapphire configuration. Multiple passes are made through the Ti-Sapphire by the fiber seed laser with each pass adding to the optical gain. Each pass is done with a temporally stretched beam using a diffraction grating, and on the amplified seed laser's final pass, the stretched pulse is re-compressed just before exiting. This stretching/compression is performed to keep the short femtosecond amplified pulse from reaching the damage thresholds of certain optics in the optical train. The following figure gives an illustration of this process.



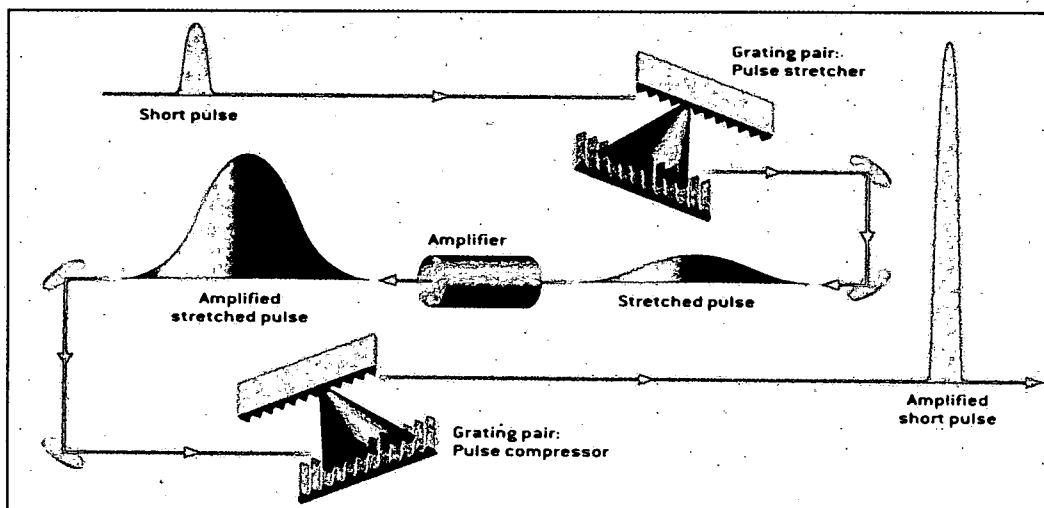


Figure 1.1: Femtosecond schematic – above is a basic setup of the MOPA configuration, and below is a basic stretcher/amplifier/compression configuration<sup>3</sup>.

Figure 1.1 shows a basic illustration of how a femtosecond laser system functions.

Above displays how the MOPA configuration of the seed pulse transpires. Below simply explains the amplification process of the seed pulse. For multiple passes through the Ti-Sapphire amplifier (or gain medium) a Q-switch is employed to precisely time when the Nd-YAG pulse excites the gain medium to when the fiber seed pulse arrives to exploit the gain medium's population inversion. The gratings (or a single grating in some cases) are engaged to stretch and compress the pulse to keep damage from occurring.

### 1.3 Femtosecond Pulse Theory

Micro-fabrication with femtosecond laser pulses has several unique characteristics, making it possible to construct extremely small and clean features within a bulk substrate. For short pulse beams,  $<1\text{ps}$ , the peak intensity is high enough for nonlinear plasma generation to occur through a combination of multi-photon and avalanche ionization<sup>4</sup>

Avalanche ionization is a process where a small number of “seed” free electrons (usually generated by multi-photon ionization) are accelerated by the light fields and acquire enough energy to ionize other bound electrons in the material. These electrons themselves are then accelerated and collide with more bound electrons and a cascade is produced. Laser machining using long pulse laser systems ( $\Delta\tau > 100\text{ps}$ ) rely on linear absorption of defect sites and sample dependent imperfections to create the first few free electrons. Thus, the breakdown threshold for these materials is very sample dependent with long pulses. This is not so for femtosecond pulses, since the first seed electrons are created by a nonlinear ionization, which can occur regardless of the presence of material defects.<sup>4</sup> Also, with the energy from longer pulse sources deposited over a much longer time than it takes for the electrons and the lattice to reach thermal equilibrium. Figure 1.2 is an illustration of what affect a long pulse has on a substrate.<sup>4</sup> Here micro-cracks, heat deposition and small collateral damage to the surrounding area occur with these sources that will spoil the structure quality. Typical heat diffusion time is on the order of nanoseconds to microseconds, and electron-phonon coupling time of most materials occurs in picoseconds to nanoseconds.<sup>4</sup>



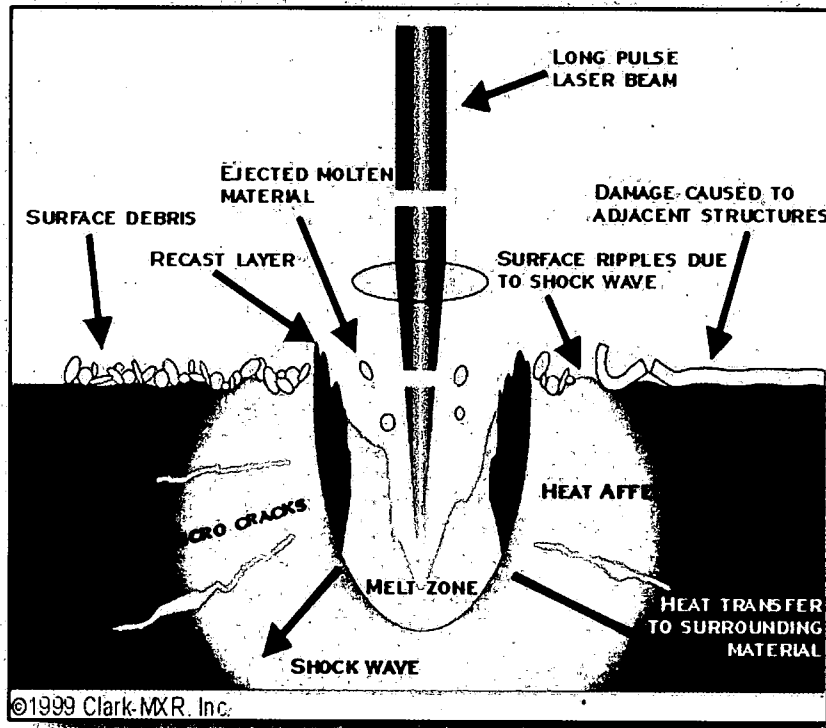


**Figure 1.2:** This figure is an illustration done by Clark-MXR, Inc., which shows how a long pulse ablates away the substrate causing many micro-cracks, surface ripples and surface debris.

However, in the femtosecond regime the ultrafast pulse leaves a very small “clean” area of localized damage or index change. Figure 1.3 shows an illustration of this, again, compliments of Clark-MXR.

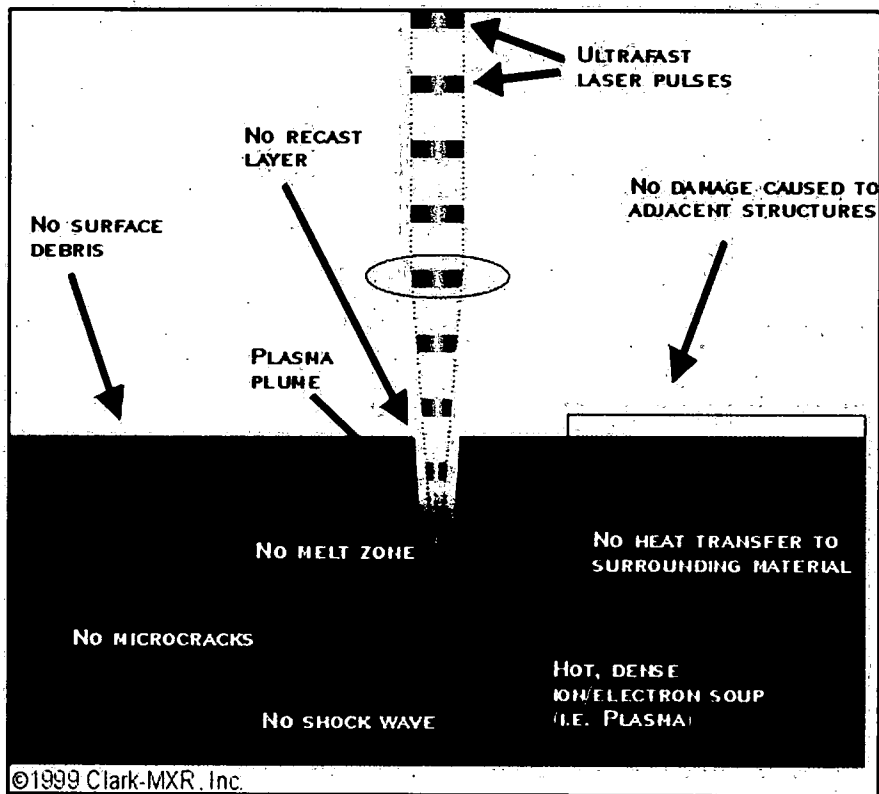


**Figure 1.3:** Here is an illustration done by Clark-MXR, Inc., which shows how short femtosecond pulse leaves the surface clean from micro-cracks, debris and no damage to the rest of the surface.

The short pulse energy is deposited into the material so fast that the material is forced into a plasma state, which then propagates away from the laser machining area as a high energetic gas. This energetic gas takes all (or most) of the heat away from the material's surface. The material, when hit with a femtosecond (fs) pulse, goes from a solid phase to gaseous expanding plasma while skipping a material-melting phase.<sup>4</sup> Therefore, the femtosecond time frame is much faster than heat transfer time and electron-phonon coupling times, and thus, the pulse is gone before heat buildup can occur. This process avoids any damage to the material, and leaves a high quality machined area.

If the energy is high enough and the focal length long enough, the fs pulse will form a channel through the substrate. On the other hand, if the energy is lowered and the focal length shortened small features can form either on or below the surface, as depicted in Figure 1.4 below. The small “clean” feature will only be preserved if the repetition rate of the laser is not too high,  $< 500\text{Hz}$ . If the repetition rate is too high then the average power will increase and, thus, the nonlinear absorption will also increase and start ablating the surface similar to a long pulse.

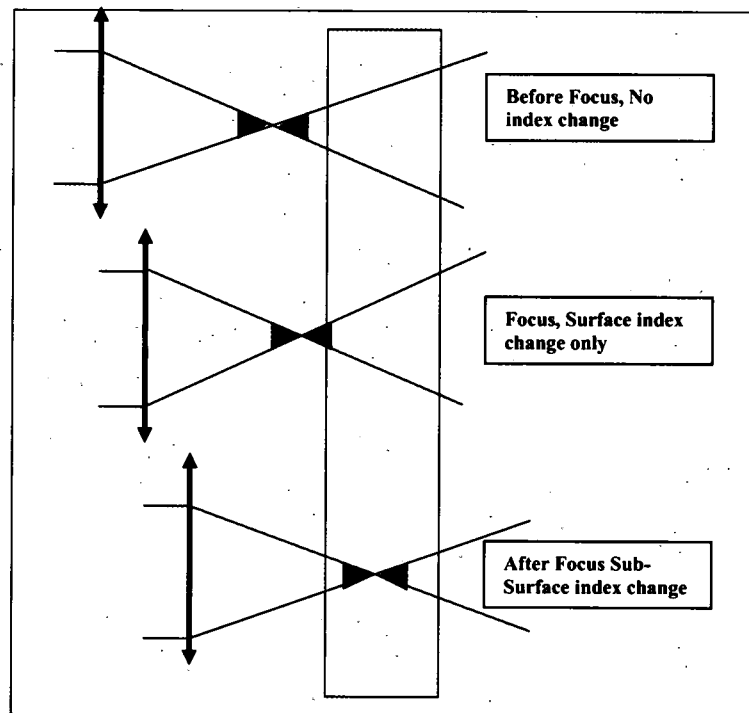


**Figure 1.4:** Illustrated here is how the index change to the substrate occurs at different locations in or on the substrate with different focus locations.

Changing the energy will have an identical affect, but it will not “move” the feature, only change its size. Because this is an intensity driven process, the damage threshold of the material is set and either the entire  $1/e^2$  diameter of the Gaussian is above that threshold or not. If not, then the diameter of the damage spot gets smaller because the material

“sees” less of the Gaussian profile. This concept seeds the new femtosecond micromachining technology used to generate micro-fabricated structures and photonic bandgap structures along with other micron and/or submicron features in bulk transparent materials.

#### **1.4 Silicon Carbide (SiC) Interest**

SiC is of interest for various reasons and was selected for this dissertation because of its significance to the Air Force. Silicon is typically used for many, if not all, electronics applications, but when silicon is combined with carbon it contributes hardness to silicon that gives it an attractive use in harsh environments. Some of the motivations for using SiC are listed here.

1. SiC is used in harsh environments where typical silicon would fail.
2. SiC has a high melting point that allows it to be in extreme hot environments such as aircraft engine components.
3. High-power high-voltage switching applications.
4. SiC is known to be difficult to process because of its hardness, therefore femtosecond laser processing is employed as an alternative to etching processes.
5. Laser processing is a clean and much simpler method; in addition, it is a faster process.

#### **1.2 Outline**

In this paper we exploit femtosecond laser technology to develop a new micromachining technique for manufacturing grating structures in SiC, create new devices arising from this innovative method, and add to the understanding of the physical mechanism behind index of refraction changes in bulk transparent substrates. Chapter 2

is a study on the linear and nonlinear material characterization for the samples chosen for this dissertation. Chapter 3 contains a description of the new technique and anamorphic lens design, and describes how this lens is used for grating formation. Chapter 4 is left to describe the performance and evaluation of the micromachined grating structures. In Chapter 5 the cause of the index change in transparent crystalline materials is studied using imaging techniques such as Raman spectroscopy, atomic force microscopy (AFM), and near field scanning optical microscopy (NSOM), TEM, EDAX, X-ray crystallography, optical microscopy, Nomarski optical microscopy, and a time study showing the degradation of processed structures in amorphous and crystalline materials. In Chapter 6 a SiC thermal sensor and a new technique for measuring the linear and nonlinear coefficient of thermal expansion of transparent and non-transparent materials are described. These applications are based on the principles described in the preceding chapters. Four papers have arisen from this research. The first is titled "Femtosecond Micromachining in Transparent Bulk Materials Using an Anamorphic Lens" and was published in Optics Express. The second is titled "Femtosecond Laser Threshold and Nonlinear Characterization in Bulk Transparent SiC Materials" and was published in JOSA B. The third is titled "Optical temperature sensor and thermal expansion measurement using a femtosecond micro-machined grating in 6H-SiC" and is soon to be published in Applied Optics. The fourth titled "Femtosecond Laser Processes in 6H-SiC Crystal to Understand the Cause of Index of Refraction Changes" will be submitted to Optics Letters. In addition to these papers, two conferences were attended with a presentation at the 2006 Great Lakes conference and a poster at 2007 Photonics West.

## **CHAPTER 2**

### **Linear and Nonlinear Material Characterization**

SiC is the primary focus of the characterizations in this dissertation since neither the linear or nonlinear properties of this material has been documented. In addition, the SiC material properties were measured to help understand the physics or morphology of the index changes in crystalline substrates. Furthermore, this chapter will discuss the theory pertaining to related to material characterization, and present of the linear and nonlinear properties of each material studied.

#### **2.1 Linear Properties of Samples Tested**

Three types of samples were tested in this research. Soda lime glass (SLG) was used primarily to align the setup and to generate a portion of the diffraction efficiency data as a function of grating spacing. The 6H-SiC semi-insulating (SI) and conducting samples were primarily interesting for their resistance to harsh environments and because of their crystalline makeup. Finally, fused silica (FS) was used only to calibrate our linear and nonlinear experiments since there is much reference data pertaining to these characterizations. FS will only be discussed when discussing calibration techniques.

##### **2.1.1 SiC Sample**

Femtosecond laser pulses were used to write volume phase gratings in bulk 6H semi-insulating and conducting Silicon Carbide (SiC); a wide bandgap semiconductor material

provided by Wright-Patterson AFB AFRL/MLPS.<sup>5</sup> As mentioned, SiC was chosen as the crystalline material for this study because it is an attractive alternative material for a variety of semiconductor devices where silicon (Si) lacks the environmental resistance that carbon furnishes when combined to Si.<sup>6</sup> These areas where SiC devices can be used include high-power high-voltage switching applications, high temperature electronics, and avionics where it is desired to keep sensitive Si-based electronics away from extreme environments onboard aircraft.<sup>6</sup> SiC is also resistant to wet chemical etching and alternative methods to bulk micromachining this material include deep reactive ion etching (DRIE) and reactive ion etching (RIE), which is the most direct micromachining method. These methods of processing SiC have issues related to masking or micro-masking for etching purposes, low etching rates, and an increase of processing steps<sup>7</sup>. The SiC samples tested were semi-insulating and conducting types; their characteristics are shown in Table 2.1 below. The samples in Table 2.1 were perpendicularly oriented on the c-plane with the vertically polarized anamorphic beam.

**Table 2.1: SiC sample characteristics for semi-insulating and conducting types. These values come from the vendor; semi-insulating SiC comes from Intrinsic Corp, and the conducting SiC comes from Cree Corp.**

Sample	Conductivity	Orientation	Dopant	Concentration (cm <sup>-3</sup> )	Resistivity (Ω·cm)	Thickness (μm)	Face	N or P Type
SiC semi-insulating	Semi-insulating	c-Plane, 6H 0° on axis	Undoped	~1x10 <sup>15</sup>	3x10 <sup>7</sup>	340	Si	---
SiC conducting	Conducting	c-Plane, 6H 0° on axis	Nitrogen	~2.5x10 <sup>17</sup>	0.05	220	Si	N

The refractive index of 6H-SiC is given using the Sellmeier equations by<sup>8</sup>

$$n_o = 2.55531 + 3.34 \times 10^4 \cdot \lambda^{-2} \quad \text{Equation 2.1}$$

$$n_e = 2.5852 + 3.68 \times 10^4 \cdot \lambda^{-2} \quad \text{Equation 2.2}$$

Where  $n_o$  and  $n_e$  are the ordinary and extra-ordinary indices given for 780nm and 633nm in Table 2.2. Another important 6H-SiC material characteristic for this study is the coefficient of linear expansion (CLE)<sup>9,10</sup> which is also given in Table 2.2.

**Table 2.2:** Provided is the ordinary,  $n_o$ , and extraordinary,  $n_e$ , as well as the coefficient of linear expansion.

Sample	$n_o$	$n_e$	CLE ( $\times 10^{-6}$ per °C)
6H-SiC Semi-insulating	2.610	2.610	3.5-4.5
6H-SiC Conducting	2.610	2.646	3.5-4.5
References	8	8	9, 10

Below are some images of the 6H-SiC semi-insulating and conducting samples prior to femtosecond micromachining.

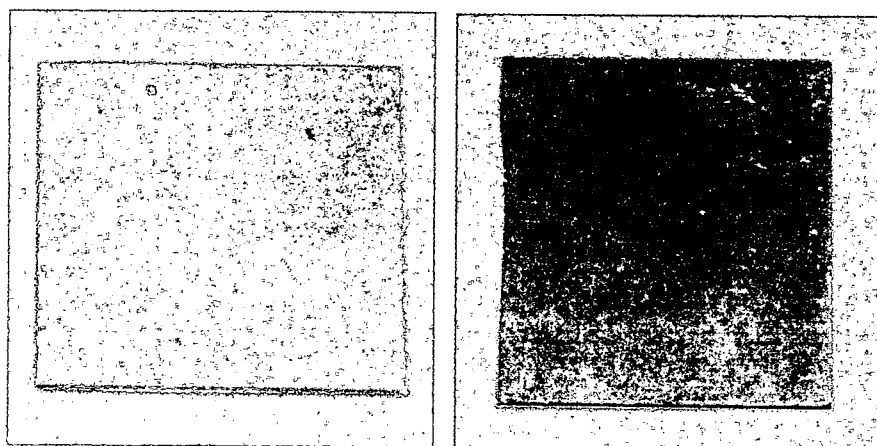


**Figure 2.1:** Images of 6H-SiC semi-insulating (left) and conducting (right) samples prior to micromachining.

In Figure 2.1 is the semi-insulating (SI) SiC and on the left is the conducting SiC samples. There is no visible way to distinguish the two samples; even the spectrums are very similar for the exception of the small dip in the conducting sample at approximately 630nm as shown in the UV-Vis later.



### 2.1.2 SiC UV-Vis

A UV-Vis study was carried out to understand the linear transmission and to confirm the provided bandgap information shown in Table 3.3 using a Varian Cary 50 UV-Vis spectrometer. This device uses a Xenon flash lamp and monochromatic optics to send a beam of varying wavelengths (300nm to 900nm) through the sample to measure its transmission. The results for each SiC sample are given in the figure below.

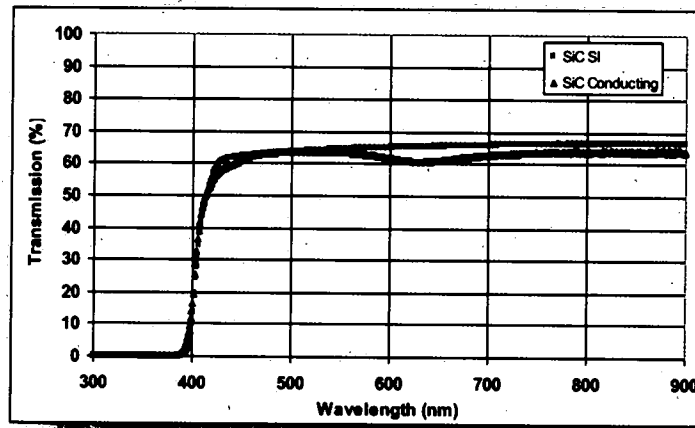


Figure 2.2 UV-Vis results on semi-insulating and conducting SiC.

From the UV-Vis results it demonstrates that both the semi-insulating and conducting SiC samples have a band edge at 400nm. Equation 12 below relates the cutoff wavelength of the SiC samples to the band gap in electron volts (eV).

$$\lambda = \frac{1239.8}{E(eV)} \quad \text{Equation 2.3}$$

Here, E is the energy with units of electron volts,  $\lambda$  is in units in nm, and Table 3.3 gives  $E = 3.1\text{eV}$ . Therefore,  $\lambda = 399.936\text{ nm}$  for both semi-insulating and conducting SiC, which is in agreement with the “turn on” wavelength in Figure 2.2. Furthermore, the conducting SiC sample has a dip centered at  $\sim 630\text{nm}$  that is consistent with multiple SiC

conducting samples tested. The dip is may be due to the absorption of the Nitrogen dopant present in the conducting SiC sample. The transmissions are around 65% to 70% for each semi-insulating and conducting sample, which agrees with the DT results that show a nonlinear transmission at close to zero fluence.

### 2.1.3 Soda Lime Glass Sample

Soda Lime Glass (SLG) was primarily used for alignment of the anamorphic lens and was also used to collect diffraction efficiency (DE) versus grating spacing, energy, and pulses. The SLG samples were microscope slides manufactured by Fisherbrand and containing the following chemical composition<sup>11</sup>:

73 SiO<sub>2</sub>, 14 Na<sub>2</sub>O, 9 CaO, 0.15 Al<sub>2</sub>O<sub>3</sub>, 0.03 K<sub>2</sub>O, 4 MgO, 0.02 TiO<sub>2</sub>, 0.1 Fe<sub>2</sub>O<sub>3</sub>. The index of refraction and linear coefficient of expansion for this material are provided in the table below, as well as the amorphous SLG has a transmission spectrum shown in Figure 2.3 below.

**Table 2.3: Index of refraction and coefficient of linear expansion for SLG.**

Sample	n	CLE (x10 <sup>-6</sup> per °C)
SLG	1.513	8.6
References	11	11

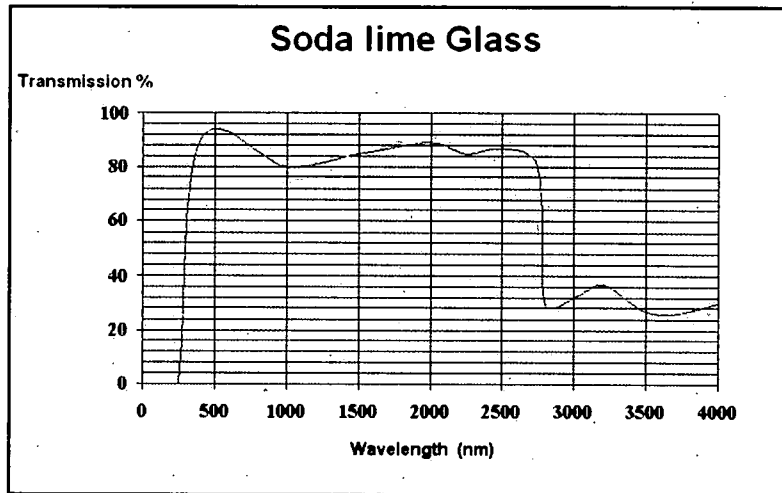


Figure 2.3: Transmission of SLG versus wavelength.



Figure 2.4: Images of SLG microscope slides prior to micromachining.

The SLG samples used are basic microscope slides and were used simply because they are inexpensive, ample, ~90% transmission, and are easily used in the setup. These SLG samples were also useful in assisting with the femtosecond beam analysis by finding beam focus, damage spot diameter verification, and general alignment.

### 2.1.4 Zscan Theory

The Z-scan technique involves moving a sample through focus of a lens and measuring the transmittance through a closed aperture as well as an open aperture. This technique is also described in CHAPTER 4, and an in depth mathematical analysis. This technique has become a standard for quickly measuring simultaneously two nonlinear optical parameters of the sample material:  $n_2$ , the nonlinear index of refraction which comes from the self-focusing property of the sample, and  $\beta$  the material's two-photon absorption (TPA) coefficient.

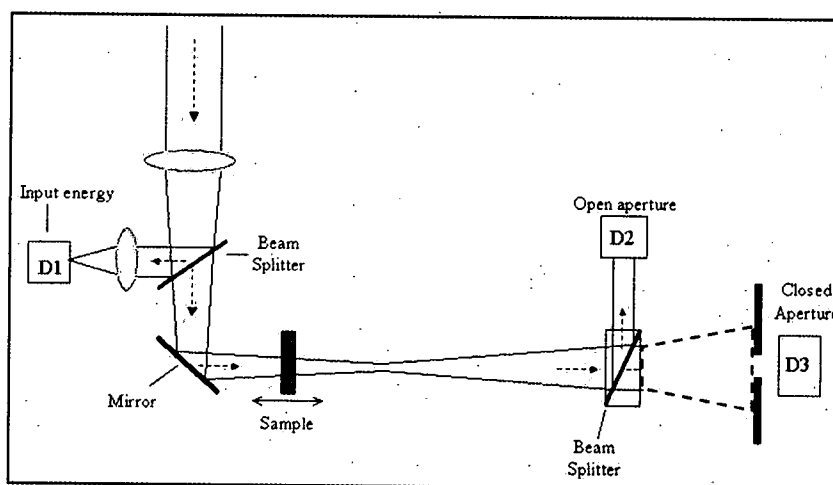
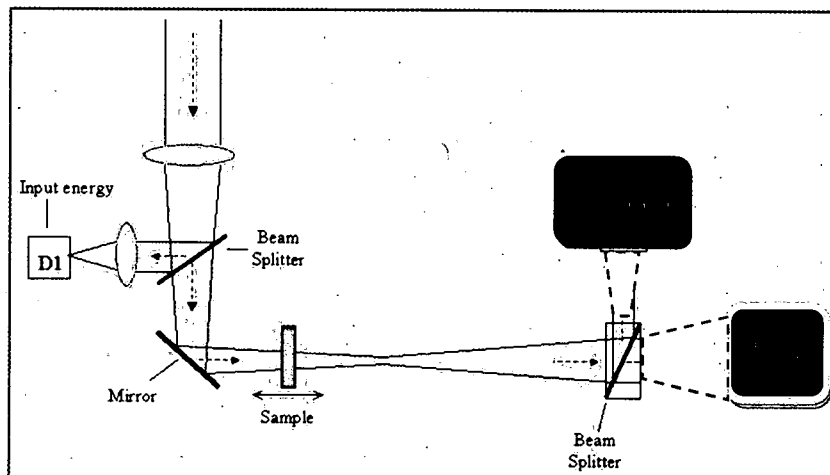


Figure 2.5: Zscan setup using three photodetectors and a closed aperture (iris).

Figure 2.5 represents a traditional Zscan setup; however, this was improved from the conventional setup with the use of a large CCD Dalsa digital camera that uses Labview software to analyze the closed and open apertures simultaneously. In addition, both the closed and open synthetic apertures translate with a misaligned beam. This is one of the most difficult aspects of running a Zscan, the alignment of the beam and dealing with a wedged sample – both of which can translate (or misalign) the beam off of the detectors.



**Figure 2.6: Zscan setup using a Dalsa CCD large array camera along with synthetic apertures.**

Figure 2.6 shows the improved method of collecting  $n_2$  and  $\beta$  nonlinear parameters. The large CCD and synthetic tracking apertures nearly eliminates any alignment issues. The beam enters from the top left in the figure. It travels through a long focal length lens and hits a beam splitter. Part of the beam goes to the first detector, D1. This D1 detector is used to set the energy entering the sample.

When the sample is a two-photon absorber (has a significant TPA coefficient,  $\beta$ ), it will absorb more light at the focus where the photon density is highest. The 'open aperture' detector, D2, measures how much light is transmitted through the sample. The closed detector, D3 (or the synthetic closed aperture), has a partially closed iris or aperture in front of it. The amount of light passing through the aperture will therefore change as the sample moves through the focus. A sample with a non-linear index of refraction actually acts as a positive or negative lens focusing or defocusing the beam. As a result, the energy will change at the closed aperture detector.

This Zscan analysis assumes a Gaussian TEM<sub>00</sub> beam where the electric field is defined as:

$$\vec{E} = E_o(t) \cdot \frac{w_o}{w(z)} \cdot e^{\frac{-2r^2}{w^2} - \frac{i \cdot k \cdot r^2}{2R(z)} - i\varphi} \quad \text{Equation 2.4}$$

Where  $w_o$  is the spot size,  $k$  is the wave number,  $2\pi/\lambda$ ,  $\varphi$  is the phase,  $R(z)$  is the radius of curvature of the phase front, and  $w(z)$  is the spot size at given distance  $z$ . Where  $w(z)$ ,  $R(z)$ , and  $z_o$  are defined below.

$$w(z) = \sqrt{w_o^2 \cdot \left(1 + \frac{z^2}{z_o^2}\right)} \quad \text{Equation 2.5}$$

$$R(z) = z \cdot \left[1 + \frac{z_o^2}{z^2}\right] \quad \text{Equation 2.6}$$

The examination of the cubic nonlinear index of refraction is done using the following:

$$n = n_o + \frac{n_2}{2} \cdot |E|^2 = n_o + \gamma \cdot I \quad \text{Equation 2.7}$$

Here,  $n_o$  is the linear index of refraction,  $n_2$  is the nonlinear index of refraction in esu units,  $E$  is the electric field or as indicated,  $n$  can be expressed in MKS units in terms of the nonlinear index of refraction  $\gamma$ , and the irradiance  $I$ .

Using the slowly varying envelope approximation (SVEA), allows the assumption that only the radial phase component to be considered. Also, assumed is the medium is considered "thin", which implies that  $L \ll z_o$  for linear diffraction and  $L \ll z_o/\Delta\varphi$ ; where  $\Delta\varphi$  is the change in the radial phase component or on-axis phase shift at the focus – and

$\Delta\phi$  is considered to be small. The equations governed by the SVEA approximations are given as: (where Equations 22-34 are defined by Sheik-Bahae *et al*)<sup>13</sup>

$$\frac{d\Delta\phi}{dz} = \Delta n(I) \cdot k = \gamma \cdot I_o \cdot k \quad \text{Equation 2.8}$$

$$\frac{dI}{dz} = -\alpha(I) \cdot I \quad \text{Equation 2.9}$$

Where  $z$  is the propagation depth in the sample and  $\alpha(I)$  holds the linear and nonlinear absorption terms. Now integrating Equation 21 and 22 from 0 to  $L_{eff}$  and solving for  $\Delta\phi$  and  $I$  respectively, leads to

$$\int \Delta\phi = \int_0^{L_{eff}} \gamma \cdot I_o \cdot k \cdot dz = \gamma \cdot I_o \cdot k \cdot L_{eff} \quad \text{Equation 2.10}$$

$$\int \frac{dI}{I} = \int_0^L -\alpha \cdot dz \quad \text{Equation 2.11}$$

$$\ln(I) = -\alpha \cdot L \quad \text{Equation 2.12}$$

$$I = I_o \cdot e^{-\alpha \cdot L} \quad \text{Equation 2.13}$$

Here  $\alpha$  is the linear absorption coefficient and  $L$  is the length of the sample. Now, combining Equation 21 and 23 we have a derivation for the phase shift at the focus,

$$\Delta\phi = k \cdot \Delta n \cdot L_{eff} \quad \text{Equation 2.14}$$

From the above equations we can now solve for the effective length of the sample,  $L_{eff}$ .

That is,

$$\Delta\phi = \int_0^L \gamma \cdot I \cdot e^{-\alpha z} dz = \frac{-k \cdot \gamma \cdot I}{\alpha} (e^{-\alpha L} - 1) = \frac{(1 - e^{-\alpha L})}{\alpha} \cdot \Delta n \cdot k \quad \text{Equation 2.15}$$

$$L_{\text{eff}} = \frac{\Delta\phi}{k \cdot \Delta n} = \frac{(1 - e^{-\alpha L})}{\alpha} \quad \text{Equation 2.16}$$

Where L is the sample length, and  $\Delta n$  is defined as  $\gamma I(t)$ . The transmitted power through the closed aperture is found by integrating the electric field with respect to the spatial radiating component, r, and time giving:

$$P_T = c \cdot \epsilon_0 n_o \pi \cdot \int_0^{r_a} |E|^2 \cdot r dr \quad \text{Equation 2.17}$$

Here  $\epsilon_0$  is the permittivity in vacuum, and c is the speed of light in m/s. Using the transmitted power,  $P_T$ , the normalized transmission can be defined as:

$$T = \frac{\int_{-\infty}^{\infty} P_T \cdot dt}{S \int_{-\infty}^{\infty} P_i \cdot dt} \quad \text{Equation 2.18}$$

Where  $P_i$  is the input power within the sample and S is the aperture linear transmittance.

$P_i$  and S are defined as:

$$P_i = \frac{\pi \cdot w_o^2 \cdot I_o}{2} \quad \text{Equation 2.19}$$

$$S = 1 - \exp\left(\frac{-2r_a^2}{w_a^2}\right) \quad \text{Equation 2.20}$$

Here,  $r_a$  is the radius of the closed aperture and  $w_a$  is the radius of the laser beam at the location of the closed aperture after passing ~400mm past focus at the CCD array, in our case. For large S-values (or closed aperture radii) the transmittance, T, goes to 1 (100%).



For a small on-axis phase shift at focus,  $\Delta\phi$ , the peak and valley occur at the same distance with respect to the focus. When the phase shift increases, the peak and valley separate, which typically means too much energy is at the input causing error in the measurement. For a cubic nonlinearity  $\Delta\phi$  distance is found to be  $0.86z_0$ . The actual equations used in Mathcad for fitting  $\beta$  (NL absorption) and  $n_2$  (NL index) are defined later in a following section.

## 2.2 Femtosecond Beam Characterization

The laser system used was a Clark-MXR 2010 femtosecond (fs) laser system that generates a 780 with a pulse width ( $\Delta t$ ) of 150fs. Discussed in this section will be the characterization of the beam and how these parameters are measured. Here,  $w_{ox}$  and  $w_{oy}$  are the spot sizes in the x and y directions. As stated previously, the fluence is not dependent on the pulse shape (pulse width), S, shown below is the peak fluence equation, which is the integration of the total energy over the entire area.

$$E = F_o \cdot 2\pi \cdot \int_0^{\infty} r \cdot \exp\left(-2 \frac{r^2}{w(z)^2}\right) \cdot dr = F_o \cdot 2\pi \cdot w_{ox} \cdot w_{oy} \quad \text{Equation 2.21}$$

$$F_o = \frac{2 \cdot E}{\pi \cdot w_{ox} w_{oy}} \quad \text{Equation 2.22}$$

The spot sizes are dependent on  $M_x^2$  and  $M_y^2$  (M-squared in x and y directions – described in the next subsection), the wavelength  $\lambda$ , and the entrance aperture, the focal length  $f_{x,y}$ , and the propagation distance away from the laser output coupler Z.

$$w_{ox,y} = \frac{\lambda \cdot f_{x,y} \cdot M_{x,y}^2}{\pi \cdot w(z_{x,y})} \quad \text{Equation 2.23}$$

Where  $w(z_{x,y})$  is the spot radius as a function of propagation distance  $Z$ , and the Rayleigh range  $Z_R$ .

$$w(z_{x,y}) = r_{x,y} \cdot \sqrt{1 + \left( \frac{Z}{Z_{Rx,y}} \right)^2} \quad \text{Equation 2.24}$$

$$Z_{Rx,y} = \frac{\pi \cdot r_{x,y}^2}{\lambda} \quad \text{Equation 2.25}$$

Here,  $r_{x,y}$  is the entrance aperture radius. The above equations are used in Mathcad software to predict the focused spot size, the peak fluence, and the peak intensity for a given focal length lens (spherical or cylindrical) and  $M^2$  – again, measured before each experiment.

### 2.2.2 Beam Characterization

Before any experiment was performed the beam profile, spectrum, pulse width, energy, and propagation constant ( $M^2$ ) was measured and Mathcad and Zemax software used to calculate the linear performance before and after focus. The  $M^2$  is a measured quantity that is used to characterize the deviation from diffraction limited focusing ( $M^2$  of 1 represents the diffraction limit, and real beams have  $M^2 > 1$ ); it is also known as the propagation constant and characterizes how the beam will transfer through space. Below is an example of a typical  $M^2$  of the femtosecond beam before entering the lens system.

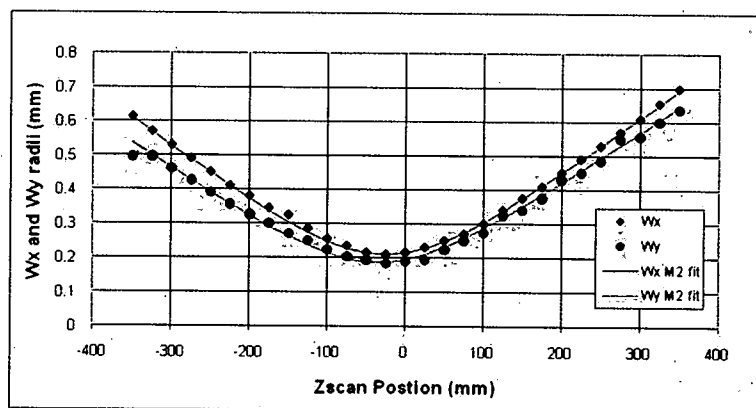


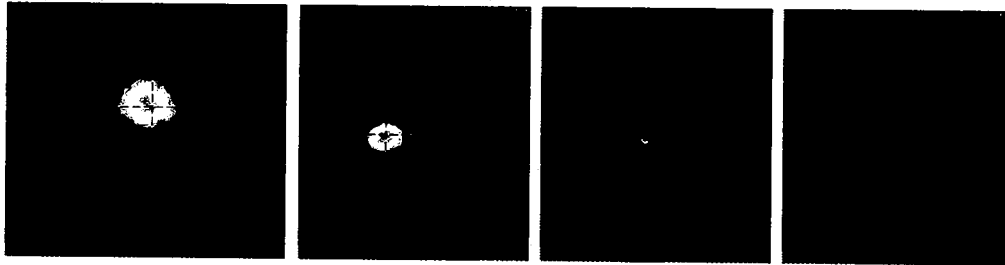
Figure 2.7: An example of the  $M^2$  for the femtosecond beam.

Figure 2.7 shows a typical  $M_x^2$  of 1.5 and  $M_y^2$  of 1.2 with nearly 0 astigmatic, or  $Z_{ox} \sim Z_{oy}$  – with  $Z_o$  being the Z-position of  $w_{ox}$  and  $w_{oy}$  theoretically at 0mm. In this case,  $Z_{ox}$  is -25mm and  $Z_{oy}$  is -30mm so the beam is slightly astigmatic – an acceptable amount. The  $M^2$  was measured by imaging the beam before the focus of a 250mm lens and translating through the z-coordinate past focus, while recording the spot diameters in x and y. The spot diameters (or radii) were then plotted as a function of position then fitted using Gaussian beam propagation spot size as a function of  $Z$ ,  $w(z)$ , and  $Z_o$ ,  $w_o$ , stated in the above equations. The  $M^2$  is solved using the above equations and plotted leaving it as a variable or fitting parameter.

### 2.2.3 Beam Profile

The beam profile is measured to determine the clear aperture (diameter of the beam in major and minor axes) just before the focusing element to measure the clear aperture and to ensure that no diffraction effects exist from a misaligned optical train. The profile measurement is also carried out after the focusing lens, before and after focus or through

focus, to make certain there is no structure in the beam that would arise from an undesirable phase front with a poorly aligned optical train (i.e. if the beam were to “scrap” an optical mount).



**Figure 2.8: Beam profiles of four beams (from left to right): the clear aperture, a beam before the focus, the beam at focus, and a beam after focus with poor phase front causing a higher order spatial profile.**

Figure 2.8 shows the profiles of the beam before the lens, then through focus with an unwanted phase front “riding” on the beam causing the spatial profile to undergo a transformation from a  $TEM_{00}$  single order near Gaussian profile to some higher order profile. Figure 2.8 gives an example of the beam profile measured using Spiricon laser beam analysis (LBA) software and a Cohu 4812 silicon CCD array. The clear aperture is typically 5.5mm in diameter, and the smallest spot size the Cohu can measure is  $\sim 50\mu m$  accurately before the beam becomes too small for the camera resolution (i.e. the beam becomes smaller than  $\sim 10$  pixels). Obviously, much smaller spot sizes are desired for micromachining. Thus, in order to measure these small spot sizes there are two options. One is to simply measure the spot size (and/or  $M^2$ ) using a 250mm lens that will cover many more pixels to provide ample resolution to measure the beam. Or, a second simple method is to use a long working distance microscope objective, which will magnify the focused beam ( $\sim 12.6$  magnification in this case). Both of these methods, plus using Zemax calculations are very reliable in predicting the system performance.

### 2.2.4 Beam Spectrum

The Clark-MXR laser spectrum was measured on multiple occasions, especially before a critical measurement, using an Ocean Optics UV-NIR fiber spectrometer, model HR4C130. The typical spectrum is given below.

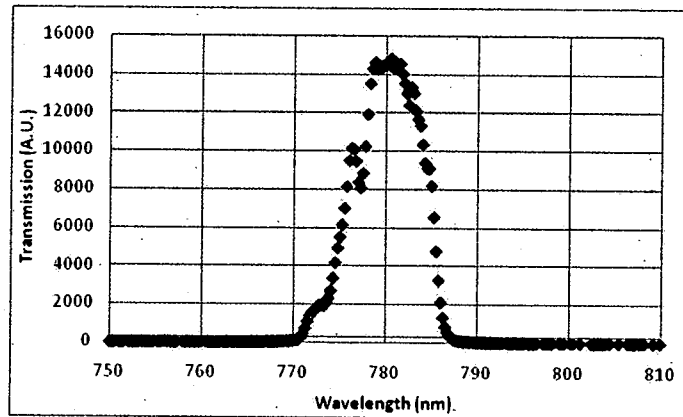


Figure 2.9: UV-NIR Ocean Optics spectrum of the Clark-MXR 2010 beam.

Figure 2.9 shows the spectrum of the femtosecond beam centered at 780nm with a FWHM band width of ~10nm.

### 2.2.5 Pulse Width

The pulse width was measured with a Clark-MXR AC 150 auto-correlator. The typical pulse width,  $\Delta t$ , is between 150fs and 180fs as shown in the figure below.

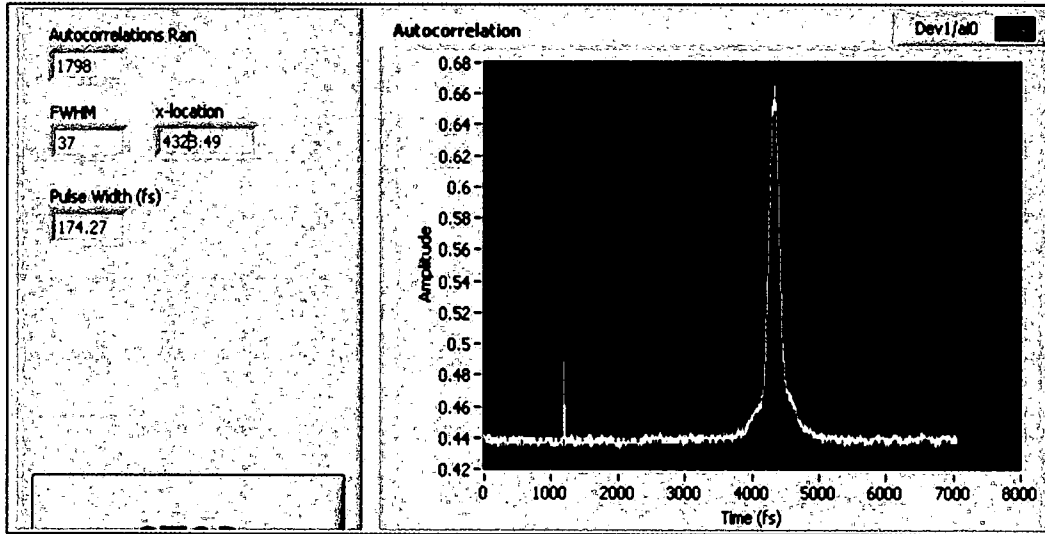


Figure 2.10: Pulse width of the femtosecond laser using the Clark-MXR auto-correlator. The small peak is only an artifact of the data acquisition software.

The  $\Delta t$ , as shown in Figure 2.10, was measured by the auto-correlator, which was calibrated before each measurement. The AC 150 auto-correlator is calibrated using a manual micrometer stage that adjusts the delay line. Where the doubled 775nm pulse (387.5nm using BBO) is split (similar to a Michelson interferometer) and the two doubled pulses are focused onto another BBO crystal that utilizes nonlinear sum frequency generation (SFG). Only SFG pulses are overlapped and correlated with respect to each other. The micrometer reading and the sample position are both recorded and are then used in the following equation, which is then used to set the FWHM of the auto-correlation scan to a  $\Delta t$  in femtosecond units.

$$\Delta t = \frac{\Delta d}{\Delta p} \cdot \frac{2}{1.54 \cdot C} \quad \text{Equation 2.26}$$

Here  $\Delta d$  is the difference in the micrometer readings,  $\Delta p$  is the difference in the Labview centroid position at each micrometer position, 1.54 is the  $\text{Sech}^2$  correction factor, and  $C$  is the speed of light.

### **2.2.6 Beam Energy**

The energy of the beam entering the lens system is an important quantity in the micromachining process and is measured using a NIST traceable joule meter. The joule meter energy measurement is then used to calibrate the photocells for the damage test bed (DTB) shown in Figure 3.4, and used to set the energy for Zscan experiments. The femtosecond laser pulse characterization was done prior to every experiment; some of the theories related to these experiments are described subsequently.

### **2.3 Zscan Measurements of SiC**

The nonlinear properties, nonlinear index of refraction ( $n_2$ ) and nonlinear absorption ( $\beta$ ), of SiC semi-insulating and SiC conducting were investigated. In calculating the nonlinear parameters two approximations are applied to reduce the computation speed and complexity. One is the thin sample approximation, where the sample thickness  $\gg Z_R$ , and the second is the weak nonlinear approximation that assumes the nonlinear process is small.<sup>12</sup> The calculated  $n_2$  data is made using the peak to valley of the closed aperture measurement and is defined by<sup>13</sup>

$$n_2 = \frac{\Delta\Phi_o}{kL} \cdot \frac{1}{I_o}, \quad \text{Equation 2.27}$$

where  $\Delta\Phi_0$  is the on-axis phase shift at the focus,  $k$  is the wave number,  $L$  is the length of the sample and  $I(z,E)$  is the intensity as a function of  $z$ -position and energy for the pulse given by<sup>13</sup>

$$I(z,E) = \frac{2E \cdot \ln(1 + \sqrt{2})}{\Delta t \cdot \pi \cdot w_0^2}, \quad \text{Equation 2.28}$$

where  $\Delta t$  is the pulse width,  $w_x$  and  $w_y$  are the spot radii of the beam in  $x$  and  $y$  directions. As stated above,  $\Delta\Phi_0$  is the on-axis phase shift,  $\Delta\Phi$ , which can be experimentally determined by examining the peak-valley transmission change in the closed aperture case using<sup>13</sup>

$$|\Delta\Phi_0| = \frac{\Delta T_{pv}}{(0.406)(1-S)^{0.25}}, \quad \text{Equation 2.29}$$

where  $S$  is the linear transmittance aperture ( $S$ -Parameter) and defined by<sup>13</sup>

$$S = 1 - \exp\left(-2 \frac{r_a^2}{w_a^2}\right). \quad \text{Equation 2.30}$$

Here,  $r_a$  is the radius of the closed aperture and  $w_a$  is the radius of the laser beam at the location of the closed aperture. Equation 5 can then be used to recover the  $n_2$  value of the sample under test.

We will not describe the detail of the fit data, rather we direct the reader to reference,<sup>14</sup> which describes precisely how to apply the theory and equations to any mathematical software such as Mathcad, Matlab, etc. The normalized open aperture signal is fitted to<sup>14</sup>

$$T(x,z,\beta,E) := \frac{1}{2 \cdot q_0(z,\beta,E)} \cdot \int_{-\infty}^{\infty} \ln(1 + q_0(z,\beta,E) \cdot \text{sech}(x)^2) dx, \quad \text{Equation 2.31}$$



where  $q_0$  is defined by<sup>14</sup>

$$q_0(z, \beta, E) := \beta \cdot I(z, E) \cdot L \quad \text{Equation 2.32}$$

This work utilizes the open and closed fits to average the noise in the data. The peak-valley of the closed data fit is used to calculate the on-axis phase shift. The NL index fitting equation is given by<sup>14</sup>

$$T_c(z, \beta, E, n_2) = 1 + \frac{4 \cdot \zeta(z) \cdot L \cdot I(z, E) \cdot n_2 \cdot k}{(\zeta(z)^2 + 9) \cdot (\zeta(z)^2 + 1)} + \frac{q_0(z, \beta, E) \cdot (\zeta(z)^2 + 3)}{(\zeta(z)^2 + 9) \cdot (\zeta(z)^2 + 1)} \quad \text{Equation 2.33}$$

Here  $\zeta(z)$  is defined by<sup>14</sup>

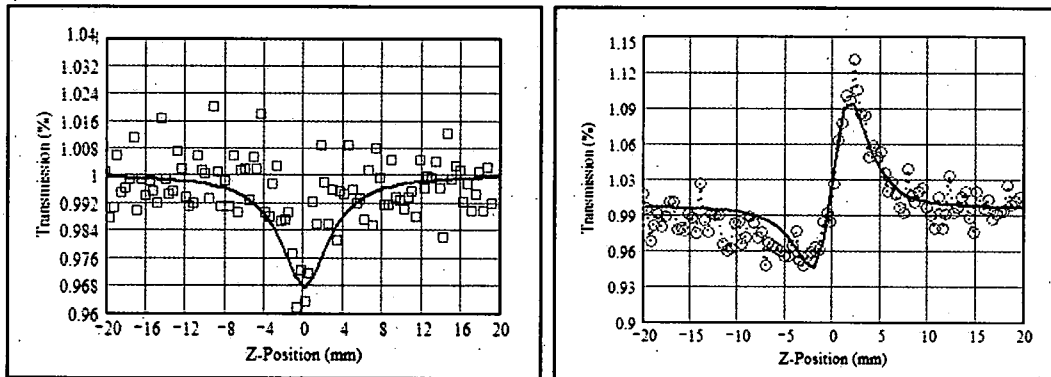
$$\zeta(z) = \frac{z}{\sqrt{Z_{rx}^2 + Z_{ry}^2}} \quad \text{Equation 2.34}$$

Where  $Z_{rx,y}$  is the Rayleigh range for x and y directions, and z is the z-position.

For the FS and SiC data, the settings chosen were a synthetic closed aperture of 0.55mm, an open aperture of 5mm, a repetition rate of 41Hz (with assistance from a chopper wheel), an S-parameter set to 15%, and an energy ranging from 2μJ to 6μJ. Multiple energies were used to ensure consistent nonlinear measurements. The beam was characterized before the experiments by performing an  $M^2$  measurement, evaluating the pulse width using a Clark-MXR AC 150 Auto-correlator, and profiling the beam with a Cohu CCD camera. The beam was profiled with and without the sample to properly calculate the S-Parameter (shown in Equation 8). Representative Z-scan data is shown as raw data with open and closed aperture data fits, which provide the  $n_2$  and  $\beta$  results. The results for the SiC and FS Z-scans are found in Table 2.4.

The SiC  $\beta$  and  $n_2$  experimental results were compared to a simple two-parabolic-band model by Sheik-Bahae *et al*<sup>15</sup> for theoretically calculating the nonlinear absorption and index of refraction properties in semiconductors. The bandgap used to calculate the theoretical  $\beta$  and  $n_2$  was calculated using the wavelength at the 1% transmission point in the UV-Vis chart in Figure 2.2. This model was not used for FS since it is not a semiconductor.

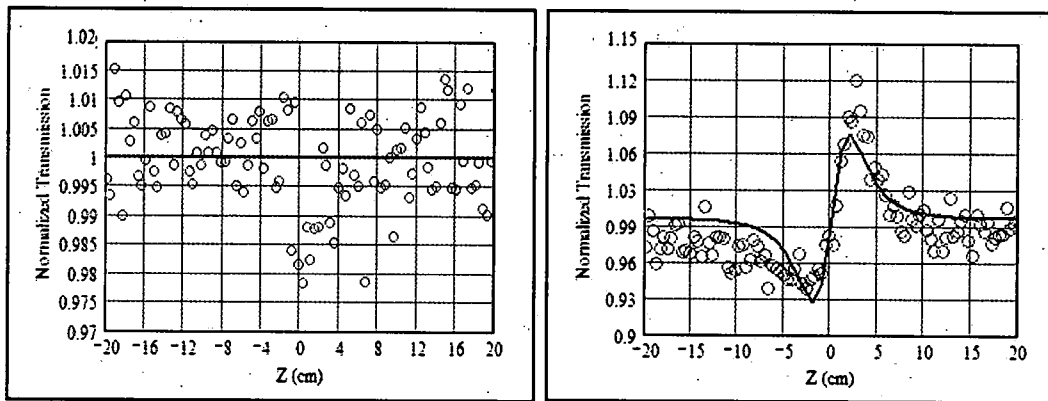
The referenced fused silica (FS) Z-scan results show  $n_2$  values of  $2.5 \times 10^{-7} \text{ cm}^2/\text{GW}$ <sup>16</sup>, but published  $\beta$  values were not located, primarily due to fact that FS has little or no nonlinear absorption (from large bandgap). However, while the experimental setup verified using a referenced FS sample, we found that the FS sample was presenting a  $\beta$  signature, while in our past results, shown earlier we found that FS does not have a  $\beta$  signature. Therefore, an exploration was done to find out exactly what was causing this effect. The figures below give the initial FS  $\beta$  and  $n_2$  results with the unexplained  $\beta$  displayed.



**Figure 2.11: FS nonlinear  $\beta$  and  $n_2$  with an unexplained  $\beta$ -signature.**

In Figure 2.11, the FS  $\beta = 3.2 \times 10^{-3} \text{ cm/GW}$ , and  $n_2 = 2.4 \times 10^{-6} \text{ cm}^2/\text{GW}$ . As shown in Figure 2.11 there exists a  $\beta$ -signature that is not supposed to be there and after looking

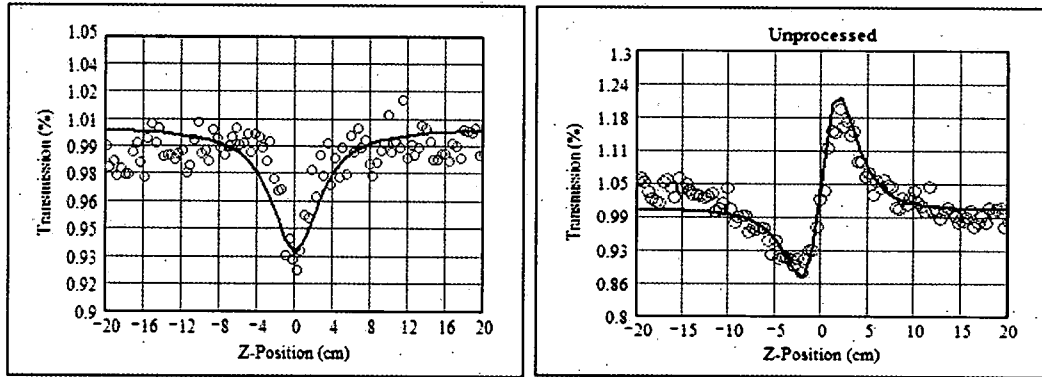
into a number of possibilities, such as saturation absorption, nonlinear absorption, polarization effects, and even the likelihood that the Labview program was the cause, we finally concluded that this affect was because the open aperture was too small for the diverging beam after propagating through the 750mm focus to the Dalsa CCD array (without a sample) where a synthetic open aperture was employed. The beam was originally ~7mm in diameter 1260mm past focus, which is roughly the same size or slightly larger than the CCD array. Therefore, the CCD camera was then moved 460mm closer to the focus, which resulted in a 3.8mm beam diameter on the CCD array. This resolved the false  $\beta$ -signature as shown in the following figure.



**Figure 2.12: The Corrected FS Zscan with the CCD array closer to the focus to eliminate the beam from walking off of the array.**

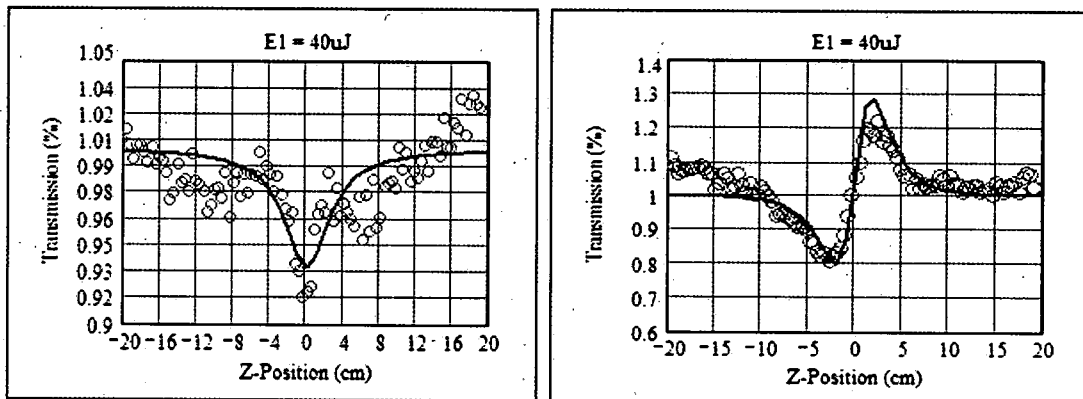
In Figure 2.12 above, 3 $\mu$ J of energy was used; the  $\beta$  is now essentially zero, while the  $n_2$  is  $2.4 \times 10^{-6} \text{ cm}^2/\text{GW}$ . In this case, the  $\beta$  before resolving this issue by moving the CCD closer to the focus was small enough that it really did not affect the  $n_2$  as it maintains the same value with and without a  $\beta$ -signature.

Once this issue was resolved the Zscan of FS was properly performed resulting in a nonlinear index of refraction that agrees with Chappell *et al.*<sup>12</sup> Next the Zscan of the unprocessed and processed SiC sample was measured and those results are given below.



**Figure 2.13:** On the Right is the normalized transmission for the open aperture and on the Left is the normalized transmission for the closed aperture both for the unprocessed SiC semi-insulating sample. The parameters used for this sample were energy of  $3\mu\text{J}$ , a 750mm lens, and a 5.1mm entrance aperture.

Next, shown are the results from the processed SiC semi-insulating sample. Figure 36 shows these results for each processed energy levels:  $E_1=40\mu\text{J}$ ,  $E_2=20\mu\text{J}$ , and  $E_3=10\mu\text{J}$ .



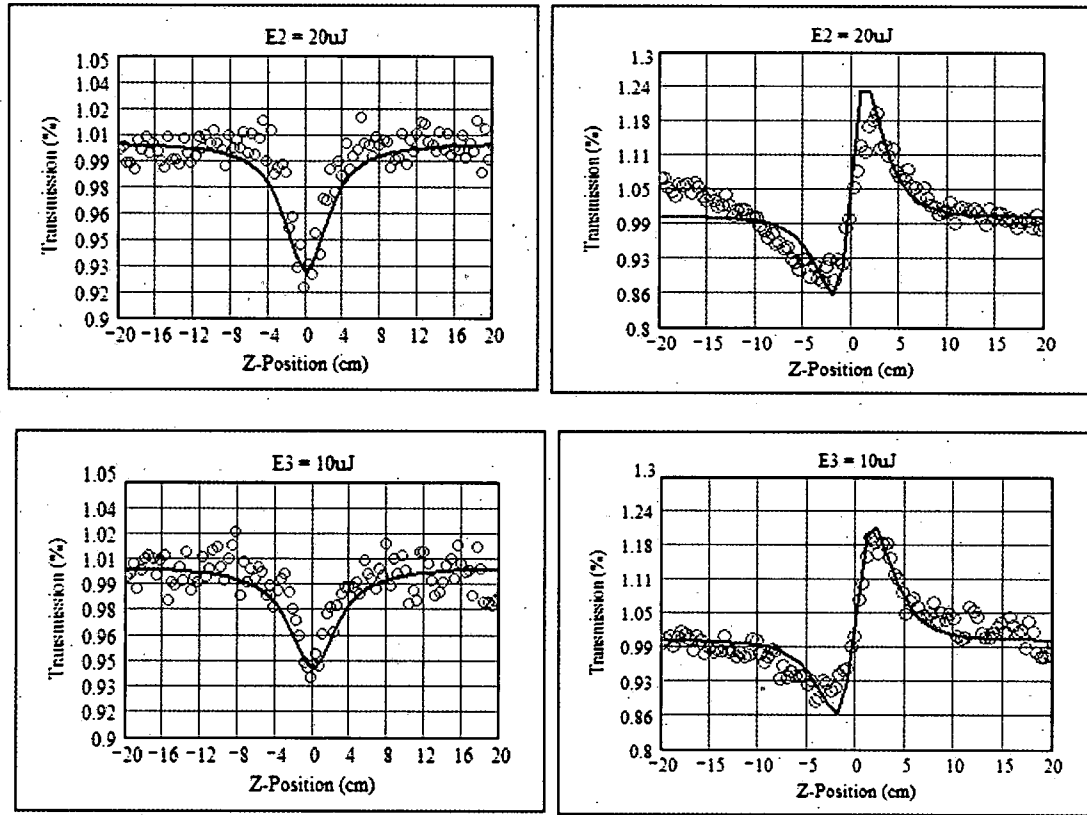


Figure 2.14: Top is the Open ( $\beta$ ) and Closed ( $n_2$ ) Zscan of  $E1 = 40\mu\text{J}$  processed area of SiC, Middle is  $E2 = 20\mu\text{J}$  processed area, and on the Bottom is the  $E3 = 10\mu\text{J}$  processed area of SiC.

The results for the unprocessed and processed SiC Z-scans are found in Table 2.4. The experimental values were compared with theoretical calculations for semi-conductor nonlinear  $\beta$  and  $n_2$  from Sheik-Bahae *et al*<sup>15</sup> and are expressed below.

$$\beta = \frac{k \cdot \sqrt{21\text{eV}}}{n_{\text{SiC}}^2 \cdot E_g^3} \cdot F_2 \quad \text{Equation 2.35}$$

Here,  $k$  is the material constant and is equal to 1940 when  $E_g$  has units of eV give by Sheik-Bahae *et al*<sup>15</sup>; 21eV is related to the Kane momentum parameter and is approximately 21 eV for most direct band-gap semiconductor materials.  $E_g$  is the bandgap of SiC, which can be found from the UV-Vis transmission plot in Figure 2.2.

The refractive index of SiC,  $n_{\text{SiC}}$ , is stated in Section 2.1.1 SiC Sample, and  $F_2$  is a function stated below.

$$F_2 = \left( 2 \cdot \frac{E_p}{E_g} - 1 \right)^{\frac{3}{2}} \cdot \left( 2 \cdot \frac{E_p}{E_g} \right)^{-5} \quad \text{Equation 2.36}$$

Here  $E_p$  is the photon energy given for  $\lambda$  and expressed in eV. For the SiC SI and SiC conducting samples the  $\beta = 0.055 \text{ cm/GW}$  as stated in Table 2.4. The nonlinear index of refraction,  $n_2$ , is defined as

$$n_2 = \frac{k_2 \cdot \sqrt{21eV}}{n_{\text{SiC}} \cdot E_g^4} \cdot G_2 \quad \text{Equation 2.37}$$

Here,  $k_2$  is a material constant which provides the proper scaling for the units of  $\text{cm}^2/\text{GW}$ , and  $G_2$  is a constant given as<sup>13</sup>

$$G_2 = \left( 2 \cdot \frac{E_p}{E_g} \right)^{-6} \cdot \left[ \left( \frac{-3}{8} \right) \cdot \left( \frac{E_p}{E_g} \right)^2 \cdot \left( 1 - \frac{E_p}{E_g} \right)^{-\frac{1}{2}} + 3 \cdot \left( \frac{E_p}{E_g} \right) \cdot \left( 1 - \frac{E_p}{E_g} \right)^{\frac{1}{2}} - 2 \cdot \left( 1 - \frac{E_p}{E_g} \right)^{\frac{3}{2}} + 2 \cdot \Phi \cdot \left( 1 - 2 \frac{E_p}{E_g} \right) \cdot \left( 1 - \frac{E_p}{E_g} \right)^{\frac{3}{2}} \right] \quad \text{Equation 2.38}$$

Again  $E_p$  and  $E_g$  are defined above, and  $\Phi$  is a step function (or unit step function), where it returns 0 if (x) is negative and 1 if (x) is otherwise.

**Table 2.4: Nonlinear measurements resulting from the Z-scan experiment. Multiple energies were tested to provide a statistical average.**

Sample	$\beta$ (cm/GW) Theory	$\beta$ (cm/GW) Measured	$n_2$ (cm <sup>2</sup> /GW) Theory	$n_2$ (cm <sup>2</sup> /GW) Measured
FS	NA	0	NA	$2.60 \times 10^{-7}$
SiC semi-insulating	0.055	0.056	$3.6 \times 10^{-6}$	$4.75 \times 10^{-6}$
SiC conducting	0.055	0.052	$3.6 \times 10^{-6}$	$4.00 \times 10^{-6}$
E1 Processed SiC SI	0.055	0.064	$3.6 \times 10^{-6}$	$7.4 \times 10^{-6}$
E2 Processed SiC SI	0.055	0.057	$3.6 \times 10^{-6}$	$5.1 \times 10^{-6}$
E3 Processed SiC SI	0.055	0.056	$3.6 \times 10^{-6}$	$4.79 \times 10^{-6}$

Table 2.4 shows a comparison with the unprocessed and processed SiC semi-insulating (SI) samples. Observed is an increased in the nonlinear index of refraction with increasing energy applied in the processed SiC, but no increase in the nonlinear absorption. Also shown is no difference between semi-insulating and conducting unprocessed samples. At  $10\mu\text{J}$  there is no significant increase in  $n_2$ , but as the energy is increased, there is a larger  $n_2$  suggesting that the linear index of refraction is thus being altered. The figure below describes this effect.

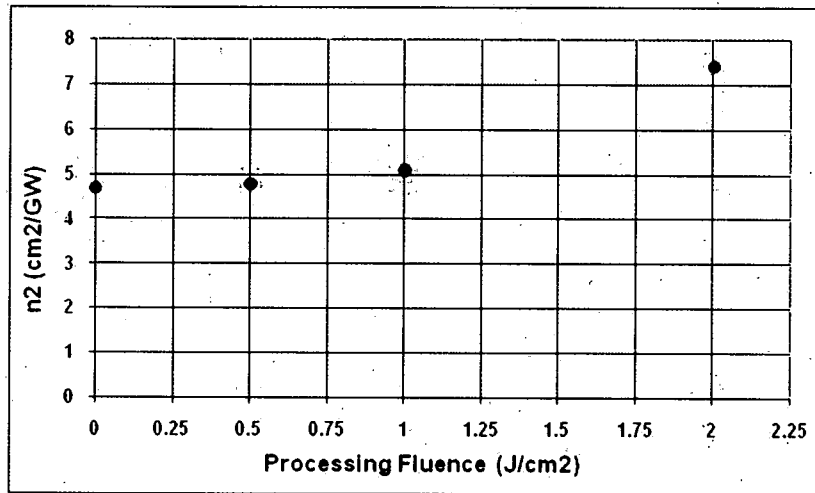


Figure 2.15: Nonlinear index of refraction in SiC SI as a function of applied fluence.

Figure 2.15 shows the  $n_2$  increasing with applied fluence. This indirectly shows a linear index of refraction dependence on applied fluence. Next, these  $n_2$  results were also used to derive  $\Delta n$ , which is then compared with  $\Delta n$  consequent from the diffraction efficiency results from an earlier section in this chapter.

## **CHAPTER 3**

### **Anamorphic Lens Design and Grating Formation**

The design and implantation of the anamorphic lens is discussed in this chapter. The design was based on the fact that a single pulse index modification can be produced in a faster and more convenient manner. The anamorphic lens was employed to develop a new way of micromachining grating structures as well as to use these gratings for the understanding of index modification in amorphous and crystalline materials, and to fabricate a new optical device using grating structures in crystalline substrates.

#### **3.1 Lens Design**

An anamorphic lens was developed to give an alternative method of micromachining bulk transparent materials. The challenge for femtosecond laser processing is to control the nonlinear effect of self-focusing, which can occur when using a fast f-number lens. Once the focused spot is dominated by self-focusing, the predicted focused beam becomes an unpredictable filament inside the bulk, which is an undesirable effect. The anamorphic lens resolves this self-focusing by increasing the numerical aperture (NA) and employing an elliptical beam shape. The anamorphic lens was designed to furnish a  $2.5\mu\text{m}$  by  $190\mu\text{m}$  line about a  $0.5\mu\text{m}$  deep at focus. Provided the pulse energy is high enough, transparent bulk material will be damaged or modified with a single femtosecond laser pulse. Damage in this text refers to visual change in the index of refraction as observed under an optical microscope. Using this elliptical line-shape, grating structures



were micro-machined on and below the surface of SiC bulk transparent substrate. From the lack of self-focusing and using energy that is just above the damage threshold, the focused line beam generated from the anamorphic lens grating structures produced a line shape nearly identical to the geometrical approximation.

The method of manufacturing gratings into any transparent material can be done on or below the surface. Using an elliptical beam to micro-machine gratings is an alternative to interference techniques and/or circular spot direct writing using high speed translation of the sample. It provides accurate micro-machined gratings in the absence of any self-focusing from the use of a highly elliptical beam.<sup>17</sup> An elliptical beam has a much higher damage threshold than that of symmetrically round beams due to the lack of self-focusing in the substrate.<sup>7</sup> With the anamorphic lens, the numerical aperture is very large in one axis, which results in a lower damage threshold for femtosecond radiation. Here, a large NA in combination with an elliptical beam will resist the chances of any self-focusing occurring within the bulk of the sample. Self-focusing filamentation will spoil the micro-machined features, which will result in unpredictable/undesired micro-machined features. The gratings produced with the elliptical beam generated with anamorphic lens, however, results in "clean" accurate gratings that closely resemble the geometrical profile.

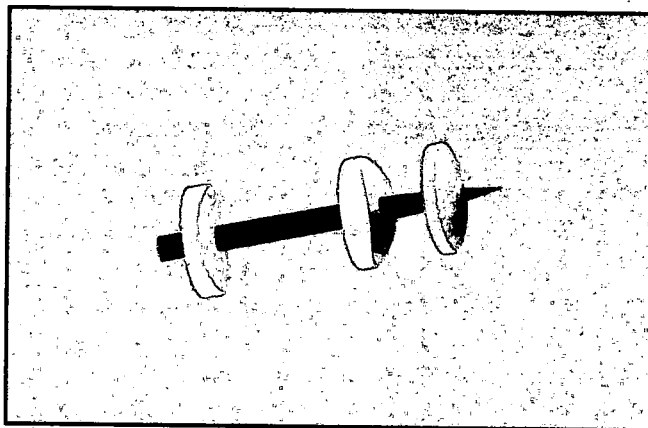
The design and analysis of this anamorphic lens design was accomplished using the software package, Zemax. The lens system consists of two cylindrical lenses (one for x-dimension and the other for the y-dimension) and a spherical lens. The spherical lens primarily assisted the x and y cylindrical lenses to give faster foci. The lens is simple to

assemble and align with the help of Thorlabs, Inc. lens tubes and standard off-shelf lenses. The lens prescription for this anamorphic lens is provided in the Table 3.1.

**Table 3.1: The anamorphic lens prescription from Zemax.**

Surface	Type	Radius (mm)	Thickness (mm)	Glass	Diameter (mm)	Lens Stock No.	Lens Manufacture
Object	Standard	$\infty$	$\infty$	Air	0		
Stop	Standard	$\infty$	10	Air	5.5		
2	Toroidal	$\infty$	5.6	BK7	25.4	25.4/50.9/C	CVI f=100mm
3	Toroidal	-50.9	0	----	25.4		
4	Standard	$\infty$	37.68	Air	5.5		
5	Toroidal	$\infty$	7.4	BK7	25.4	25.4/25.4/C	CVI f=50mm
6	Toroidal	-25.4	0	----	25.4		
7	Standard	$\infty$	12	Air	5.4833		
8	Standard	24.397	10.08	BK7	25.4	KBX046	NP f=25.4mm
9	Standard	- 24.397	0	----	25.4		
10	Standard	$\infty$	12.188	Air	2.8117		
Image	Standard	$\infty$	0	Air	0.36108		

The beam input into the anamorphic lens is completely characterized with pulse width,  $M^2$ , and profile measurements. The anamorphic lens was then characterized by measuring the numerical aperture (NA) in both axes, x and y. Figure 3.1 below shows a solid layout and a ray distribution through focus of the anamorphic lens.



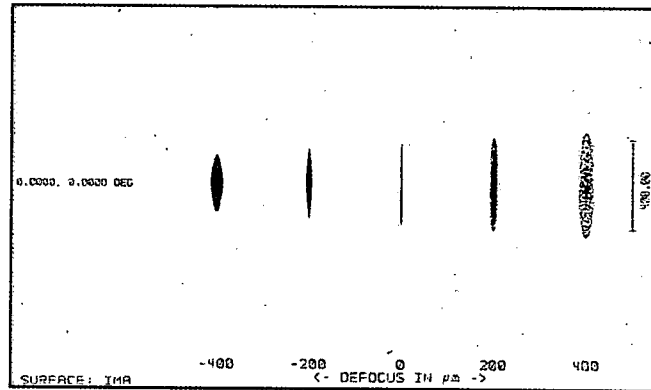


**Figure 3.1: Zemax analytic views of the anamorphic lens used spread the focused beam elliptically. Top is a Zemax solid layout displaying each lens and their relative position in the lens tube (on the left is a 100mm focal in x, middle is a 50mm in y, and on the right is the spherical lens), and Bottom is a plot of the ray distribution through focus  $\pm 400\mu\text{m}$ , where at defocus =  $0\mu\text{m}$  is the anamorphic line shape used for laser processing.**

The lens system was designed to transform the circular beam into a line distribution as shown in Figure 3.1. The x-dimension uses a 100mm focal length cylindrical lens and the y-dimension uses a 50mm focal length cylindrical lens. The last lens is a 25mm spherical lens, which is used to further assist the x and y foci into a slightly tighter focus and provide a line spread of high enough fluence above the damage threshold (DT) of the SiC substrate. The numerical aperture (NA), as mentioned, was used to characterize the anamorphic lens. A general NA equation is given below.<sup>18</sup>

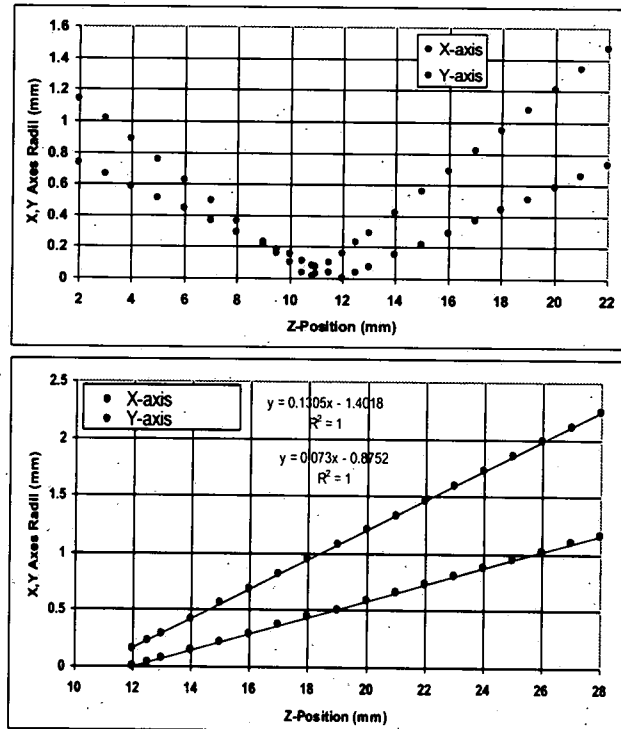
$$NA = \frac{D}{2f} = n \sin(\theta), \quad \text{Equation 3.1}$$

where D is the entrance aperture diameter, f is the effective focal length (EFL) of each axis, n, is the index of refraction, and  $\theta$  is the cone angle. The NA of this anamorphic lens system was found geometrically using Zemax and confirmed experimentally by performing a  $M^2$  measurement to extract the NA from the cone angle or slope of the data.

Figure 3.2 illustrates the comparative NA results between geometrical and theoretical  $M^2$  data. The NA was determined for each axis by finding the slope of a series of points after the focus. Table 3.2 gives both experimental and theoretical NA results of the anamorphic lens. The experimental and theoretical NA results show that the anamorphic lens design is functioning as predicted. The anamorphic lens results are also compared to the instantaneous NA at the desired line-focus at  $0\mu\text{m}$  defocus position as shown in Figure 3.1 as well as a commonly used spherical lens as shown in Table 3.2.

**Table 3.2: NA values for theoretical and experimental results.**

Type	NA <sub>x</sub>	NA <sub>y</sub>
Theoretical	0.073	0.131
Experimental	0.073	0.134
Instantaneous NA (at focus)	0.0035	0.256
Spherical 125mm Lens	0.022	0.022



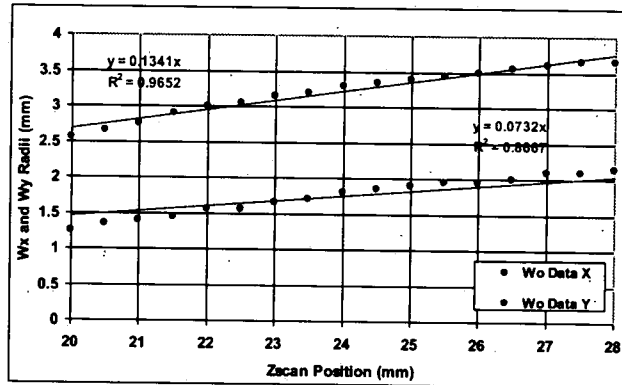


Figure 3.2. Shown here is the geometrical Zemax theoretical  $M^2$  (top chart), a zoomed in theoretical chart with linear fit (middle chart), and the experimental (bottom chart), which were used to determine the NA of each axis.

Shown in the figure below is an image of the anamorphic lens mounted and in the experimental setup.

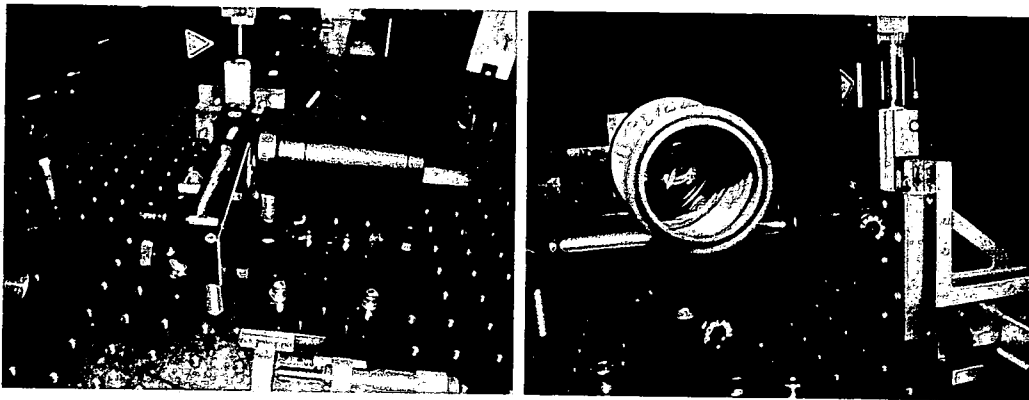


Figure 3.3: Shown here are images of the mounted anamorphic lens in the experimental setup.

Figure 3.3 shows the anamorphic lens in the automated setup. The lens, mounted, is only a little over 2" long and 1" in diameter. It is roughly 12mm from the sample from the end of the lens tube.

### 3.2 Experimental Setup

The DT and Z-scan experiments were completed using a single laser source split into multiple paths. Figure 3.4 below illustrates the experimental setups.

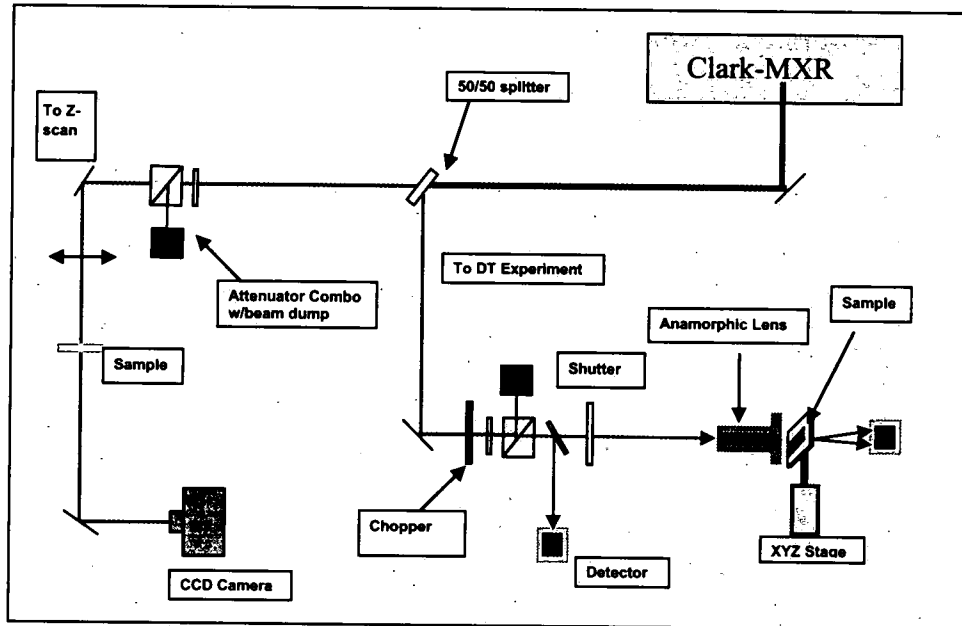


Figure 3.4: Optical setups for the damage threshold and Z-scan experiments.

Figure 3.4 gives the experimental setups for both the DT and Z-scan experiments. The Clark-MXR femtosecond laser system is split into multiple beam paths for different tests; a 100 $\mu$ J portion of that is split for the DT and Z-scan studies. In each experiment line there is a polarizer beam splitter and  $\frac{1}{2}$  wave plate combo used to attenuate the beams. The Z-scan uses a 750mm lens to provide a large Rayleigh range,  $Z_R$ , and to keep the fluence below the damage threshold. The DT experiment uses the anamorphic lens to morph the 5.5mm circular beam into a 2.5 $\mu$ m x 190 $\mu$ m line distribution as described in the Introduction section.

The Z-scan line uses a CCD camera (DALSA 1M15) to sense the transmitted beam, and the closed aperture is added synthetically, via software image processing. The synthetic aperture types (round or other shapes), range of the Z-scan, and camera calibration are all set before each scan. The experiment uses a large CCD array (typically about twice the beam diameter after focus) and synthetic apertures have allowed ease in alignment of the beam down the Z-scan line. In addition, the software can record an average of beam profiles (intensity) at each Z-location, and then save those images for further analyses.

The DT line uses input and output photodiodes to measure the incident pulse energy versus the transmitted energy through the sample. Each photodiode is calibrated using a pyroelectric Joule meter (traceable to National Institute of Standards). The DT line also has a chopper wheel and a high speed shutter which together work automatically control the number of pulses to the sample. Finally, the sample is held on a xyz automatic stage controlled with  $\pm 1\mu\text{m}$  accuracy. The entire illumination collection procedure is automated. This configuration, shown in Figure 3.4, allows for the Z-scan and DT experiments to run simultaneously, but the beams delivered at each experiment are separately characterized for completeness.

### **3.3 Threshold Measurements**

The damage threshold (DT) in this text refers to the limit where the substrate becomes modified as observed under an optical microscope using transmission or reflection. The DT values are an important quantity to report for future laser processing of SiC bulk materials. The DT is measured in  $\text{J}/\text{cm}^2$  and determines the minimum energy distribution

to induce an observable change into the SiC material. The fluence distribution in the beam focus is well-characterized as an elliptical and/or circular Gaussian with spot size along each principal axis given by<sup>18</sup>

$$w_{o,x,y} = \frac{\lambda \cdot f_{x,y} \cdot M_{x,y}^2}{\pi \cdot w_z}, \quad \text{Equation 3.2}$$

where  $f$  is the focal length,  $\lambda$  is the wavelength,  $M^2$  is a measured quantity that is used to characterize the deviation from diffraction limited and  $w_z$  is the spot radius propagating from the laser and is given in Chapter 2, which were used to calculate the spot size and fluence in each axis for the elliptical beam formed by the anamorphic lens system.

Figure 3.5 and Table 3.3 then gives the damage threshold results for FS, semi-insulating and conducting SiC. FS is our base-line sample, which is used to calibrate our DT experiments. FS has a DT that is well known to be  $\sim 3.0\text{--}4.0 \text{ J/cm}^2$  as referenced.<sup>19</sup>



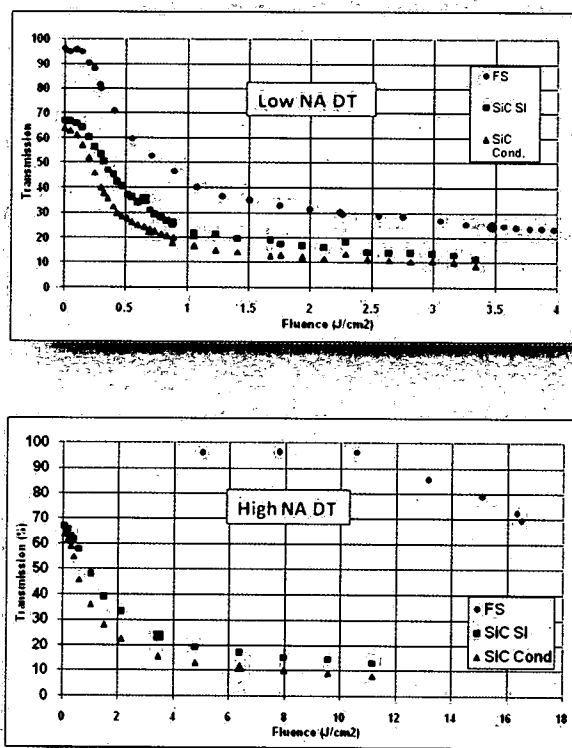


**Figure 3.5** On Top is a plot of the damage threshold (DT) for SiC semi-insulating (SI), SiC conducting, and Fused Silica (FS). On Bottom is the DT plot of SiC semi-insulating, SiC conducting, and FS as a function of fluence. The larger red data points represent where the visible damage begins.

These DT results greatly depend on NA as shown in Schaffer-Mazur<sup>17</sup> for tight focusing conditions. In Figure 3.5, the DT data was recorded using a 125mm lens (NA = 0.022). To show the dependence of NA, as Schaffer-Mazur, we employed our anamorphic lens and repeated the DT plot shown in Figure 3.5. The DT results are tabulated in Table 3.3 below.

**Table 3.3:** DT measured results for two lenses: 125mm focal and the anamorphic lens (High NA).

Sample	DT (J/cm <sup>2</sup> )	High NA DT (J/cm <sup>2</sup> )	Bandgap
FS	3.7	~30-40	9eV
SiC semi-insulating	0.6	3.5	3.1eV
SiC conducting	0.65	6.4	3.1eV

As shown in Table 3.3 the use of a high NA focusing geometry increases the DT, as inspected under an optical microscope, by a factor of 6 to 10 times from the spherical 125mm lens. The FS sample did not reach a DT for the high NA experiment, and it is predicted that 100 $\mu$ J (for a fluence of  $\sim 35$  J/cm<sup>2</sup>) or more is needed to create a 2.5 $\mu$ m X 190 $\mu$ m line on or below the surface.

### **3.4 High NA Sample Characterization**

The high NA line distribution processed into the 6H-SiC semi-insulating and conducting samples used in this chapter for the DT experiments were further analyzed using optical microscopy and Atomic Force Microscopy (AFM) to understand the morphology of the index modified structures. The processed lines are on or just below the surface, and the modifications form a hill/valley above/below the surface depending on the type of SiC processed. The figures below illustrate this effect. For these images, the optical microscope used is an Olympus upright digital BX51 microscope with Nomarski DIC capabilities that use high contrast prisms to produce increased contrast/resolution. This microscope also has measuring capabilities to  $\pm 0.25\mu$ m or less, which is also traceable to NIST.

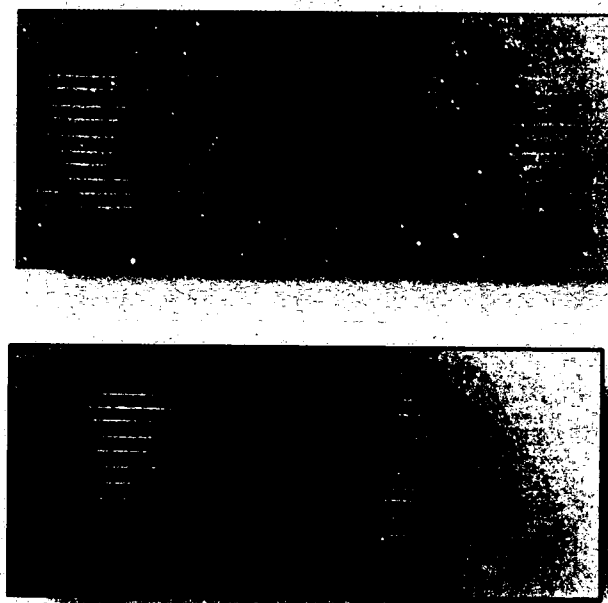


**Figure 3.6** DT optical microscope results using Nomarski DIC and image processing for better viewing purposes for (Top) semi-insulating SiC; (Bottom) conducting SiC. Image processing was performed in order to better resolve the modified surface lines.

Here, the subsurface gratings result in the  $2.5\mu\text{m} \times 190\mu\text{m}$  *predicted* line spread is shown from the AFM to be  $\sim 5.5\mu\text{m}$  wide  $\times 210\mu\text{m}$  long for the semi-insulating SiC and  $\sim 3.3\mu\text{m}$  wide  $\times 193\mu\text{m}$  long for the conducting SiC sample. The line spread (for semi-insulating and conducting both) decreases in both axes as the fluence/energy is decreased until the point where no visible damage occurs. The semi-insulating SiC sample results in more columns of modified lines which are due to it having a lower threshold than the conducting SiC sample. The processed lines, on both SiC types, were analyzed using the Nomarski DIC mode on the optical microscope (set in reflection mode). AFM imaging will give a more precise measurement of the line spread morphology, which will be shown in Chapter 6.

We conclude in this chapter that there are only two observable differences between the two SiC types (even the samples visual appearance is similar), which are the UV-Vis absorption at  $\sim 630\text{nm}$  and the morphology after being femtosecond laser processed. The linear, nonlinear, and DT properties remain familiar to one another. The values of all the measured parameters vary within 20% of each other except for the high NA DT values which gives a 45% difference between semi-insulating and conducting types.

### 3.5 Grating Production

Our method of micromachining gratings, using the anamorphic lens, distributes the ultrafast (UF) laser pulse from a  $5.5\text{mm}$  round Gaussian distribution to a  $2.5\mu\text{m}$  by  $190\mu\text{m}$  line shape. Each individual grating line consists of three separate line pulses exposed in sequence along the x-direction and 25 lines in the vertical, equating to  $\sim 500\mu\text{m} \times 500\mu\text{m}$  grating. These gratings are typically about  $1\mu\text{m}$  to  $5\mu\text{m}$  deep below the surface. Figure 3.7 shows a  $500\mu\text{m} \times 500\mu\text{m}$  grating in semi-insulating SiC with a spacing of  $20\mu\text{m}$ .

The anamorphic line distribution processed gratings into the SiC semi-insulating sample, which were analyzed using optical microscopy and Atomic Force Microscopy (AFM) to understand the morphology of the index modified structures. The grating lines are on or just below the surface ( $\sim 5\mu\text{m}$  to  $10\mu\text{m}$ ), and the modifications deform the surface such that the machined regions protrude up from the surface. Figure 3.7 shows a 10X and 50X images illustrating a good overlap of the grating lines.

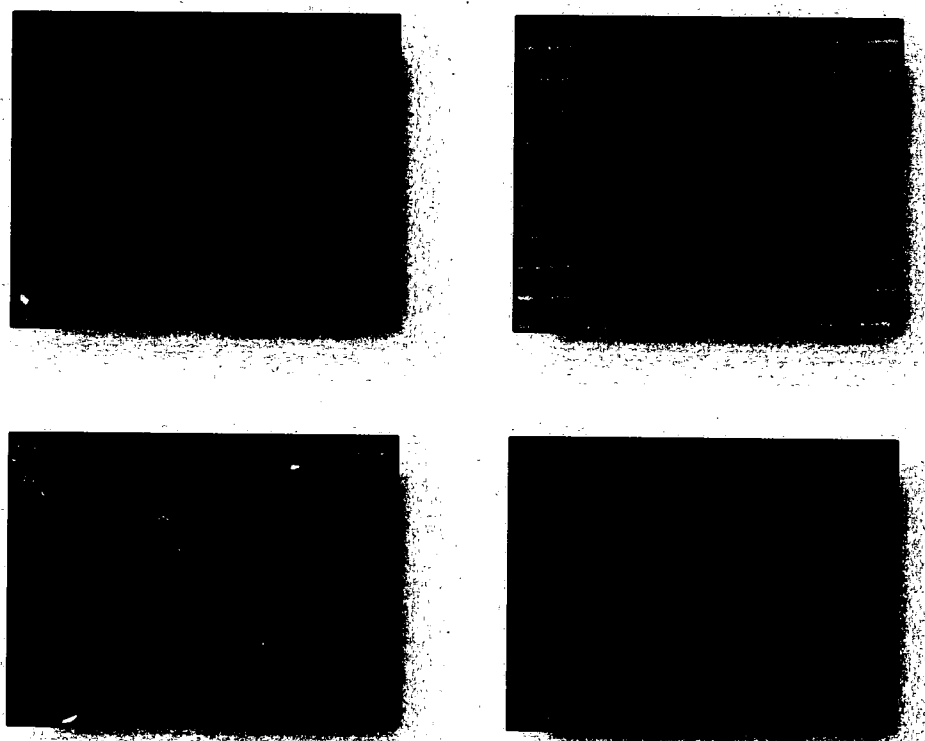


**Figure 3.7.** (Top) SiC grating view with an optical microscope using Nomarski DIC for (left) semi-insulating SiC on a 10X magnification; (right) 50X magnification. (Bottom left) shows the surface of another SiC sample, and (bottom right) shows just 5µm below the surface. Image processing was performed in order to better resolve the modified surface lines.

For these images, the optical microscope used is an Olympus upright digital BX51 microscope with Nomarski DIC (Differential Interference Contrast) capabilities that use high contrast prisms to produce increased contrast/resolution. This microscope also has measuring capabilities to  $\pm 0.25\mu\text{m}$  or less, which is also NIST traceable. The optical microscope reveals that the *predicted* line spread was found experimentally to be  $\sim 4.5\mu\text{m}$  wide x  $210\mu\text{m}$  long for the semi-insulating SiC sample with a surface grating, but a  $\sim 3.5\mu\text{m}$  wide x  $190\mu\text{m}$  long grating for the subsurface grating. The processed gratings were analyzed using the Nomarski DIC mode on the optical microscope in reflection mode.

## **CHAPTER 4**

### **Performance Evaluation of Grating Structures**

This chapter contains the performance and evaluation of the grating structures micromachined in amorphous and crystalline materials as described in Chapter 3.

Characterization of the grating structures is important for two reasons. One is so we understand that these gratings are of decent quality and to know the type of gratings structure manufactured; in this case volume phase gratings were fabricated.

Understanding of the type of grating and the morphology will enable a theoretical model to be fashioned. The second reason is to measure and use the diffraction efficiency of the optimum grating to approximate the magnitude of the index change,  $\Delta n$ . This chapter will encompass optical microscopy to visually understand the morphology, Fourier transform analysis used to model the grating structure, and diffraction efficiency measurements used to approximate the  $\Delta n$ .

#### **4.1 Optical Microscopy**

The optical microscope used is an Olympus upright digital BX51 microscope with Nomarski DIC (Differential Interference Contrast) capabilities that use high contrast prisms to produce increased contrast/resolution. This microscope also has measuring capabilities to  $\pm 0.25\mu\text{m}$  or less, which is also NIST traceable. The processed gratings were analyzed using the Nomarski DIC mode on the optical microscope (set in reflection mode). Nomarski DIC provides a spatial relationship and phase difference between

ordinary and extraordinary wavefronts and is governed either by the position of the objective prism (Nomarski DIC) or the relationship between the polarizer and a thin quartz retardation plate. Therefore, specific phase differences are made obvious while other scattering sample imperfections are less obvious. Phase differences can then be attributed to index changes from the bulk and the processed regions.

The processed sample areas were investigated directly after being development and later at the following dates: 1, 3, 6, and 12 months later. It will be shown how the amorphous versus crystalline materials differ with time and annealing.

#### 4.1.1 Soda Lime Glass Optical Microscope

Soda lime glass samples were processed with gratings and the optical microscope images show subsurface structures as shown below Figure 3.7.

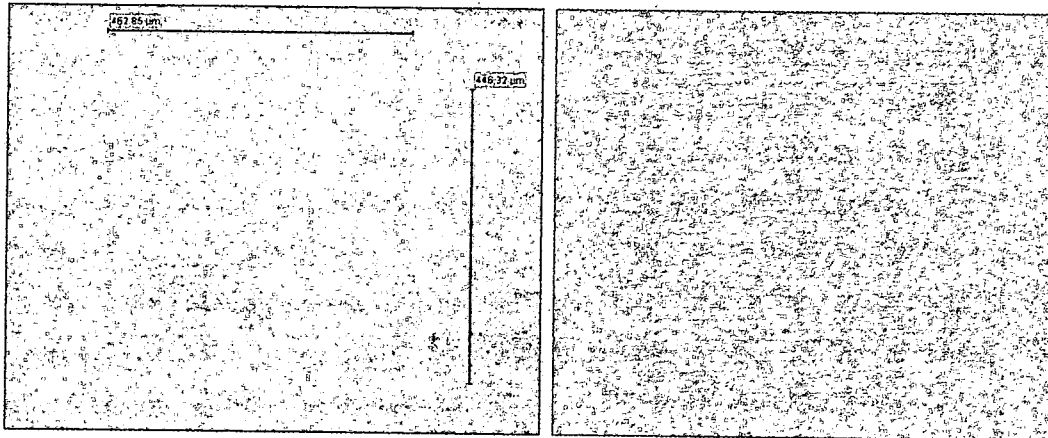


**Figure 4.1: SLG grating structures view with the optical microscope. On the left is the actual 10x image for a 450 $\mu$ m x 450 $\mu$ m grating with a 10 $\mu$ m grating spacing, and a 3 $\mu$ m line thickness. On the right is the same grating after post image processing to better view the structure.**

Figure 4.1 shows an example of a SLG subsurface grating at 10x magnification. These gratings actually consist of three micromachined lines in sequence with  $\sim 5\mu\text{m}$  overlap. The lines are  $3\mu\text{m} \pm 0.25\mu\text{m}$  thick and about  $0.5\mu\text{m}$  deep (grating line depth will be discussed in Section 6.6). The fluence used was  $2.8 \text{ J/cm}^2$  (single pulse) and resulted in a measured 1<sup>st</sup> order diffraction efficiency of 0.4% to 0.5%. Many gratings were micromachined in SLG that appear very similar to this grating; therefore not all of them will be shown.

#### 4.1.2 SiC Optical Microscope

Images illustrating the morphology of surface and subsurface gratings processed in SI SiC are shown earlier in Figure 3.7. The optical microscope reveals that the *predicted* line spread was found experimentally to be  $\sim 4.5\mu\text{m}$  wide x  $210\mu\text{m}$  long for the semi-insulating SiC sample with a surface grating, but a  $\sim 3.5\mu\text{m}$  wide x  $190\mu\text{m}$  long grating for the subsurface grating. Additional color Nomarski DIC images were taken of the SiC SI processed lines to show if color images present any insight on the morphology and to investigate if the grating lines degraded over time as well as being annealed as the soda lime glass gratings did and this will be discussed in further detail in a later section in this chapter.

#### 4.2 Fourier Analysis

The following is a more detailed description of the Fourier transform of the micromachined gratings and the Matlab code used to analyze the theoretical results. The



gratings micromachined are in fact a series of thin anamorphic lines in series with slight overlap between the tails of the lines.

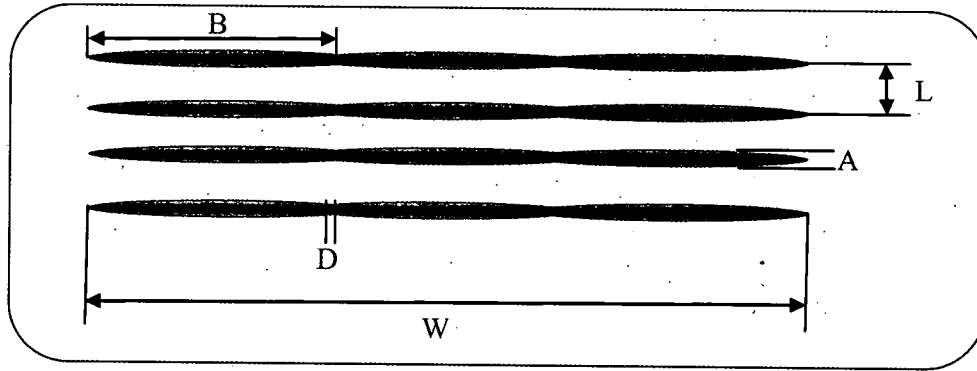


**Figure 4.2: Grating dimensions: A = 20 $\mu$ m, B = 190 $\mu$ m (consisting of 3 separate overlapped anamorphic lines), C = 3 $\mu$ m, D = 2-5 $\mu$ m, W = 500 $\mu$ m.**

In Figure 4.2 the gratings consist of three lines overlapping in series formed from a single circular femtosecond pulse transformed by the anamorphic lens. The diffraction pattern observed is in the far-field since it satisfies the Rayleigh range requirement.

$$Z_R = \frac{2 \cdot D^2}{\lambda} \quad \text{Equation 4.1}$$

Here D is the diameter of the beam, and in this case the width of the grating is essentially the size of the 632nm HeNe focused onto the grating, which is 500 $\mu$ m. The Fourier transform of the diffraction pattern is was analyzed in Matlab and that code is shown here.

```

% SiC Grating Fourier Problem
% Mark Burky and Logan DesAutels Dec 13 2007

clear all
close all

A = double(3*10^(-6));%Gaussian X - Width
B = double(190*10^(-6));%Gaussian Y - Width
dx = double(22*10^(-6));%X Grating Spacing
dy = double(180*10^(-6));%Y Spacing
L = double(500*10^(-6));%Grating Dimension
H = double(825*10^(-6));%HeNe Illumination Gaussian Width
lam = double(632.8*10^(-9));%HeNe Wavelength
z = double(1);%Distance to Screen - Probably want to leave this alone

T = 501; % Image is TxT pixels

x = linspace(-L,L,T);
y = linspace(-L,L,T);

[V,X] = meshgrid(y,x);

background = zeros([T T]);
% Initialized ta matrix to zero
Gauss = background;

% For loop calculates the Gaussian at each grid position and sums to
% provide ta.
for n = 1:3;

    for m = 1:18; % Must be odd integers.

        xo = (m-18)*dx;
        yo = (n-2)*dy;

        Gauss = Gauss + exp(-pi*(((X-xo)/A).^2 + ((Y-yo)/B).^2));

    end
end

% HeNe Gaussian Illumination
outergauss = exp(-pi/H^2*(X.^2+Y.^2));

% ta illuminated by HeNe
ta = Gauss.*outergauss;

% Normalization
norm = max(ta(:));
ta = ta/norm;

figure(1)
%im(ta);
imagesc(ta,[-0.25 1]);
colormap(gray);
axis off

% FFT of illuminated ta shifted and squared for intensity
ff = abs(fftshift(fft2(ta,2048,2048))).^2;

%im(ff,1,1,1)

% Zord cuts out the desired rectangle of the fraunhofer diffraction
% pattern

Zord = ff([1024-600:1024+600],[1024-400:1024+400]);

figure(2)
%im(Zord,1,1,.5);
imagesc(Zord,[-50000 200000]);
colormap(gray);
axis off

%improfile %use this to draw a line out.

```

### 4.3 Diffraction Efficiency

Gratings were chosen as the structure of choice to be micromachined for two primary reasons:

1. To construct FBGs into fiber optics without having to remove the cladding from the core and without having to dope the core with UV sensitive dopant.
2. To measure  $\Delta n$  indirectly from grating diffraction efficiency, DE, measurements.

Here the analysis of the DE results will be used to measure the  $\Delta n$  and any other observations pertaining to the physics of the femtosecond index modification. In this section various fabrication scenarios were investigated, and then from the data collected from each of these scenarios  $\Delta n$  could be calculated. Fabrication scenarios of the SiC gratings consisted of the following:

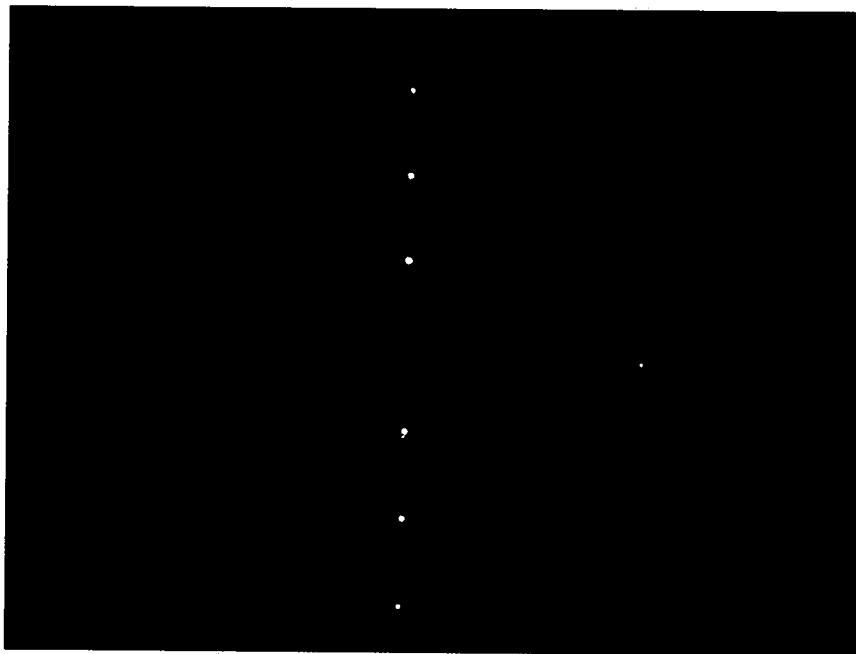
1. Variable energy.
2. Variable pulses for each energy tested.
3. Variable grating spacing at constant energy and number of pulses.
4. Semi-insulating versus conducting SiC samples.

Each of the above was evaluated and shown in the following sections.

#### 4.3.1 DE versus Grating Spacing and Number of Pulses

The DE was varied with grating spacing,  $d$ , and number of pulses for two reasons. First, to show that the gratings micromachined were of good quality and to compare with theoretical gratings results. The second reason was to find the correct receipt producing the most efficient gratings to calculate the magnitude of  $\Delta n$ . However, only the DE for gratings with 2-6 pulses was exploited for the calculation of the  $\Delta n$ . One pulse data is not

shown because during this experiment the femtosecond laser system happen to be experiencing pulse degradation and the single pulse gratings were lacking index modulation to induce a large enough diffraction efficiency. An example of the diffraction pattern is now given below to illustrate the complex pattern caused from the micromachined grating lines overlap.



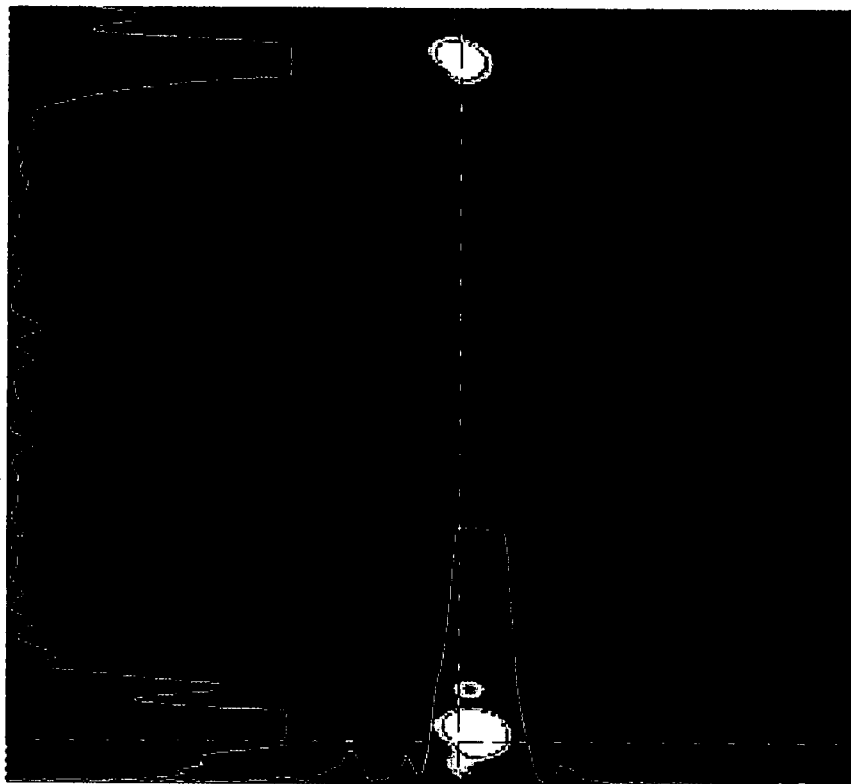


**Figure 4.3: Top shows SiC grating diffraction pattern using a HeNe beam and viewed onto a business card, while Bottom shows the same image only with using the Cohu 4812 CCD camera and Spiricon software.**

In Figure 4.3 (Top) the diffraction pattern has a distinctive pattern easily viewed with the unaided eye. This picture shows a typical pattern we observe when the pattern is projected onto a card with the zero-order blocked using a common digital camera. The bottom image cross-section represents a saturated profile. The saturated profile matches the theoretical profile. The image is saturated to allow a visualization of the structure between the peaks. This structure matches the theoretical profile as shown in the following figure below.

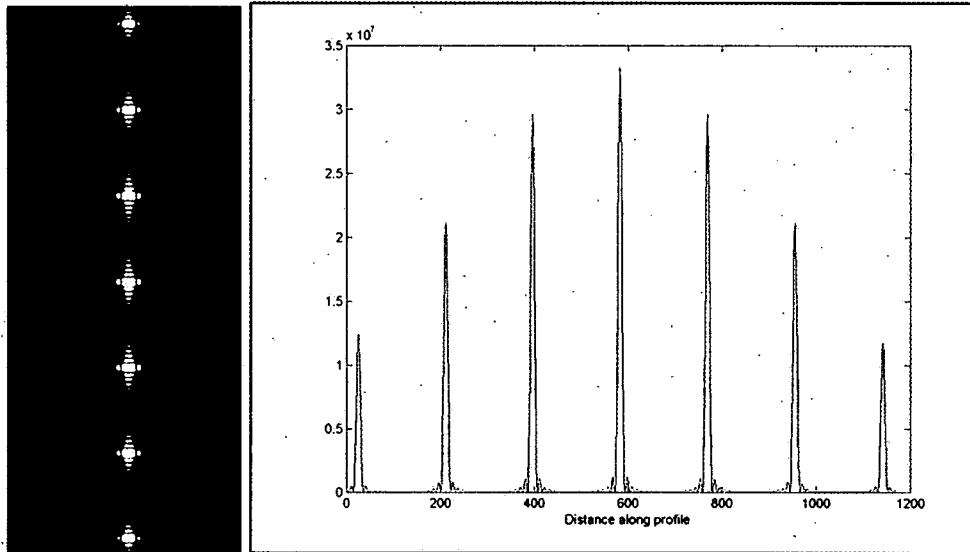


**Figure 4.4: Theoretical Fourier transform image and line out of the micromachined gratings.**

In Figure 4.4 the image is nearly exactly the same as the measured using a CCD, and the lineout of the theoretical is scaled in A.U. units to  $\times 10^7$ , which represents the saturated CCD image. As observed, the number of sub-order lobes matches that of the measured CCD image as well.

The optimal diffraction efficiency (DE or  $\eta$ ) was determined by manufacturing a series of gratings with varying spacing,  $d$ , ranging from  $3\mu\text{m}$  to  $50\mu\text{m}$ . A typical diffraction efficiency measurement output is shown in Figure 4.5. This DE output in Figure 4.5 shows the 0-order and diffracted beams resulting from a HeNe laser at  $632.8\text{nm}$ ,  $1.5\text{mm}$   $1/e^2$  beam diameter, and  $1.5\text{mW}$  output power. A long focal length lens was used to keep the HeNe beam diameter close to  $500\mu\text{m}$ , which is roughly the size of the grating structures. The HeNe beam power and diameter were measured with Spiricon software and a Cohu 4812 CCD camera in the absence of the gratings. The  $+1$  and  $-1$  orders were verified that they contained the same power within  $\pm 5\%$ . However, for the diffraction

efficiency calculation only one of the orders were measured (the +1 order) and a factor of 2 exist in the diffraction efficiency ( $\eta$ ) calculation in Equation 4.2.

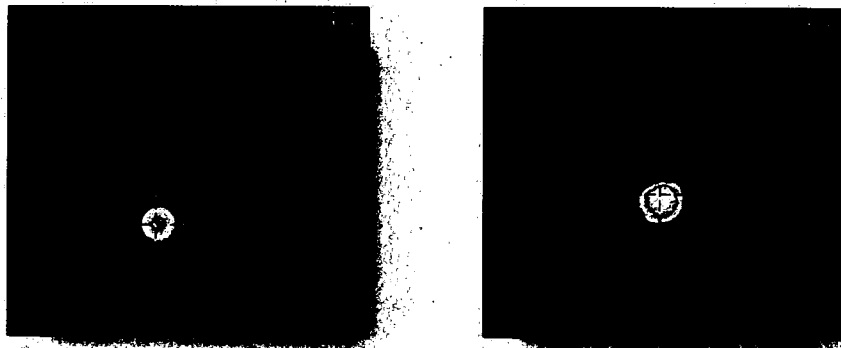


**Figure 4.5:** This figure depicts the input 632.8nm HeNe beam and the resulting SiC diffraction pattern of the first order. On the right is the 0-order beam and on the left is the first-order diffracted beam.

Figure 4.5 shows on the left the 0-order beam after propagating through an unprocessed portion of the sample. There are slight higher-order diffraction rings in the 0-order image that are caused from minor surface imperfections. The 0-order beam appears to be dimmer only because of the relative camera calibration and due to a larger ND used. On the right is the 1<sup>st</sup>-order diffraction beam, which has a structured diffraction pattern caused by the grating structure itself. Since the grating consist of three separate lines that slightly overlap, as stated earlier, this causes a superimposed diffraction pattern in the far-field (2 feet from the grating). The 1<sup>st</sup>-order appears more intense simply because of the lesser ND value used on the camera.

The diffraction efficiency of the 1st order diffraction pattern in Figure 4.5 was calculated by first measuring the power of the 1st order then using the following equation,

$$\eta = \frac{2 \cdot P_1 \cdot 10^{-(ND_0 - ND_1)}}{P_0} \cdot 100. \quad \text{Equation 4.2}$$

In Equation 4.2,  $P_1$  is the power of the 1st order measured beam,  $P_0$  is the power of the zero-order beam,  $ND_0$  is the neutral density filter OD placed in front of a Cohu 4812 camera when measuring the zero-order beam (no grating present only the unprocessed sample), and  $ND_1$  is the neutral density filter OD placed in front of the Cohu camera while measuring the 1st order diffraction beam. Neutral density filters were needed to keep the CCD camera from saturating.  $P_1$  and  $P_0$  are measured using Spiricon laser beam analyzer (LBA) software with a Cohu 4812 CCD camera, which is calibrated using a Coherent FieldMax II TOP meter with an OP2-VIS detector (both traceable to NIST). Equation 4.2 was used to calculate the diffraction efficiency for each grating fabricated.

The uncertainty in the diffraction efficiency measurement was determined using standard propagation of uncertainties. The uncertainties are primarily from the FieldMax meter, which has  $\pm 1\%$  accuracy, and the neutral density filters ( $ND_0$  and  $ND_1$ ) that are  $\pm 4\%$ . The OP2-VIS detector has  $\pm 5\%$  calibration uncertainty, but since we are taking relative measurements (or the ratio of  $P_1$  to  $P_0$ ) the 5% can be negated since it cancels. Therefore, the overall error in Equation 12 is taking into account the  $\pm 1\%$  for the meter accuracy and  $\pm 4\%$  for the ND values. From standard error analysis the uncertainty in the diffraction efficiency is  $\pm 5\%$  or less.

Figure 4.6 demonstrates how the diffraction efficiency peaks at a grating spacing of  $4\mu\text{m}$ . The diffraction efficiency was measured using a HeNe 632nm laser aligned nearly perpendicular ( $0^\circ$  to  $5^\circ$ ) to the micro-machined grating and to the c-axis of the SiC crystal. Once the HeNe beam passed through the grating the 1<sup>st</sup> order diffracted beam

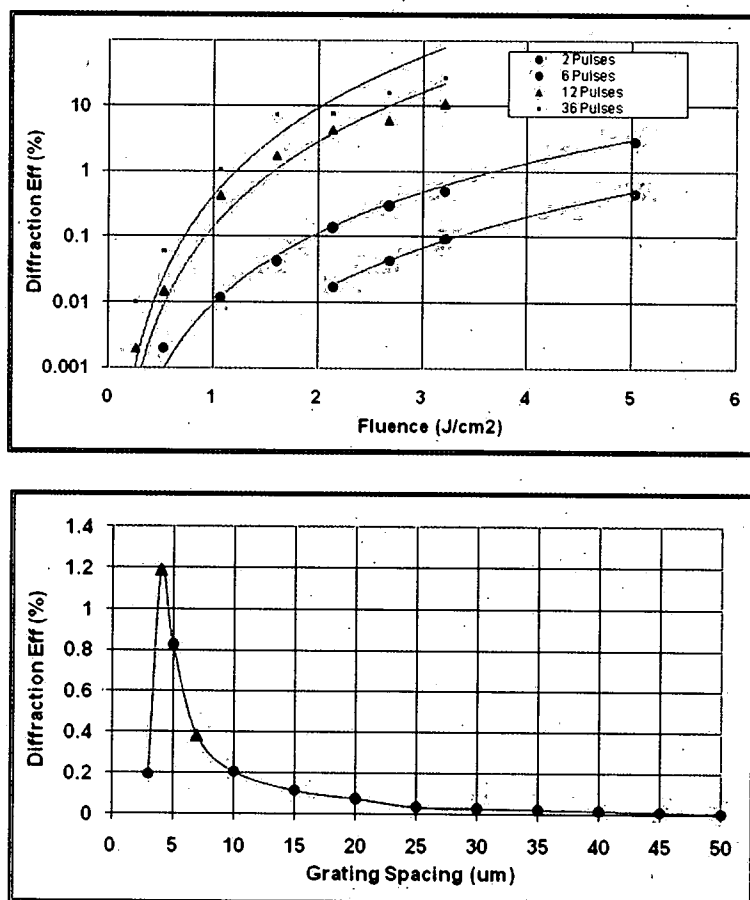


was measured by a camera roughly 2 feet away. The diffraction angle, power, and the image of the 1<sup>st</sup> order beam for each grating were measured at the same distance of 2 feet. These diffraction efficiency results are primarily shown here to illustrate the efficacy of the gratings generated using this anamorphic lens technique.

This new way of processing transparent bulk materials and grating structures using an anamorphic lens design enables a single femtosecond pulse to modify the surface and/or subsurface with a change in the bulk index of refraction. The theoretical anamorphic lens design agrees well with the experimental characterization of  $M^2$  and NA results. The gratings manufactured are  $\sim 500\mu\text{m} \times 500\mu\text{m}$  and are easy to acquire good alignment of the individual line pulses. Optical microscopy and AFM results show the morphology of these grating lines to be in good agreement with the predicted results. However, depending on the subsurface depth and type of substrate irradiated, a protrusion will form above the surface, which causes broadening of the machined line width. The diffraction efficiency results illustrate the performance of the gratings fabricated in SiC, which show the gratings produced are of good quality. One functional application for this technique is manufacturing fiber Bragg gratings (FBG).<sup>20</sup> This technique can generate gratings without removing the cladding, using a phase mask, or adding dopant to the fiber to react to the UV interfering beams to create the FBG.

Figure 4.3 gives the results of using a HeNe 632.8nm beam and the output SiC diffraction pattern. Each of the above was evaluated by charting the diffraction efficiency verses energy, number of pulses and grating spacing. In Figure 4.6 (Top), the diffraction efficiency of semi-insulating SiC for 6 pulses is  $\sim 0.6\%$ , whereas for 36 pulses shows a

max diffraction efficiency of ~28% in the same semi-insulating SiC sample. The gratings comprised of 12-36 pulses are a combination of amplitude and phase modulations causing higher diffraction efficiency than if they were merely phase induced. However, the gratings comprised of 1-6 pulses result in only phase modulations, which are used in the  $\Delta n$  calculations. In other words, the gratings at lower energies and pulses are subsurface only, which induces the phase of inspection HeNe laser wavefront to be modulated. In contrast, the gratings at higher energies and pulses have surface damage that causes amplitude as well as phase modulation to the laser wavefront.



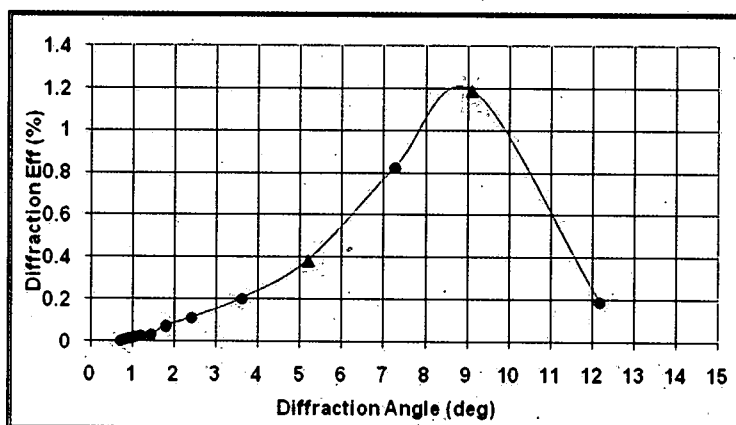


Figure 4.6: (Top) DE versus fluence for 2, 6, 12, and 36 pulses, (Middle) DE versus grating spacing, and (Bottom) DE versus diffraction angle. The red data points (triangle) are the data that was filled in at a later date to verify the trends.

Figure 4.6 (Middle) shows how the diffraction efficiency varies with the grating spacing, and Figure 4.6 (Bottom) represents the DE with varying grating diffraction angle of the 1<sup>st</sup> order. Figure 4.6 (Middle) and Figure 4.6 (Bottom) suggests that the type of grating structure we manufactured is a volume phase grating,<sup>21</sup> as well as the quality of the volume gratings are acceptable since Figure 4.6 resembles the trends attributed to standard volume phase gratings. Also, Figure 4.6 (Middle) and Figure 4.6 (Bottom), show two red triangle data points which represent data added at a later date. This data was added to confirm the trends and to show repeatability in the grating fabrication. As observed, gratings added to this substrate at a later date and alignment show consistent results. Our grating structures are typically 0.5 microns deep (as measured and shown later with TEM) and just below the surface resulting in a phase modulation only.

A phase modulation grating is when only an index change,  $\Delta n$ , inside the bulk material has occurred, whereas, an amplitude grating is caused by surface damage/obliteration similar to a Ronchi-ruling grating (opaque lines over a transparent substrate). It is

believed that for the subsurface grating most or all diffraction efficiency is contributed to phase or index changes.

The trends for the diffraction efficiency versus energy/fluence plot, in Figure 4.6 (Top), indicate that the efficiency *may* “roll” off or reach peak efficiency then start decreasing, but this did not happen in the semi-insulating SiC sample. Instead the DE increased quadratically even as the scattered light increased. The scattering of the light should theoretically bring the DE down, but practically the diffraction efficiency increased at a much higher rate than the scatter. This increase in diffraction efficiency is due to surface damage caused by thermal breakdown of the chemical bonds leading to surface ablation, as well as the  $\Delta n$  of the increased anamorphic volume. The increase in the volume depth with higher energy exposure, basically, has a longer interaction with the HeNe 632.8nm beam, used to evaluate the diffraction efficiency, and the gratings  $\Delta n$ . As mentioned, the thermal breakdown leading to surface ablation decreases the diffraction efficiency due to scatter, but at a negligible rate as compared to the increased  $\Delta n$  volume.

Next, we tested conducting SiC samples for comparison with the semi-insulating samples. The conducting SiC sample had a very different reaction to the laser processing, in that, the diffraction efficiency verses fluence started to “roll off” as the fluence increased due to absorption and scattering from the surface damage – see Figure 4.7. Once the DT was reached on the conducting SiC sample (for 36 pulses) there was a very discrete threshold from no damage to extreme surface thermal breakdown – see Figure 4.8. At a slightly higher fluence level above the DT, the surface modifications were sporadic; leaving a discontinuous grating line with further increases would then

seriously and continuously create a solid surface modification that was black and/or opaque in color. This type of change is not desired, but we were not able to find the proper fluence level to allow for only an index modification.

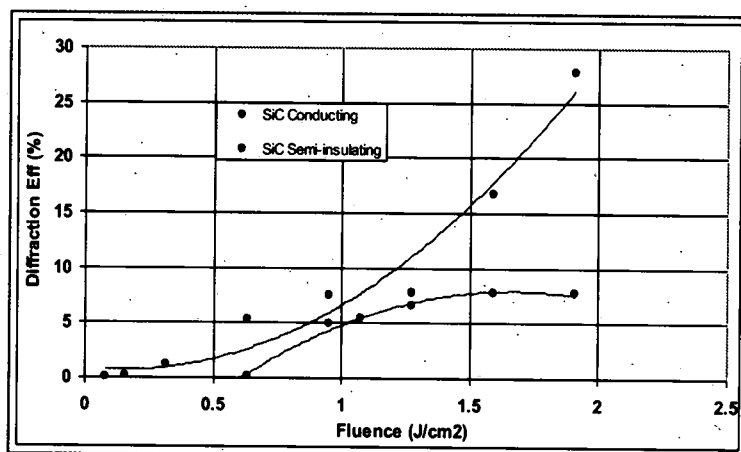


**Figure 4.7: Diffraction efficiency versus Fluence using 36 pulses comparing semi-insulating to conducting SiC.**

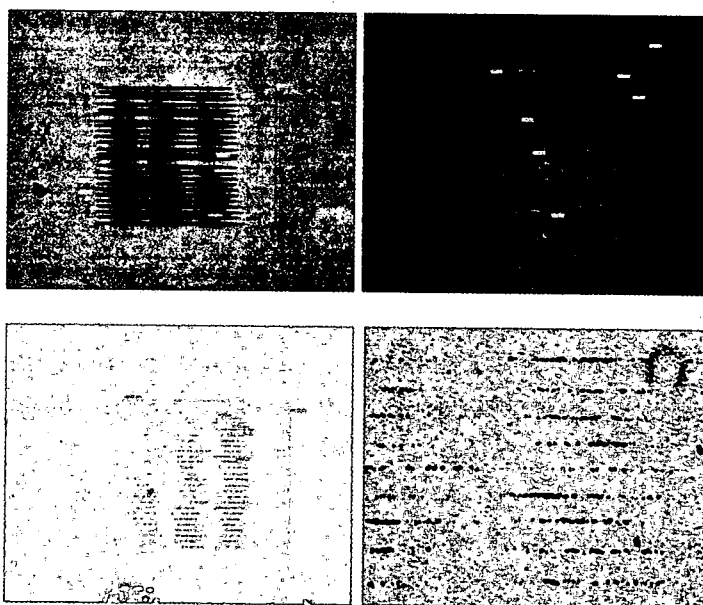


**Figure 4.8: Discontinuous and continuous grating lines micro-machined in conducting SiC. Top two pictures, grating made using 36 pulses, and the bottom two pictures, grating made using a single pulse.**

From Figure 4.7 and Figure 4.8 it is evident that the conducting SiC sample is more sensitive to the femtosecond radiation. The conducting sample has more thermal breakdown on the surface and is very sporadic for the single pulse gratings (bottom two pictures in Figure 4.8). Also, Figure 4.7 depicts this graphically by the “roll off” of the conducting SiC with increasing fluence. Also, Figure 4.7 shows how DE is zero and suddenly jumps to  $\sim 5\%$  in less than  $0.5 \text{ J/cm}^2$  representing the discrete threshold as described earlier.

#### 4.3.2 Change in Index of Refraction Magnitude Calculation

In order to perform  $\Delta n$  magnitude calculations, the structure has to have only phase changes and not amplitude changes. As seen above, using NSOM, TEM, optical microscope (with Nomarski capabilities), and AFM it is possible to determine the type of grating that is written. Samples where there is only a sinusoidal phase change (subsurface machining) are called volume phase holographic (VPH) gratings. The methods to determine the morphology of the VPH micromachined gratings are discussed in detail in various sections of this chapter.

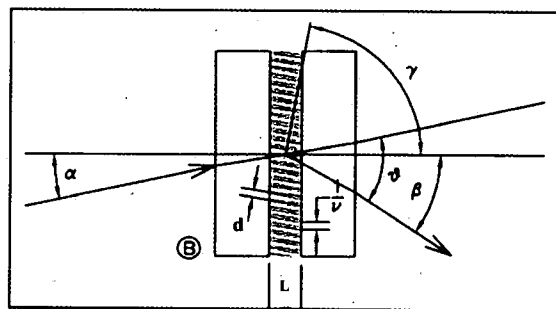


Figure 4.9: Transmission grating with index modulations at a given angle with respect to the input beam. This figure is provided by Barden *et al*<sup>22</sup>.

The diffraction efficiency,  $\eta$ , of a VPH grating for phase only modulation depends upon the thickness,  $L$ , the grating angle,  $\beta$ , with respect to the input beam, the  $\lambda$ , and  $\Delta n$  of the modulation.<sup>22</sup> This approximation assumes a sinusoidal structure, which is an acceptable estimate for this analysis.

$$\eta = \sin^2 \left( \frac{\pi \cdot \Delta n \cdot L}{\lambda \cdot \cos(\beta)} \right) \quad \text{Equation 4.3}$$

Here  $\beta$  is defined as the Bragg angle as is given as<sup>22</sup>

$$\beta = \sin \left[ \frac{n_{air}}{n_{SiC}} \cdot \sin(\alpha_i) \right] \quad \text{Equation 4.4}$$

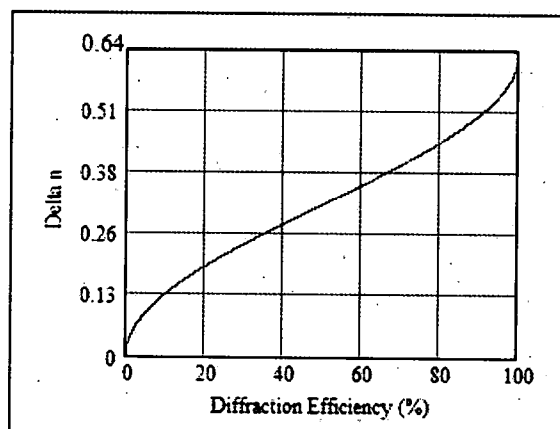
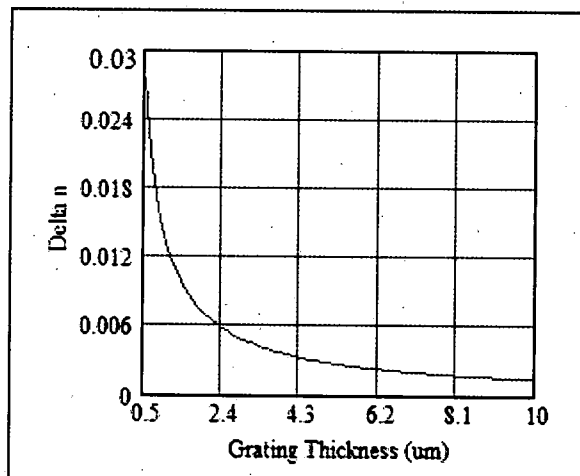
Where  $\alpha_i$  is the incident angle of the input beam that is dependent on the HeNe laser alignment and how well the sample was aligned to the femtosecond laser during the micro-fabrication process. Also,  $n_{air}$  is the index of air which is 1.0, and  $n_{SiC}$  is the average index of ordinary and extraordinary indices of SiC. The incident angle is therefore estimated to be under  $3^\circ$ , which provides a Bragg angle of  $\beta = 1^\circ$ . The Bragg angle,  $\beta$ , and incident angle do not have a large affect on  $\Delta n$ ; approximately 0.8% difference in  $\beta$  from  $0^\circ$  to  $20^\circ$ .

Knowing the diffraction efficiency from the 2-pulse efficiency curves, at  $5 \text{ J/cm}^2$  input fluence, in Figure 4.6 demonstrate  $\eta = 0.47\%$ . Now, if  $\Delta n$  is solved from Equation 4.3 above then we have,

$$\Delta n = \sin^{-1}(\sqrt{\eta}) \cdot \lambda \cdot \frac{\cos(\beta)}{\pi \cdot L} \quad \text{Equation 4.5}$$

Where  $\Delta n$  is found to be 0.03 for  $L = 0.5 \mu\text{m}$ ;  $L$ , as will be shown, is the modulation depth of the grating structures found using TEM. Previously, using the optical microscope, the

modulation depths were found to be  $\sim 5\mu\text{m}$  to  $10\mu\text{m}$ , but TEM morphology is trusted because there is more uncertainty with using the optical microscope due to the depth of focus (or Rayleigh range) of the objective. Next, using the above equations, the  $\Delta n$  was varied as a function of modulation depth. In addition,  $\Delta n$  was also plotted as a function of  $\eta$ ; both plots shown below.





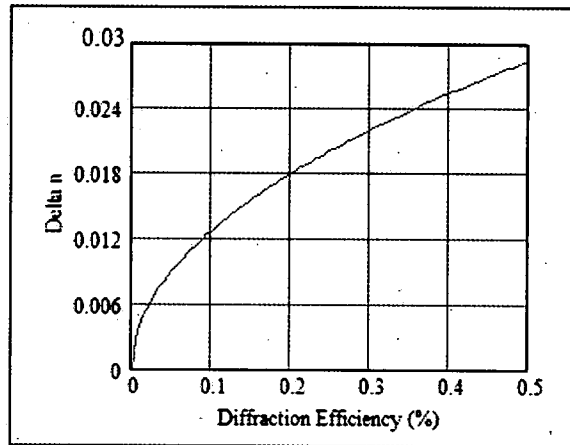


**Figure 4.10: (Top)  $\Delta n$  versus modulation depth, (Middle)  $\Delta n$  versus diffraction efficiency, and (Bottom) zoom of the middle chart –  $\Delta n$  versus  $\eta$ .**

As shown in Figure 4.10 the trend of  $\Delta n$  increases as the modulation depth decreases, which means that the index change has to be greater in order to achieve the same diffraction efficiency for a smaller depth. Also Figure 4.10 shows  $\Delta n$  increasing as efficiency increases, and shown is a  $\Delta n$  of 0.03 for 0.5% efficiency.

## **CHAPTER 5**

### **Index Change Morphology/Mechanisms**

In this chapter the morphology of the processed grating lines and the possible mechanisms of the index changes in amorphous and crystalline transparent bulk materials; soda lime glass and 6H-SiC samples respectively, are studied. Each section of this chapter discusses the techniques used to image and analyze the processed areas. The conclusion gives a collective view of what the best hypothesis is for the mechanism responsible for creating an index modification in bulk transparent materials using fs laser pulses. Grating structures in 6H-SiC semi-insulating (SI), 6H-SiC conducting and soda lime glass were machined with gratings and were analyzed/imaged with all of the following techniques.

#### **5.1 Raman Spectroscopy**

Raman spectroscopy is a technique which involves illuminating a sample with monochromatic light and using a spectrometer to examine the light inelastically scattered by the sample.<sup>24</sup> Photons interact with matter by means of absorption, transmission or scattering processes. Inelastic scattering is the mechanism for Raman spectroscopy. The incident laser excites a molecular vibration or rotation, hence losing energy. There is a frequency shift that occurs which corresponds to the energy difference between the source photon and the scattered photon (after interacting with the molecule). This frequency shift is known as the Raman shift. If the scattered photon experiences a gain

corresponding to the vibrational energy this correlates to an increase in frequency relative to the incident photon. Likewise, if the scattered photon experiences a loss due to exciting a vibrational mode vibrational energy this correlates to a decrease in frequency relative to the incident photon and is called a Stokes process. The gain in vibrational energy, or increase in the scattered frequency, is called the Stokes line, and a decrease in the scattered photon frequency is called the anti-Stokes line. Every material or element has its own vibrational mode and thus a characteristic Raman signature.

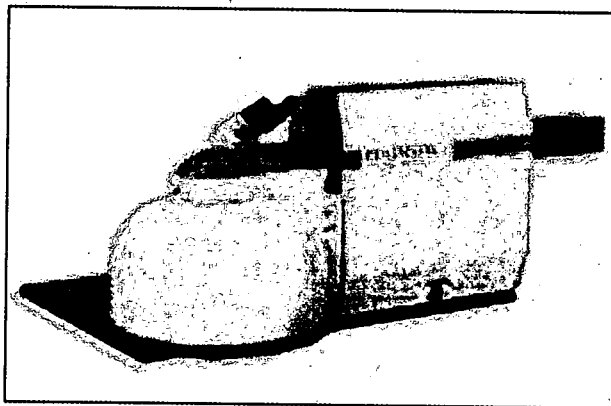


**Figure 5.1: University of Dayton Renishaw Micro-Raman system.**

The Raman experiments used a Renishaw micro-Raman system that has variable objectives. For these experiments a 100X objective was used to obtain a small spot size on the processed area.

Raman spectra were taken from both unprocessed and processed areas. As a baseline, the Raman data was also measured with fused silica to be compared to referenced fused silica Raman results<sup>23</sup> to confirm that our Raman results for SiC are valid.

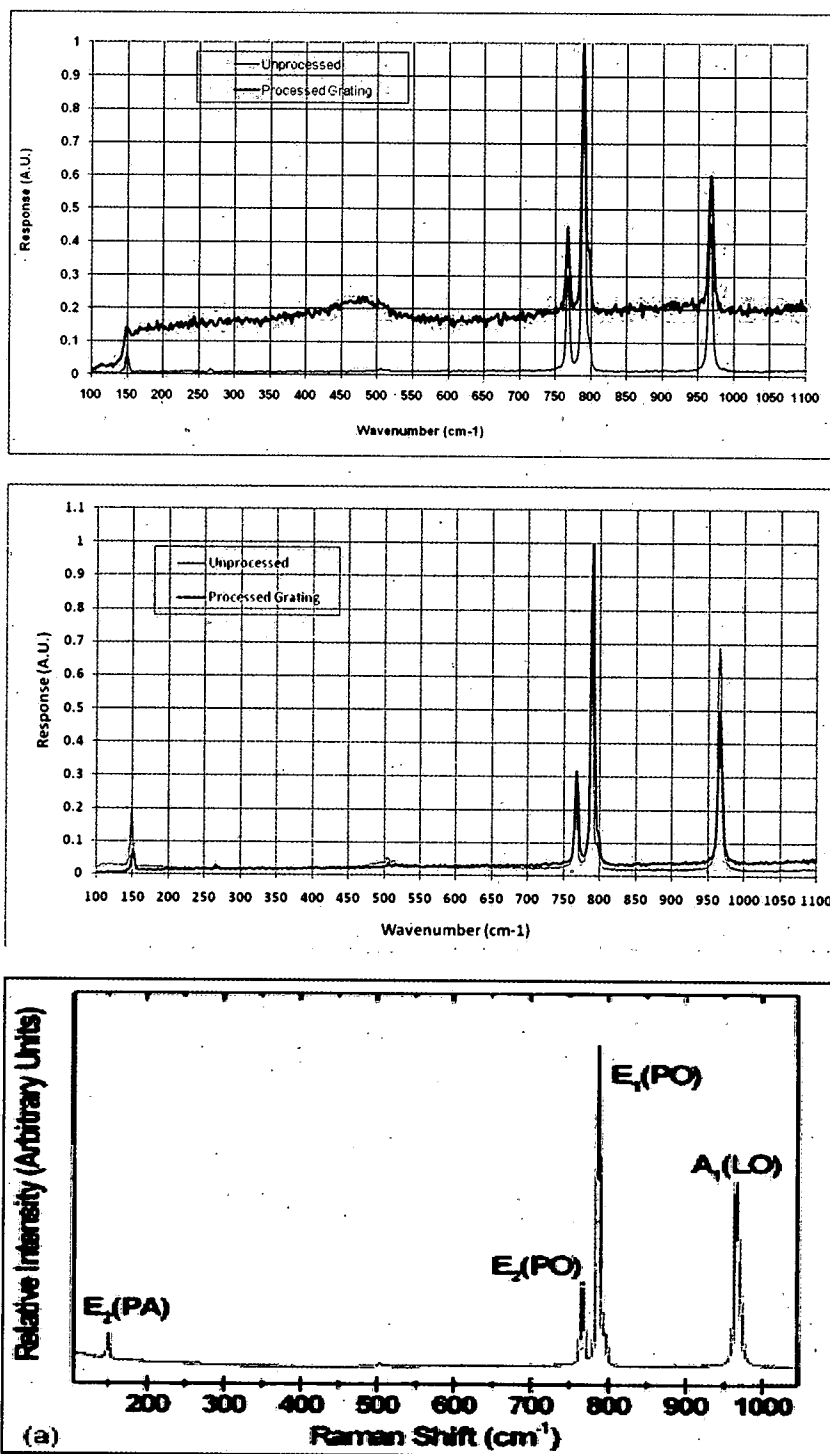


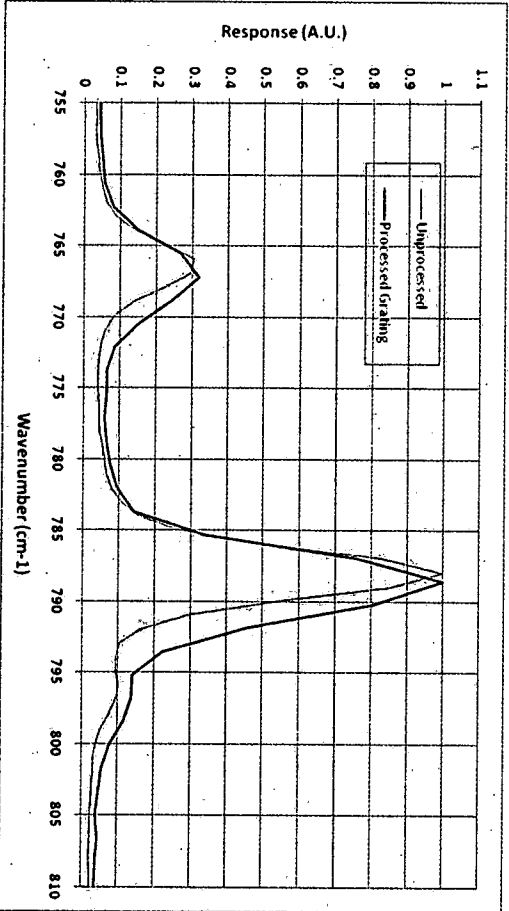
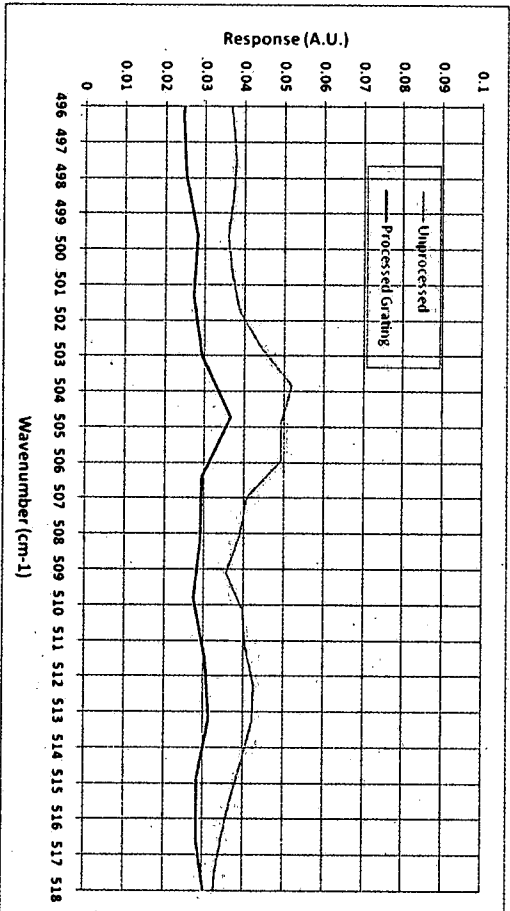
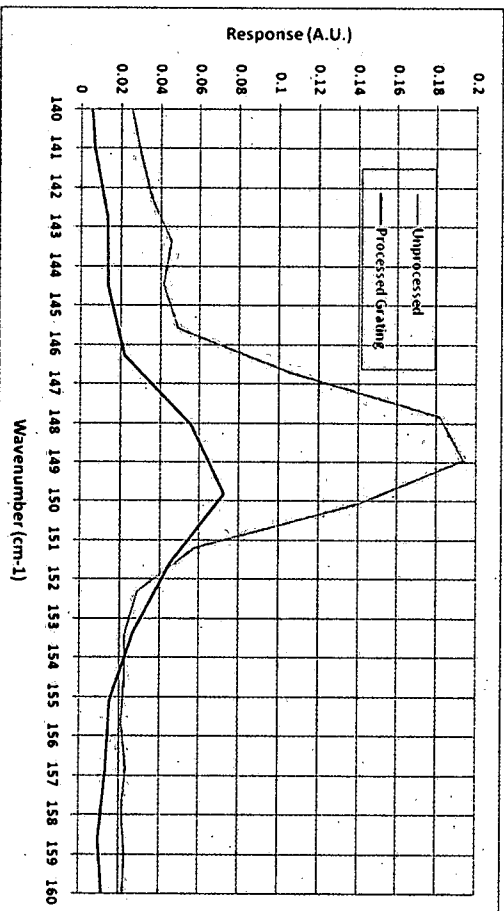
Figure 5.2: University of Dayton Raman Spectra on semi-insulating processed and unprocessed SiC: (Top) Raman using 514nm laser source and a 1800 line grating with fluorescence emission causing a slope in the trend and false-broadening of two or three of the peaks, (Middle) is a new Raman scan with the instrument set to use a “photo-bleaching” technique to subtract the fluorescence emission, (Bottom) is a 6H-SiC Raman from Burton *et al* 6H-SiC Raman spectrum.<sup>24</sup>

This Raman spectrum was performed in the semi-insulating SiC subsurface grating features and they primarily show a broadening affect and a slight shift that will be described momentarily. Figure 5.2 (Top) is shown to illustrate how fluorescence emissions in the processed region cause an overall slope in the trend and broadening of two or three of the peaks. Fluorescence emissions come from using a high power objective (to measure the 3 $\mu$ m wide grating features) that results in a high photon flux on the sample, where this flux creates elevated electronic and/or vibrational states after absorbing source photons. When the excited atoms lose their energy they drop to various vibrational energy levels and thus emit a mixture of photons each with different frequencies. The mixture of photons, or fluorescence, are additionally measured causing background noise. This fluorescence background contamination can be subtracted by using photo-bleaching and auto-baseline correction performed by the Raman instrument. Photo-bleaching is done by irradiating the sample under test with the intense source for a long period of time thus causing a chemical decomposition, which breaks down the molecules that are the cause for fluorescence. Auto-baseline is used to correct for the sloping background, which makes it difficult to interpret the spectrum. Therefore, with the Raman instrument set to photo-bleach and auto-baseline correction features, a new spectrum was collected as shown in Figure 5.2 (Bottom), which gives a 6H-SiC spectrum without the presences of fluorescence. In addition, the unprocessed Raman results are in absence of fluorescence because unprocessed SiC spectrum did not require a high power objective, thus the photon flux was low and no fluorescence was emitted.

The unprocessed semi-insulating (SI) 6H-SiC UD Raman was compared to a reference 6H-SiC Raman as shown in Figure 5.2, which shows that the UD SiC Raman agrees with referenced SiC Raman. The Raman peaks are described by Burton *et al* as an  $E_2$  planar acoustic mode at  $150.5\text{ cm}^{-1}$ , two planar optic or TO modes of  $E_2$  symmetry at  $767.5\text{ cm}^{-1}$  and  $788.0\text{ cm}^{-1}$ , and an  $A_1(\text{LO})$  phonon at  $966.5\text{ cm}^{-1}$ . Burton *et al* also mention that the mode at  $796.0\text{ cm}^{-1}$  is a planar optical mode of  $E_1$  symmetry, and there are two peaks around  $500\text{ cm}^{-1}$  (505 and 513), which are  $A_1$  axial acoustic LA modes.<sup>24</sup>

There are two polarization modes for crystals with at least two atoms. These modes are known as acoustical and optical modes with longitudinal and transverse phonons representing each mode. LA represents the longitudinal acoustic mode, TA represents the transverse acoustical, LO represents the longitudinal optical, and TO represents the transverse optical phonons.<sup>24</sup> The acoustic modes correspond to all the atoms moving together (as a wave of atoms) that generates a lower frequency. The optical modes correspond to the individual atoms oscillating independently with a much higher frequency.

Now, if the UD 6H-SiC Raman spectrum of the processed and unprocessed regions in Figure 5.2 (Middle) is expanded, we find the peaks are both broadened and shifted as shown in Figure 5.3.



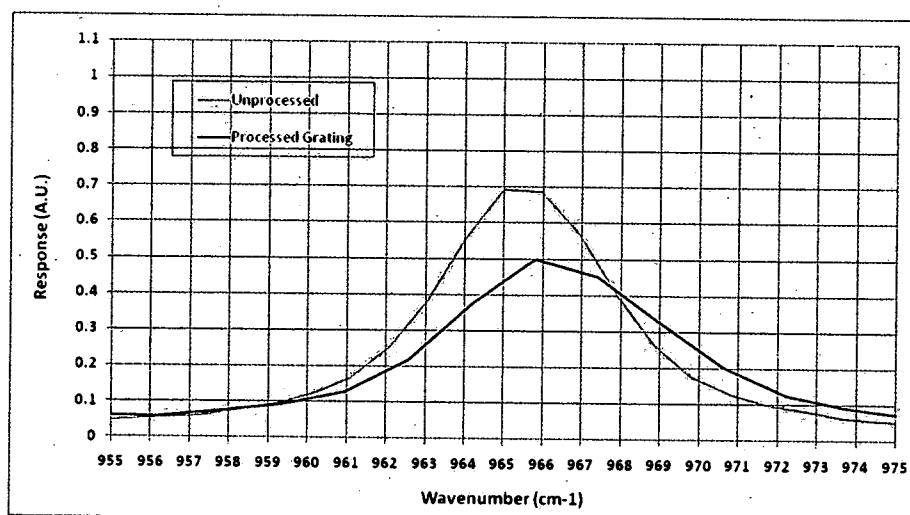


**Figure 5.3: UD Raman of 6H-SiC processed grating subsurface structure and unprocessed regions illustrating peak shifts and broadening: from top to bottom: 150  $\text{cm}^{-1}$  peak, 500  $\text{cm}^{-1}$  peak, 766  $\text{cm}^{-1}$  and 788  $\text{cm}^{-1}$  peaks, and the 965  $\text{cm}^{-1}$ .**

**Table 5.1: Processed and unprocessed SiC peak analysis is shown for Figure 5.3.**

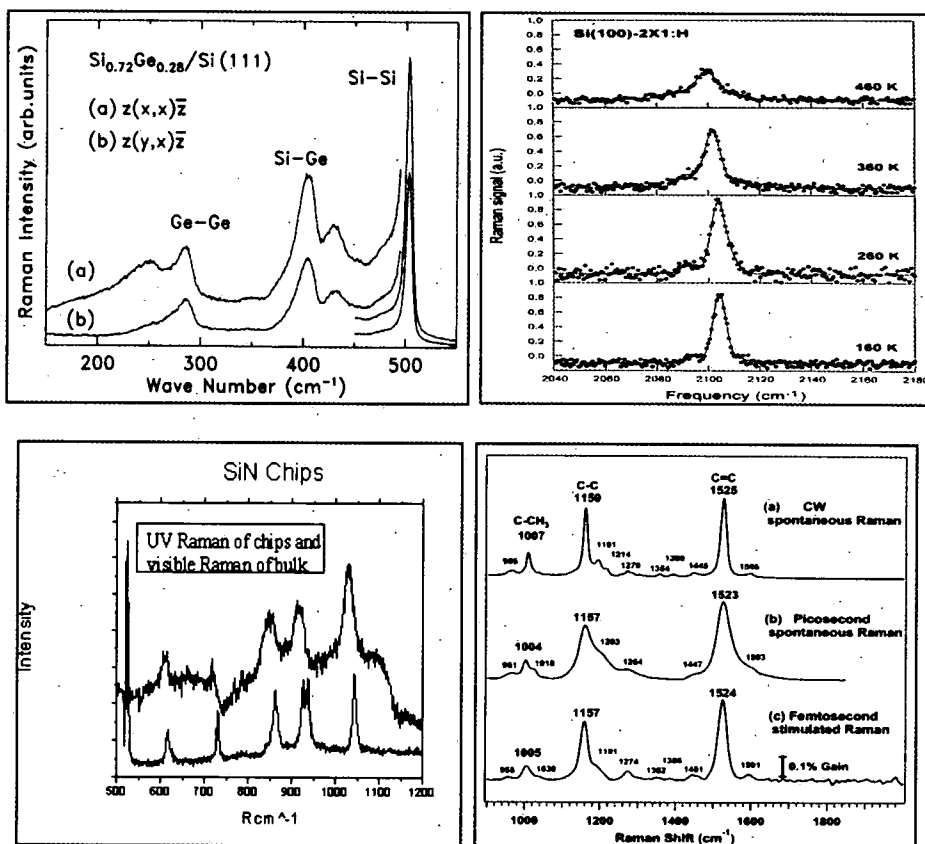
Unprocessed 6H-SiC Peak Raman Shift ( $\text{cm}^{-1}$ )	Processed 6H-SiC Peak Raman Shift ( $\text{cm}^{-1}$ )	Mode Symmetry <sup>24</sup>	FWHM Broadening ( $\text{cm}^{-1}$ )	Peak Shift ( $\text{cm}^{-1}$ )
148.5	149.34	$E_2$ Planar Acoustic	1.0	0.84
505, 513	505, 513	$A_1$ Axial Acoustic	0, 0	0, 0
765.9, 787.9	767.2, 767.2	$E_2$ Planar Optic	2.6, 0.9	1.3, 0.7
965.5	966.25	$A_1$ (LO)	1.5	0.75

Table 5.1 provides the Raman results for the unprocessed and processed 6H-SiC. This Raman spectrum suggests that a chemical change in the bond structure has not occurred since only the original 6H-SiC peaks exist. The Raman results were compared with other possible chemical combinations that could have possibly taken place. These probable reactions are stated below:



1. Si=Si
2. SiH
3. SiN
4. C=C
5. CN
6. CO
7. Graphite

With these combinations in mind, a literature search was done to determine if any of the above spectra could have a subtle presence in the processed SiC.



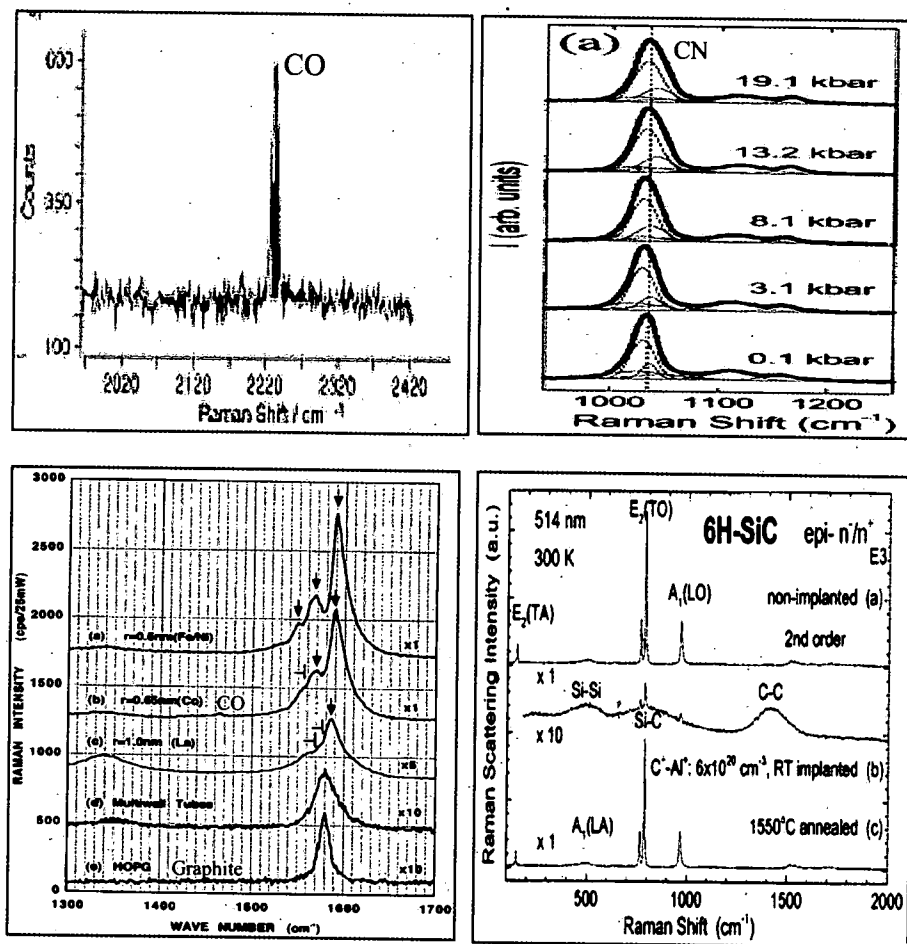


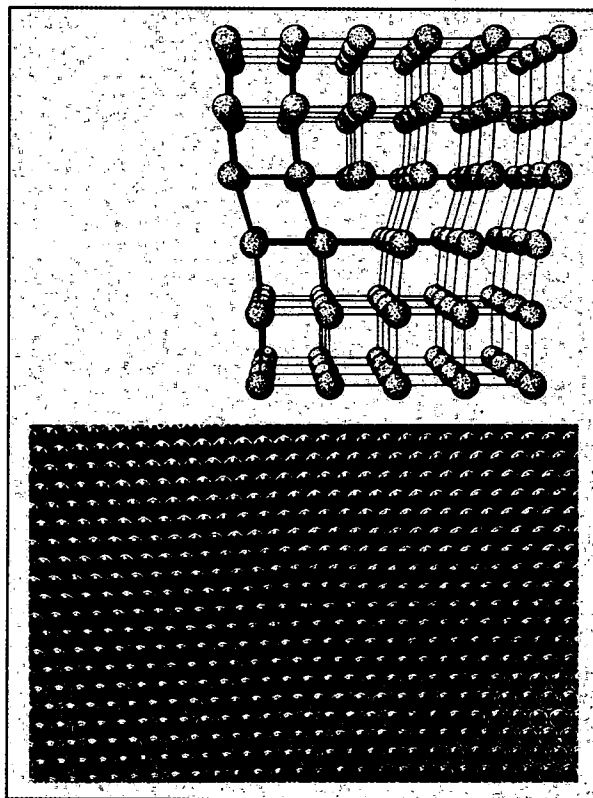
Figure 5.4: Raman spectra in order from the list of possible chemical reactions in the processed SiC specimen. From top left to bottom: Si-Si<sup>25</sup>, SiH<sup>26</sup>, SiN<sup>27</sup>, C-C<sup>28</sup>, CN<sup>29</sup>, CO<sup>30</sup>, Graphite<sup>31</sup>, and a 6H-SiC specimen with C-C reaction and also showing another common SiC peak at 1530<sup>32</sup>.

Figure 5.4 shows some of the plausible reactions that could occur with femtosecond laser processing of semi-insulating (SI) 6H-SiC. As is observed, none of the referenced peaks are apparent in the processed SiC sample. Therefore, it is concluded, from the Raman spectrum only, that the femtosecond laser processed SiC did not alter the chemical makeup, but only broadened and shifted some of the peaks of the spectrum.

Even though there are no new peaks that appear in the processed SiC spectrum, the broadened and shifted peaks, shown above in Table 5.1, do give evidence of an index

change in the processed regions. The broadened peaks represent a compression of the lattice atoms, which forces the dipoles to be in closer proximity with each other. Since the atoms are denser in the processed area this causes a broadening of the Raman scattered peak. If the atoms are perfectly spaced and there are no temperature variations exist then a delta-function peak will result in the Raman spectrum. Since there is temperature variations the Raman peaks have some width. However, if those atoms are compressed causing the atoms to vibrate as a group instead individually then the sum phonon frequencies will effectively broaden the Raman peaks additionally to the temperature.

The shift of the peaks represents a generation of phonons due to Brillouin scattering (sometimes known as Raman scattering),<sup>33</sup> named for Leon Brillouin, occurs when light in a medium interacts with lattice variations and changes its path. These variations may be due to acoustic modes, such as phonons.<sup>33</sup> If the medium is compressed, from an external source such as a femtosecond laser pulse, its index of refraction changes and this is illustrated in the figure below.



**Figure 5.5: Deformation of a crystal lattice that will cause a dislocation in the bulk medium, or an index of refraction change. This dislocation is seen in the center of the bottom image by tilting the page<sup>34</sup>.**

Therefore, the shift in the  $150\text{cm}^{-1}$   $E_2$  Planar Acoustic,  $766\text{cm}^{-1}$  &  $788\text{cm}^{-1}$   $E_2$  Planar Optic, and the  $966\text{cm}^{-1}$   $A_1$  LO SiC crystal lattice modes suggest a deformation in the lattice. The deformations change the dipole moments, where the photons now interact with these dipoles in their new locations which cause an effective index of refraction change.

## 5.2 X-Ray Crystallography

X-ray crystallography is a technique that uses an x-ray beam directed at a sample, which will be scattered by the electrons within the lattice structure. The scattered x-ray beam will then produce a diffraction pattern of recurring spaced spots as a two-dimensional output image. Taking the Fourier transform of this two-dimensional image will result in a three-dimensional model of density of electrons that represent the crystal orientation or the atomic lattice.<sup>33</sup>

The x-ray crystallography was performed on SiC SI to investigate any changes within the SiC crystal structure that might suggest that the index of refraction modifications done in this substrate are due to a change in the chemical structure of SiC either by broken bonds or new elements or impurities. Therefore, the areas in the SiC sample that have been processed should result in an altered diffraction pattern caused by the modifications in the crystal lattice as a consequence in the femtosecond pulse radiation.

A large area of the sample (about a 4mm x 4mm area) needed to be processed for this technique due to the size of the x-ray beam used to analyze. Therefore, in order to process a large area, a long focal length spherical lens was used (250mm focal length), which provided a 70 $\mu$ m focused spot diameter. To cover a large 4mm x 4mm area a matrix of 70 $\mu$ m damage spots were produced with slight overlap of the spots to fully fill the area. The damage test bed (DTB – used to measure the damage threshold of materials) was used to automate this since this matrix took ~12 or more hours to complete. Three different energy levels were used to create 3 different 4mm x 4mm processed areas – each was analyzed with the x-ray beam. The different energy levels

provided various morphology on the SiC sample – from surface damage to subsurface damage were thus examined by this x-ray technique. In addition, an unprocessed area of the SiC was also tested to provide a reference or comparison for the processed areas. The figure below shows the sample after being prepared for the x-ray crystallography experiment.

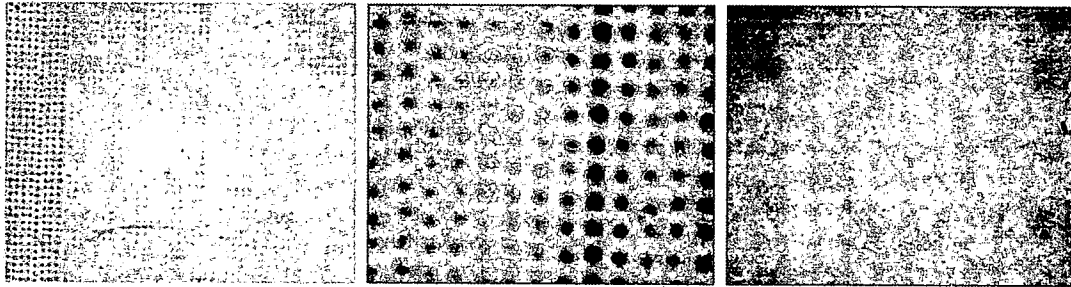


**Figure 5.6:** SiC sample after being prepped for the x-ray crystallography test. (Left) is energies 1, 2, and 3 at 5x magnification, (middle) is energy 1 area at 20x magnification, and (right) is energy 1 area at 50x magnification.

The energy levels used were: energy 1 ( $E_1$ ) = 40 $\mu$ J to provide a fluence of 2.2 J/cm<sup>2</sup>,  $E_2$  = 20 $\mu$ J for a fluence of 1.1 J/cm<sup>2</sup>, and  $E_3$  = 10 $\mu$ J for a fluence of 0.55 J/cm<sup>2</sup> (at or just above the damage threshold). The damage spots for the  $E_1$  level do overlap, but it is not easy to observe from the images in Figure 5.6. Overlapping of the damage spots is known after measuring the sample (shown in Figure 5.6) using an optical microscope and a 50x objective.

The x-ray tests were setup and done for varying x-ray beam scanning at angles of 0° to 15°, with the sample initially set at ~45° to measure the x-ray diffraction off of the surface, and with a 10 second exposure time. Each area, processed and unprocessed, was scanned using these parameters. The x-ray device used is the Oxford Diffraction Xcalibur 3 x-ray diffractometer (XRD). This is a fully-enclosed single crystal XRD system. It has a Mo/Cu x-ray source with a Sapphire3 CCD detector. The instrument is

computer-controlled with CrysAlis<sup>TM</sup> software for data analysis. Samples can be cooled to temperatures between 90 and 300 K with the Cryojet nitrogen jet cold unit.

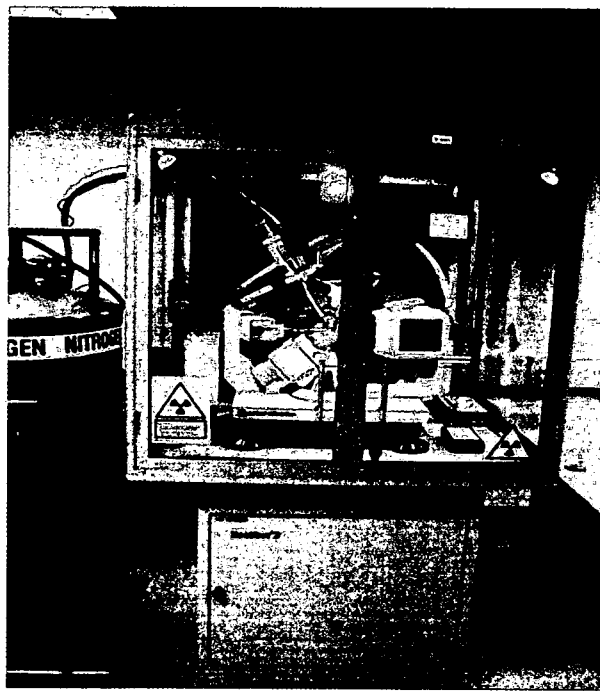
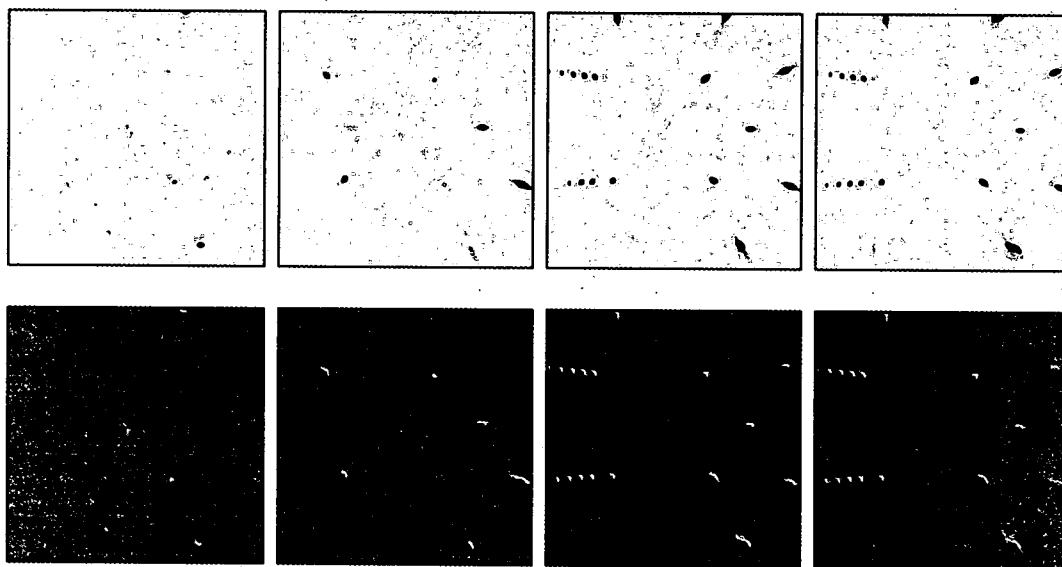
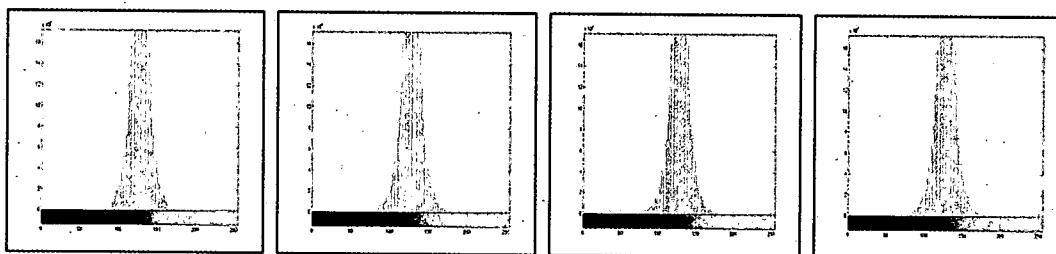


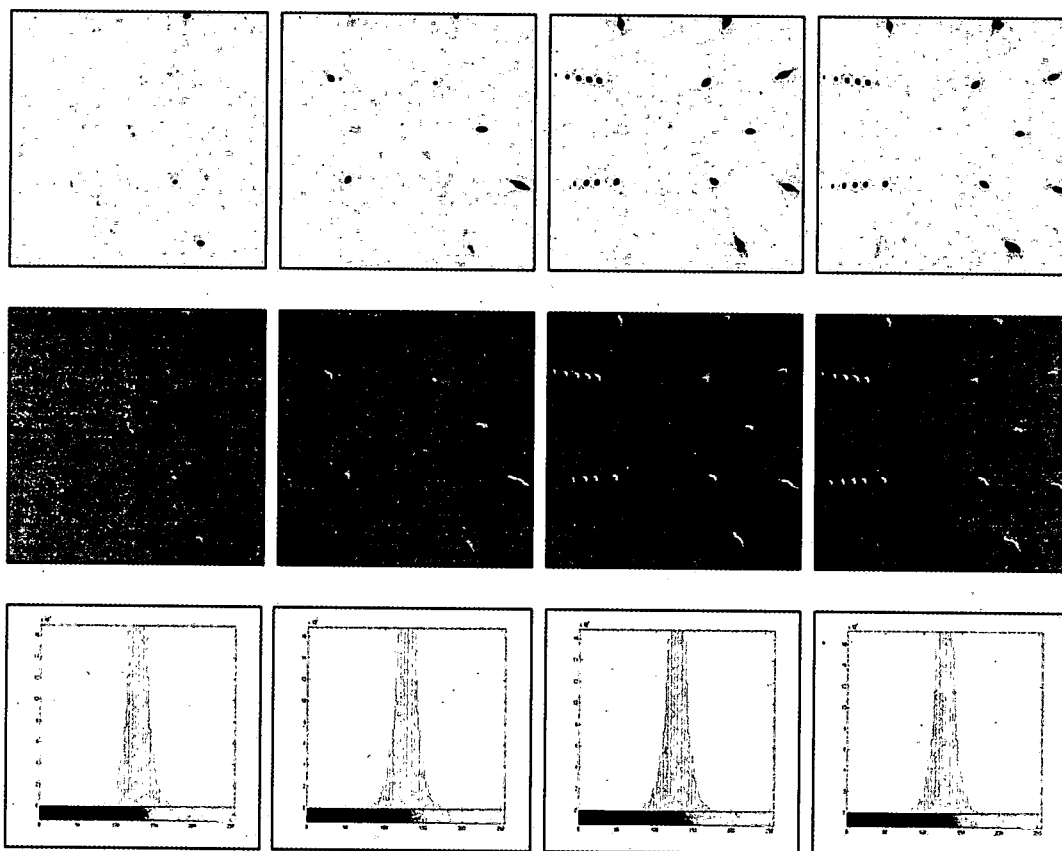
Figure 5.7: UD Oxford Diffraction Xcalibur 3 x-ray diffractometer (XRD), or x-ray crystallography.

Each area on the 6H-SiC SI sample was tested was carefully aligned to the x-ray gun using the system CCD imager.



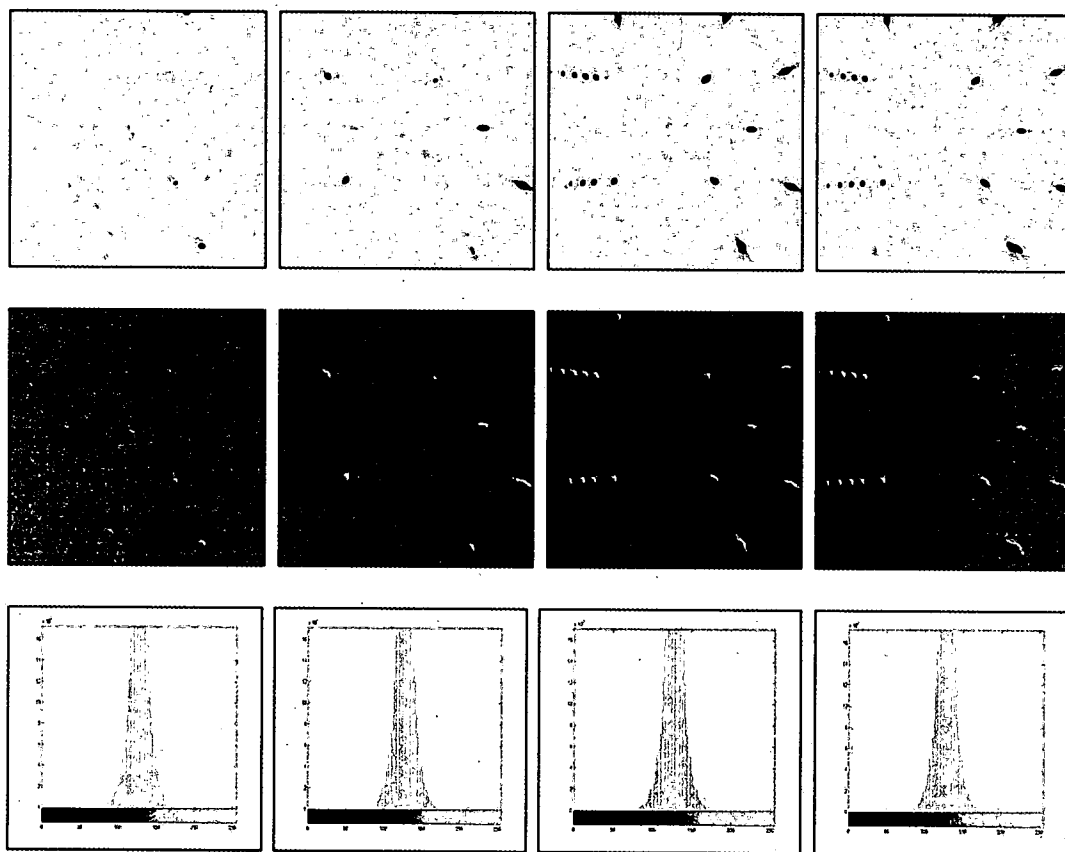


**Figure 5.8: Unprocessed SiC: in order from left to right – 0°, 5°, 10°, and 15° scans. Top is the raw images, middle is emboss-processed raw images, and bottom are histograms of the emboss images.**

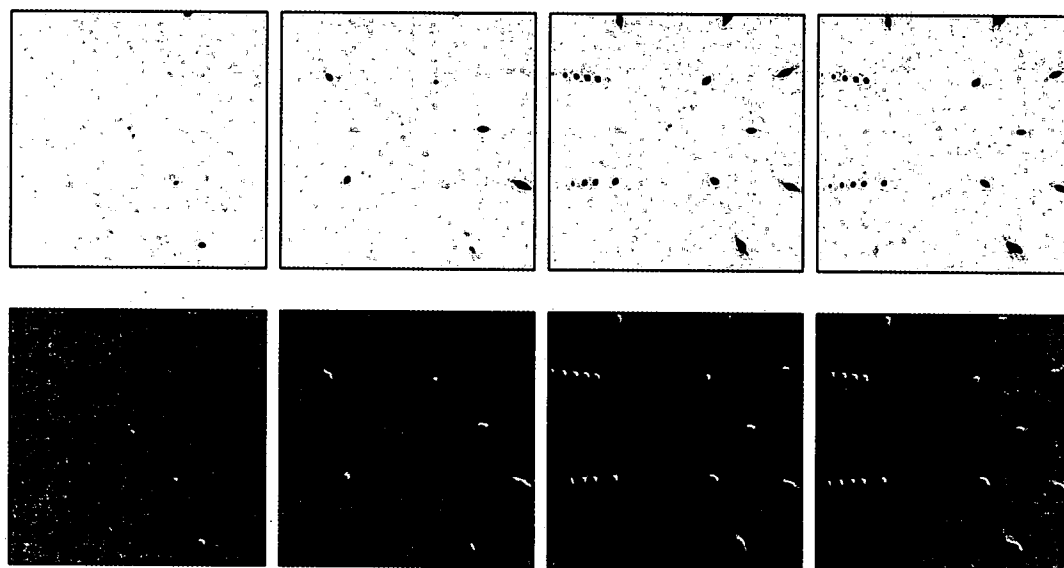


**Figure 5.9: Processed SiC for  $E_1 = 40\mu\text{J}$  area: in order from left to right – 0°, 5°, 10°, and 15° scans. Top is the raw images, middle is emboss-processed raw images, and bottom are histograms of the emboss images.**





**Figure 5.10: Processed SiC for  $E_2 = 20\mu\text{J}$  area: in order from left to right –  $0^\circ$ ,  $5^\circ$ ,  $10^\circ$ , and  $15^\circ$  scans. Top is the raw images, middle is emboss-processed raw images, and bottom are histograms of the emboss images.**



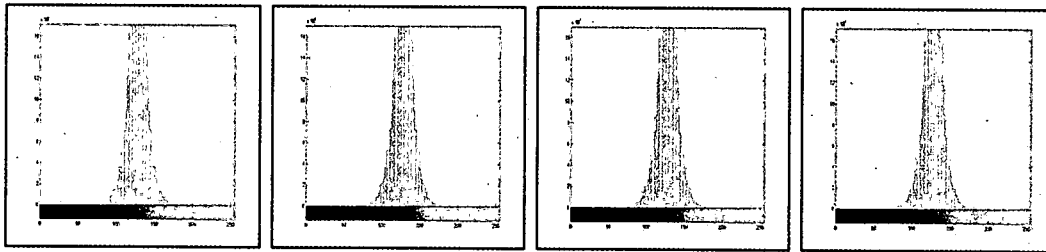


**Figure 5.11: Processed SiC for  $E_3 = 10\mu\text{J}$  area: in order from left to right –  $0^\circ$ ,  $5^\circ$ ,  $10^\circ$ , and  $15^\circ$  scans. Top is the raw images, middle is emboss-processed raw images, and bottom are histograms of the emboss images.**

Figure 5.8, Figure 5.9, Figure 5.10, and Figure 5.11 all show exactly the same result from the unprocessed to processed areas. The four angles are actually scanned, for example, the  $15^\circ$  angle is a scan from  $0^\circ$  to  $15^\circ$ , and so on. Even after the raw images have been image processed with emboss. The emboss images show the crystal diffraction patterns well, and there appears to be no distinctive differences. As with the Raman measurements, the most likely indication of damage would be in a slight peak broadening and peak shift. Such features were not resolvable with this setup.

These findings suggest one of the following:

1. The SiC subsurface processed region has not been altered by the femtosecond radiation in a way of new bond structures or with any impurities introduced. The processed regions remain SiC crystalline.
2. The x-ray beam was “seeing” the bulk SiC and the processed areas’ modulation depths are not large enough volume to be resolved, but since the x-ray beam was incident onto the processed areas at a  $45^\circ$  angle it is unlikely that the beam is only interacting with the bulk SiC substrate.

### 5.3 Atomic Force Microscopy (AFM)

The basic idea of an AFM is that the local attractive or repulsive force between the tip and the sample is converted into a bending, or deflection, of the cantilever. The cantilever will deflect towards or away from the surface as it is scanned across the “reading” the roughness of the surface<sup>35</sup>.

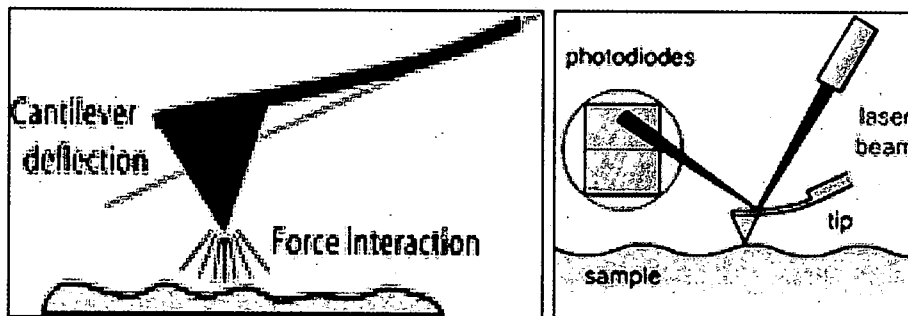
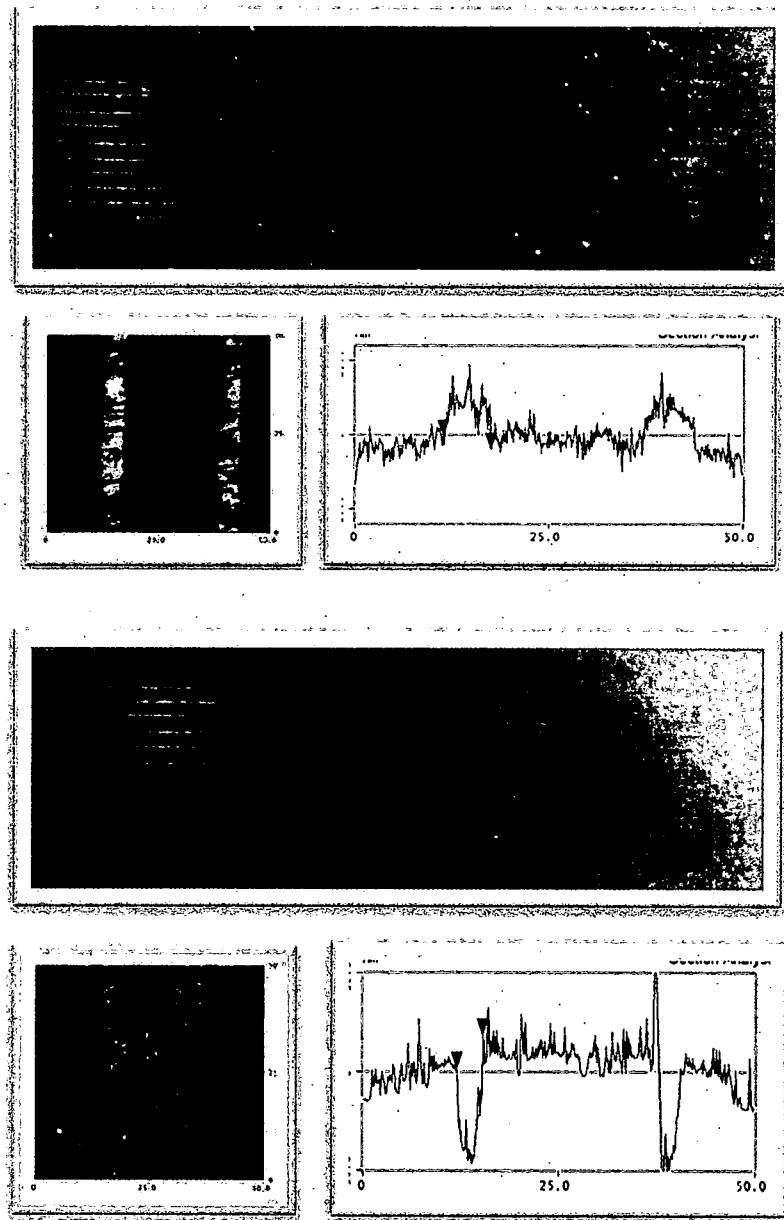


Figure 5.12: AFM illustrations from JPK Instruments.<sup>35</sup>

The pointed tip is brought into contact with the sample and moved across the surface. The cantilever deflects as it travels across the landscape (topography). The cantilever deflection is usually detected by a laser beam, which is focused on the flat top of the cantilever. The movements of the reflected light are monitored through the current in different parts of a photodiode. This information about the tip movement provides three-dimensional images of the sample.<sup>35</sup>

The AFM used at WPAFB is a Veeco Dimension 3100 with a Nanoscope 3a controller in tapping mode to evaluate the topography of line distributions fabricated just above the threshold. The purpose of the AFM tests was to study the modified regions of the SI and conducting SiC grating structures.

The results from this unit are presented, and shown in Figure 5.13. Figure 5.13 below was shown previously and is shown again here to help illustrate how the morphology of these features gives evidence to the physics of the index modifications. These images have been previously shown, but are present here for convenience.



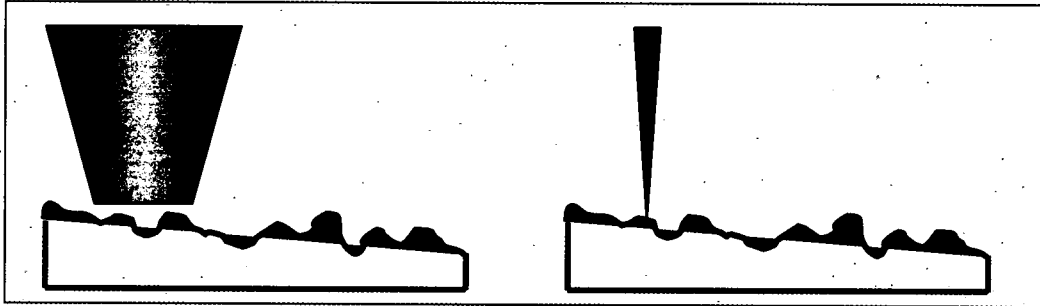
**Figure 5.13:** On the top shows the microscope DIC image of the semi-insulating SiC processed lines and AFM results of a 5.5 $\mu\text{m}$  wide and a 10nm raise surface modification on SI SiC material. On the bottom shows the DIC microscope image of the conducting SiC sample and AFM results of a 3.3 $\mu\text{m}$  wide and a 30nm trench surface modification. This figure is also shown previously.

Figure 5.13 shows how the semi-insulating SiC sample forms lines protruding bulges that are raised by  $\sim 10\text{nm}$  and have a width of  $\sim 5.5\mu\text{m}$ , while the conducting SiC sample forms line trenches that are  $\sim 30\text{nm}$  deep and have a width of  $\sim 3.3\mu\text{m}$ . The actual grating processed lines are theoretically  $3\mu\text{m}$  wide so the AFM shows that the conducting SiC is very close to  $3\mu\text{m}$ , but since the SI SiC protrudes into a "hill" causes the predicted width to become larger, which may be due to a local subsurface restructuring has occurred or some other electronic trapping process<sup>36</sup> has forced the material to rise in the processed areas. Whereas, the conducting SiC sample forms trenches that may be due to surface structural damage caused by thermal breakdown of the molecular lattice to the inability for the crystal to dissipate heat, and/or oxidation and chemical reactions on the surface that give a different compound. Shown here is a morphology difference in the femtosecond laser processing of SiC between semi-insulating and conducting types. However, modulation depth was not determined using AFM, but TEM gave this finding.

#### **5.4 Near Field Scanning Optical Microscopy (NSOM)**

Near Field Scanning Optical Microscopy (NSOM) is the use of a light source and/or a detector that is itself nanometer in scale.<sup>37</sup> NSOM uses near-field diffraction where light is collected through the tiny tip of a fiber optic, and the tip's entrance aperture can be on the order of tens of nanometers. When the tip is brought to nanometers away from a sample under test, the resolution is not limited by far-field diffraction (as in a typical optical system), but by the size of the tip aperture. An image can be built by a raster scan of the tip over the surface to create an image. In a typical far-field optical system the smallest resolvable image is inversely proportional to the wavelength used to image the

specimen. In a near-field system the smallest resolvable image is inversely proportional to the physical limiting aperture size, which is the fiber optic tip. Thus, the smaller the tip size the smaller the feature that can be resolved.



**Figure 5.14:** (Left) is an example of a far-field imaging system, (Right) is an example of a near-field imaging system.

Near Field Scanning Optical Microscopy (NSOM) was completed on semi-insulating SiC in order to determine if an index change had occurred in the processed area. This test was carried out on a subsurface SiC grating to ensure that the index change is due to phase modulations and not surface structures. As shown above with the AFM measurements, when the gratings are written subsurface, no modification of the entrance face of the sample is present. The NSOM instrument was used in the following fashion to record the phase-only index modifications.

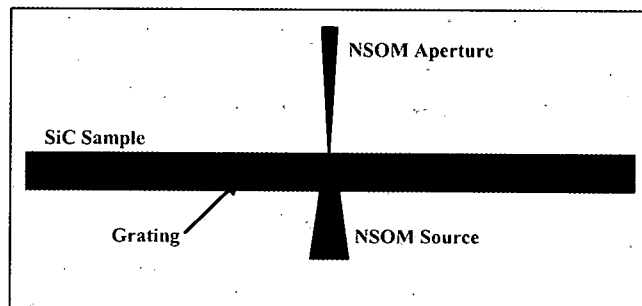


**Figure 5.15:** SiC grating NSOM measurement setup.

Figure 5.15 illustrates the NSOM setup used to measure the subsurface grating index modifications, while Figure 5.16 shows the NSOM results.

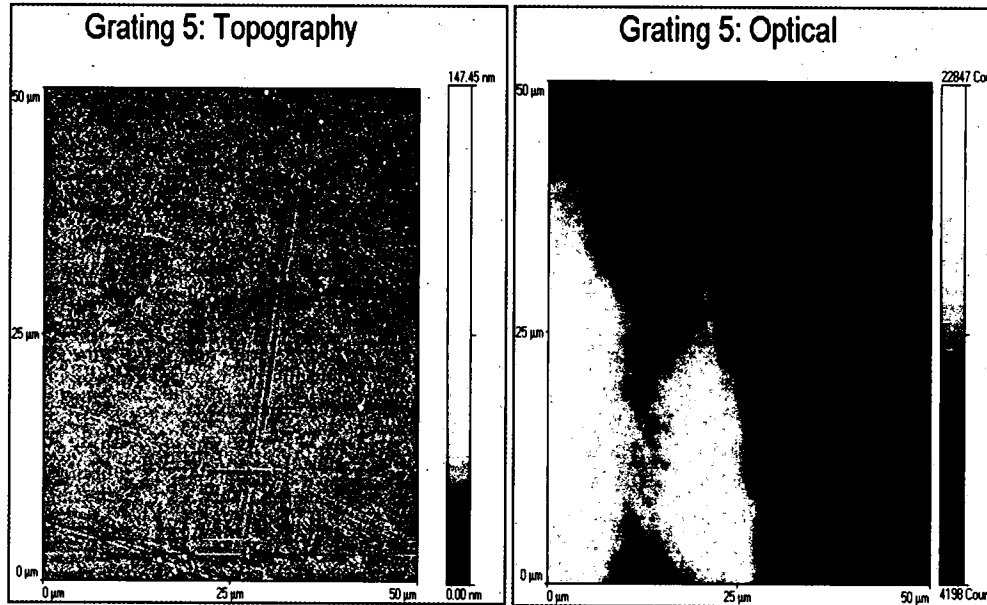


Figure 5.16 (Left) is topography of the semi-insulating SiC sample, (Right) is the optical output revealing an index change.

The NSOM optical image is generated from a collimated light source illuminating the SiC sample ( $\sim 250\mu\text{m}$  thick) from the bottom while a fiber receiver collects the output from the top surface only, which is only  $\sim 100\text{nm}$  from the surface. The topography image in Figure 5.16 (Left) shows an absence of any surface alterations due to processing, but the modifications do exist below the surface. Figure 5.16 (Right) demonstrates that the collimated input beam (from the bottom of the sample) is coming to a focus at the fiber receiver after propagating through the subsurface SiC grating line modifications. The grating lines act as micro-lenses consisting of convex radii and an index change in order to cause the collimated light to focus. The lighter areas in the optical image show where the light is coming to a focus at the fiber receiver, thus confirming the semi-insulating SiC sample contain a  $\Delta n$  only in the processed areas. The

fact that this particular grating is subsurface also suggests that the modulation is phase and not amplitude.

## 5.5 Transmission Electron Microscopy (TEM)

Transmission Electron Microscopy (TEM) is technique whereby a beam of electrons is transmitted through a thin sample, interacting with the sample as it passes through it.<sup>38</sup>

An image is formed from the electrons transmitted through the sample, which is then magnified and focused by an optical lens and forms an image onto a sensor. A crystalline material interacts with the electron beam mostly by diffraction rather than absorption, although the intensity of the transmitted beam is still affected by the volume and density of the material through which it passes. The intensity of the diffraction depends on the orientation of the planes of atoms in a crystal relative to the electron beam; at certain angles the electron beam is diffracted strongly from the axis of the incoming beam, while at other angles the beam is largely transmitted.<sup>38</sup>

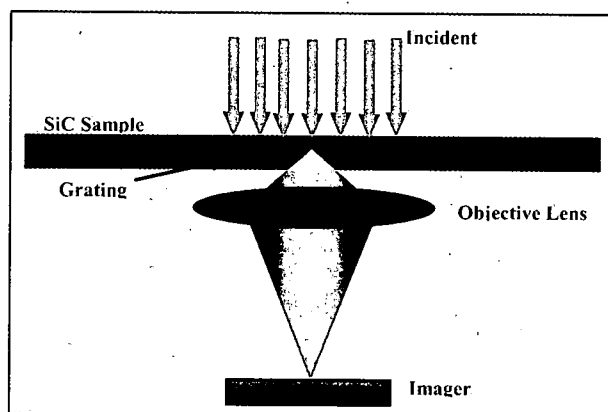


**Figure 5.17: Fixed beam TEM setup – drawing is not to scale.**



The TEM setup above is not to scale. First the SiC processed area (grating) had to have focused ion beam (FIB) milling procedure performed on the area of interest. Two gratings were analyzed, one was subsurface (shown below in Figure 5.18) and the second grating is just below the surface with a protruding “hill” as shown in the AFM section of this Chapter. Figure 5.18 shows the subsurface grating (embedded in the middle of the substrate), which is presented in that figure as an example of FIB. These two gratings have fairly different TEM profiles, which is attributed to where they reside in relationship to the surface.



**Figure 5.18: Subsurface semi-insulating SiC with FIB preparation: (Left) 10x microscope image of the subsurface grating before FIB, (Right) 20x microscope image of the FIB processed area.**

Once the sample area was milled out, TEM was performed and those results are shown next. First the surface grating will be displayed showing interesting artifacts that will be theorized as to what is causing them.

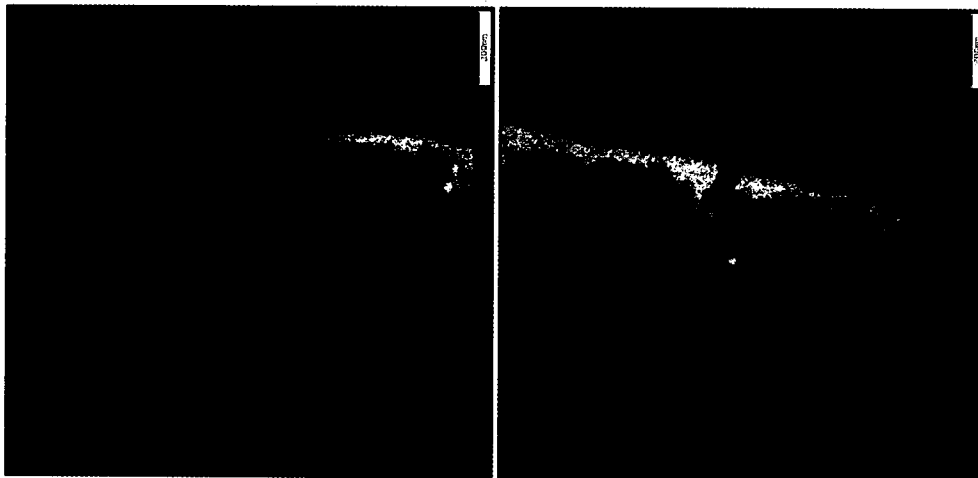
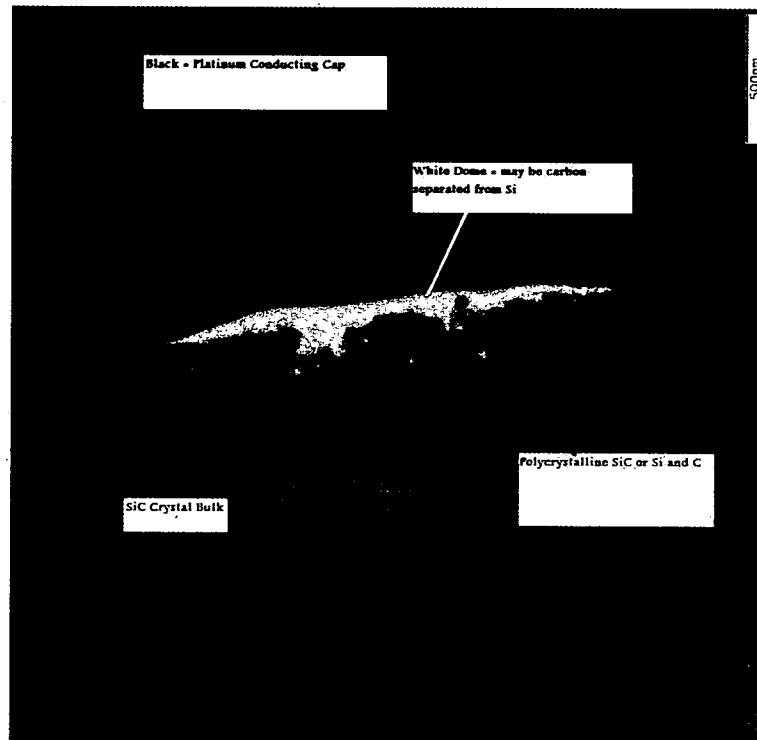


**Figure 5.19:** (Top) is the image of the surface grating TEM that is labeled to identify the key features of the TEM specimen. (Bottom Left & Right) are zoomed images of the labeled top image to give a better image of the processed area.

Figure 5.19 shows a “dome” of lighter material with appears to be polycrystalline in the processed areas. The polycrystalline region is likely due to super cooling of the crystal lattice causing microscopic crystalline regions that have random polarizations of the

birefringent substrate. The black area on top is the conducting cap for the TEM measurement/setup. The bottom gray area is the unprocessed semi-insulating SiC bulk. The polycrystalline is most likely a combination of Si, C, and/or SiC. The "dome" may be a separation of carbon for silicon and the carbon has risen above creating a protrusion as shown in the AFM results. The "dome" is perceived to be C since Si has a larger atomic number and larger atomic numbers appear darker in the resulting imagery. The curved lines below the polycrystalline and above the SiC bulk is known to be caused by the electron beam diffraction affects from the TEM, which are of no consequence.

Next, TEM was performed on a totally subsurface,  $\sim 0.5\mu\text{m}$ , processed gratings micromachined within the same semi-insulating SiC specimen. These results differ from that of the surface grating in that they do not have a separation of Si and C, or at least very little as is shown below. Rather, it will be shown that the TEM results in Figure 5.20 support the lattice deformation theory as will be described momentarily. Simply, subsurface processed regions are theorized here to be lattice deformations, while the surface processed regions are theorized to be broken bonds causing silicon and carbon to separate creating a localized amorphous region trapped within the bulk organized crystalline lattice.

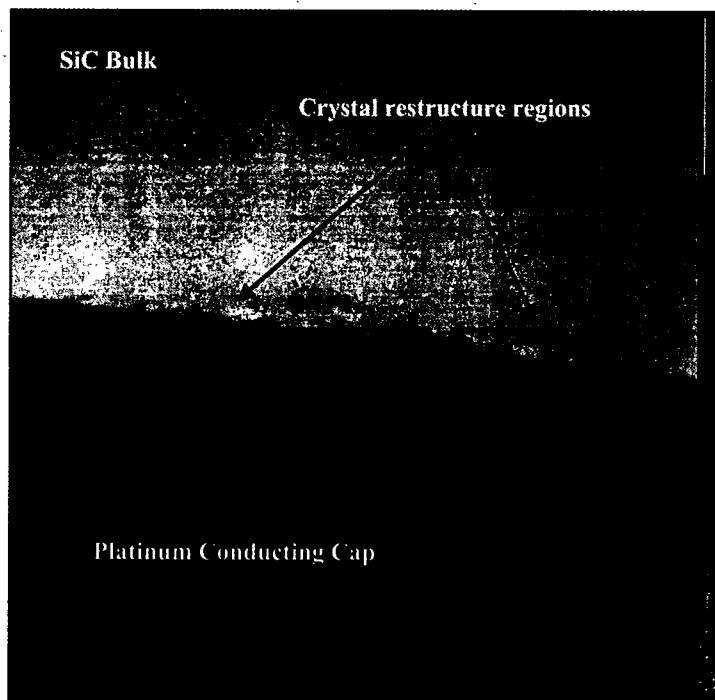


**Figure 5.20: TEM of subsurface SiC grating line.**

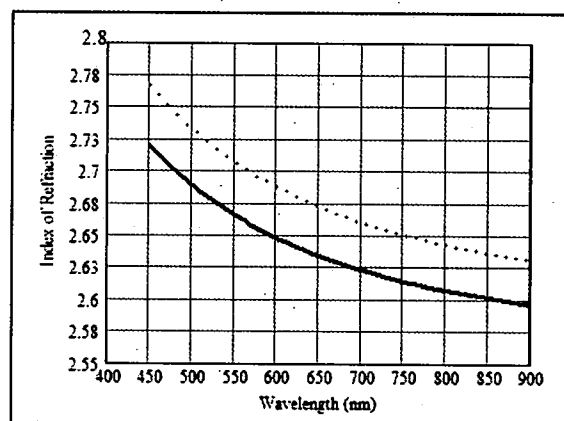
As observed in this TEM is that the SiC bulk area is nearly the same color/density as the processed area which tells us that the Si did not separate from the C and form polycrystalline and/or a “dome”. However, observed is a slight discoloration where there may be some Si and C separation, but not nearly as much as the surface features. This tells us that the air (room temperature non-purged air) is playing a role in the formation of the new index or  $\Delta n$  formation. It would be interesting, in a future study, to purge the processed area with nitrogen to understand the formation of the “dome” for surface grating features. The only reason why this was not done is because it was unknown that the “dome” or silicon-carbon separation even existed until the TEM measurement was done, and those results took a good deal of time to acquire. In addition to processing new

surface features on SI SiC in the presence of a nitrogen purge, likewise it would also be interesting to run the same test with subsurface features for completeness.

One imaging technique that may be useful to further analyze this sample is SIMS.

Secondary Ion Mass Spectrometry (SIMS), which is used for sub-monolayer elemental analysis, would be used to investigate if the "dome" is truly carbon or some other impurity. Regrettably, this device is has not been available for our employment, but it is our hope to use this technique in the near future. With that being said, all the theories related to the TEM data and what is the cause of these features will be discussed in the following bullets. It appears that the  $\Delta n$  may be attributed to one of the following mechanisms:

1. Polycrystalline origin may be from the fast laser pulse that caused the SiC to melt then quickly quench with different crystal orientations. Hence, the SiC material remains intact, but only with various crystal orientations. Where the  $\Delta n$  may be comprised of an average of  $n_e$  and  $n_o$  (extraordinary and ordinary refraction indices). In contrast, the polycrystalline may not cause an effective average  $\Delta n$ , rather, the crystals may be too small for the optical wavelengths to "see" an index change. The figures below help to describe this theory.



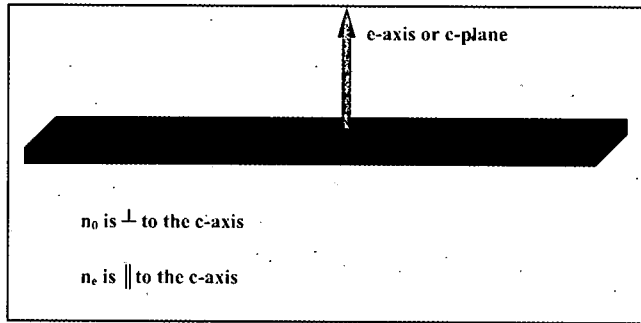


**Figure 5.21: (Top) is the extra-ordinary and ordinary SiC crystal refraction indices plot as a function of wavelength, (Bottom) is a plot of the SiC crystal indices orientations.**

2. Separation of Si and C, where Si is vaporized leaving carbon in a

homogeneous state where it may form a “dome” on the surface.

Polycrystalline regions are also formed leaving additional index modifications that lie under the “dome”. In this case, the carbon has a different index than silicon. As mentioned, the larger atomic number elements, Si, will be darker in the TEM imagery, and the carbon, with a smaller atomic number, will appear lighter. Being that the “dome” is very uniform in color, from the TEM images above, theorizes that the “dome” is carbon only and not a mixture of C and Si. In addition, even if the “dome” is NOT carbon it remains that it is definitely not SiC and thus must have a different linear and nonlinear index of refraction. The polycrystalline area could be contributing to the  $\Delta n$  along with the “dome” layer (weather it is C or some other material). The SiC crystallites have varying orientations, which affect the index since SiC is birefringent, thus the  $\Delta n$  may be written as the average of  $n_e$ ,  $n_o$ , and  $n_{dome}$ .

$$\Delta n \approx \left( \frac{n_e + n_o}{2} \right) \pm \left[ \left( \frac{n_e + n_o}{2} \right) - n_{dome} \right]$$

**Equation 5.1**

The above equation for  $\Delta n$  is only an approximation and this expression is not conclusive.

3. The third possibility is that scattering and or impurities may be causing the index change. Scattering alone, however, would not be an index change, but would make the processed grating lines visible under the optical microscope. In contrast, the NSOM, Nomarski DIC, Zscan, and DE results all reveal a phase-only index modification so scattering is unlikely. It is plausible, though, that there may be some scattering, but we do not believe that this is the sole cause.
4. The most probable cause for the subsurface processed features is lattice deformations without additive impurities. These deformations cause a location change in the dipole moments, which cause index modifications.

## **5.6 Index Modification Degradation over Time**

Grating structures were micromachined in semi-insulating and conducting 6H-SiC and soda lime glass (SLG), as well as spherical lens or circular processed areas in fused silica (FS) for DT experiments. These processed features were created in these samples over a 2-3 year span, and in that time most of the samples (especially the samples with gratings) were re-investigated under the optical microscope numerous times for various reasons. It was during those periodic inspections that it was observed that the subsurface structures prepared in amorphous substrates (SLG and FS) have completely vanished. However, the femtosecond laser processed regions in all of the SiC crystalline substrates are

completely intact. This effect of the processed features in amorphous substrates vanishing takes, in general, approximately 1-2 years for them to completely fade away.

Initially, at approximately 6-8 months after processing gratings into SLG, it was difficult to detect the structures under the optical microscope even with Nomarski DIC employed. It was ignored at that point because the gratings were still detectable and the fact that the diffraction efficiencies (DE) were still measurable. Subjectively the efficiency,  $\eta$ , was decreased; although it was unknown by exactly how much, but the  $\eta$  of the first order was at least down by half. Unfortunately, the  $\eta$  was not recorded versus grating spacing as done initially, but it is safely assumed that each grating spacing  $\eta$  had dropped by  $\sim 1/2$  as depicted in Figure 5.22.

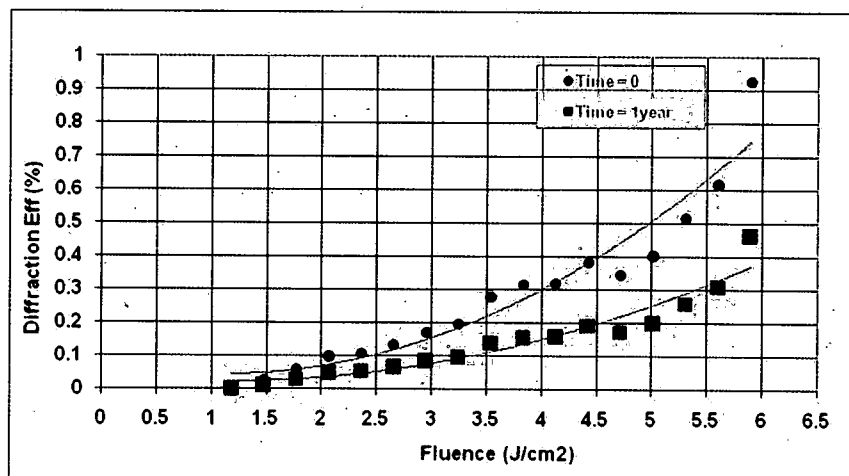


**Figure 5.22: DE versus fluence for two times: Time 0 is when the DE was measured directly after writing the gratings, and Time 1 year is an approximate drop in  $\eta$  by 2.**

In Figure 5.22 Time = 1 year is only an approximate – it was only measured for 3 or 4 of the high  $\eta$  data points (gratings at different fluence levels), which was then assumed that the rest of the  $\eta$  decreased by  $\sim 2$  as well. This affect is best described visually in the following figure.



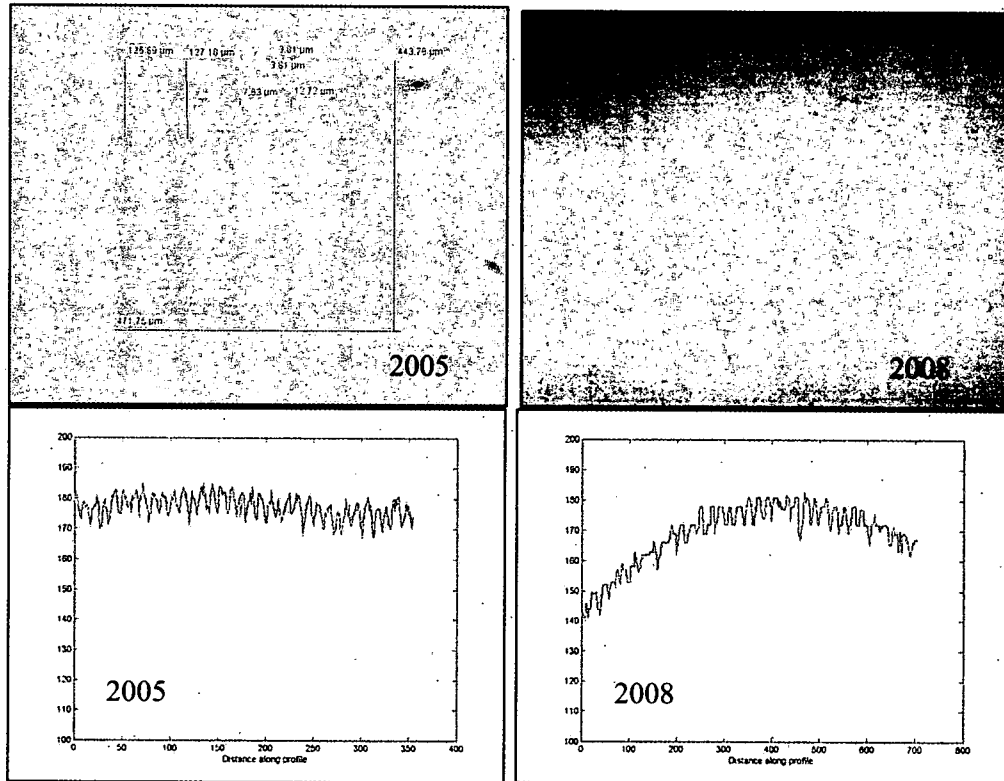


**Figure 5.23: (Top) is an optical microscope image of a surface grating micromachined in SLG in 2005 and the same grating re-imaged in 2008, (Bottom) are the lineout results for each.**

Figure 5.23 shows how a subsurface grating micromachined in SLG has degraded over time. By degrade we mean that the femtosecond processing has almost completely reversed itself. The only reason why any grating lines exist is because there happened to be some surface damage, which is the only way the amorphous processed features will persist. This figure also shows the lineout images on the SLG surface gratings: (Left) 2005 lineout, (Right) 2008 lineout.

To illustrate how a subsurface SLG grating degrades the following figure compares two subsurface gratings.

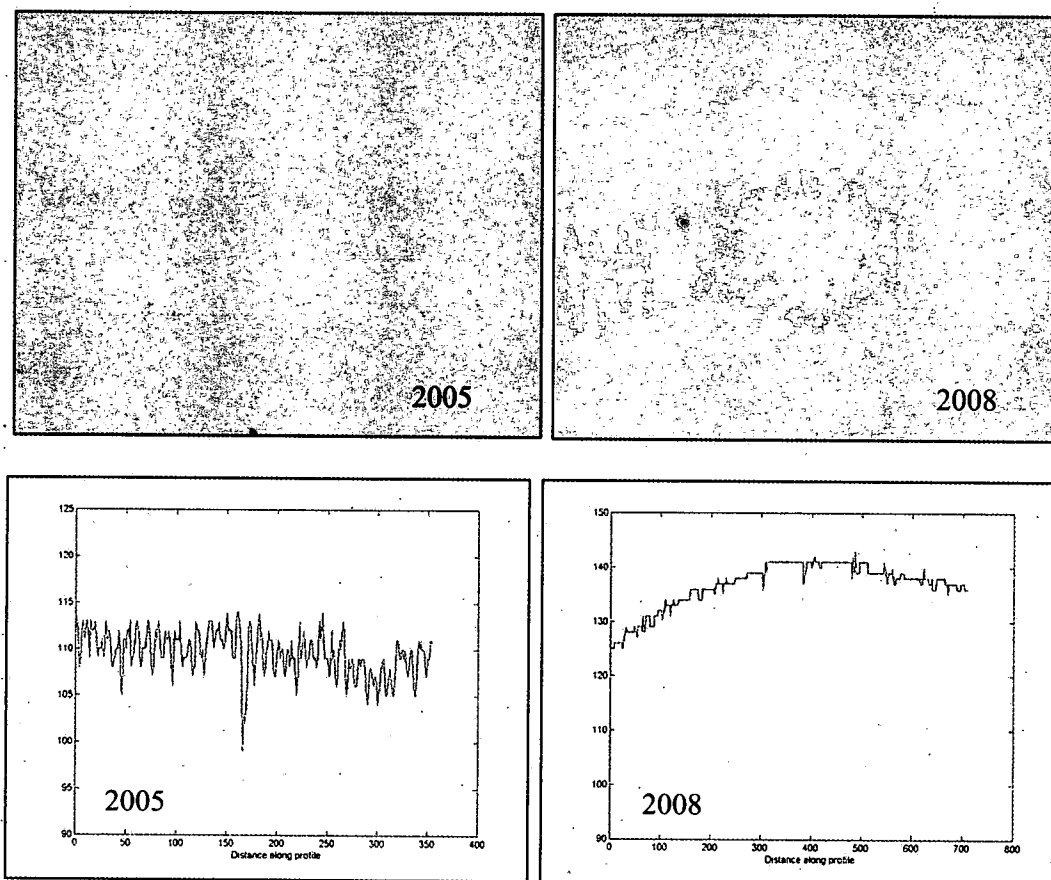


**Figure 5.24: Subsurface SLG gratings: (Top) are the optical microscope images, (Bottom) are the lineout images.**

Thus, as shown from Figure 5.23 and Figure 5.24 the amorphous substrates are “healing” over time to the point where the subsurface features are not even visible even using Nomarski DIC (not shown above). Whereas, the surface femtosecond processed features do remain only from oxidation that has occurred on the surface immediately after processing. Unlike the amorphous substrates, SiC crystalline materials were also processed and their features (surface and subsurface alike) remain without any indication of “healing”, even after being annealed.

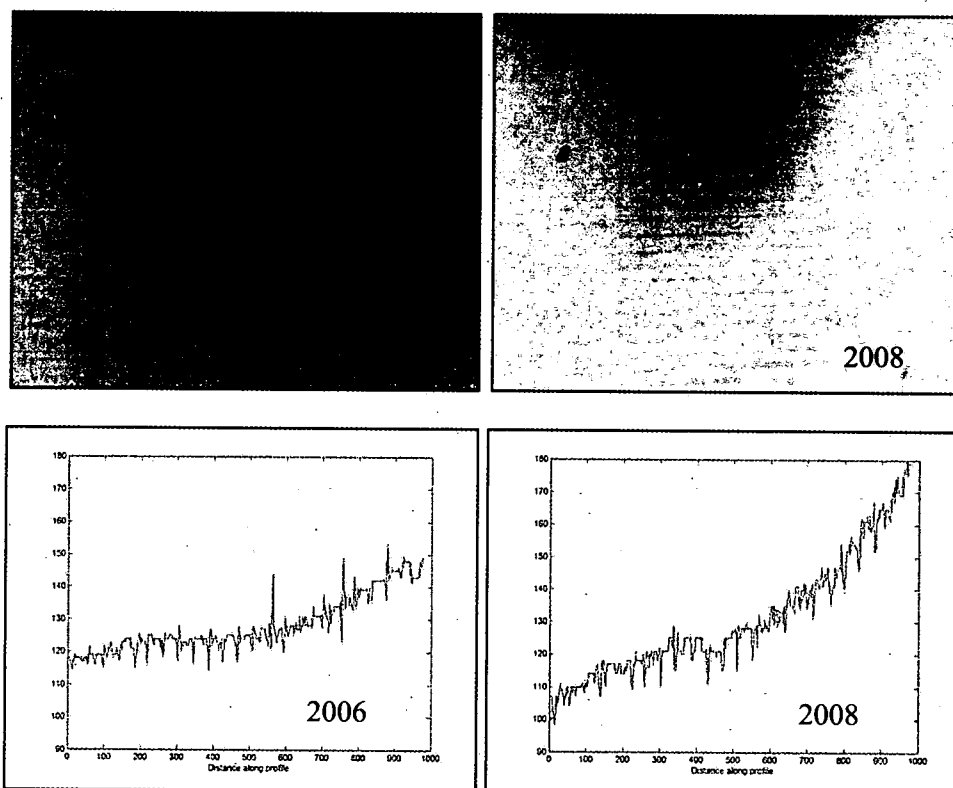


**Figure 5.25: Subsurface SiC gratings: (Top) are the optical microscope images, (Bottom) are the lineout images.**

As observed from Figure 5.25, the SiC gratings have not degraded (or “healed”) to any significant amount. In fact, the SiC 2008 SiC grating image was also annealed to 399°C. Thus, neither time nor heat will alter the SiC subsurface grating structures, which suggests their crystal structure was indeed altered and the lattice is different. This means that the lattice dipoles are at different locations and this would cause an index change given that when light interacts with those new dipole moments a new index of refraction is the result.

The theory behind why the amorphous materials “heal” over time and the crystalline materials do not is due to a multiphoton process in which two or more photons are absorbed by the material at the atomic level and some of the outer bound electrons get

trapped from the fast femtosecond pulse causing fast electron cooling. The cooled or trapped electrons then create hole-pairs, which after time or annealing could re-combine with holes in close proximity and essentially "heal" the modified femtosecond processed area. In crystalline structures, the femtosecond pulse also induces a multiphoton absorption process by which the electrons are freed, but because the substrate is highly organized the result may result in broken atomic bonds for surface features and deformed atomic bonds for subsurface features. These deformed bonds result in a new structure with the atomic dipoles in different locations from the original crystalline lattice structure. Any photon incident on these new dipoles will interact differently than the originally crystal dipole mapping. This is not necessarily any new elements or impurities that are introduced, but possible new or a re-organized compound structure due to a deformed crystal lattice. This is supported by the fact that annealing the SiC crystalline processed samples did not "heal" or change the resulting femtosecond micromachined grating lines at all since the only way the crystal will change is if the melting point of the crystal is reached.

## **5.7 Summary of Results**

Here, a summary of all of the above experiments will be given to consolidate each conducted experiment to provide a better understanding of what the possible causes of femtosecond index modifications in crystalline and anamorphic materials. At the very least, the data provided will add to the science of index of refraction changes in bulk transparent materials. Below is a list of the key findings.

1. Optical Microscopy:
  - a. Nomarski DIC images provide evidence that the subsurface features are resulting from phase changes within the bulk transparent substrate that are attributed to index of refraction changes.
2. Raman Spectroscopy:
  - a. No evidence of new elements or compounds was found in the processed SiC.
  - b. Some peaks have been broadened and shifted slightly, which is probably caused from crystal lattice deformation.
3. X-ray Crystallography:
  - a. No evidence of new elements or compounds was found in the processed SiC.
4. Atomic Force Microscopy:
  - a. Surface SI SiC grating features resulted in protruding rises caused by the creation of a carbon-dome that should have a different index of refraction from that of the bulk due to possible broken Si-C bonds creating localized amorphous Si and/or C within the crystalline bulk.
  - b. Subsurface SI SiC grating features is the result of lattice deformation. Thus the primary cause for index change is likely crystal lattice dipole changes.
  - c. Surface conducting SiC grating features likely are attributed to thermal breakdown of the SiC molecular lattice.
5. Near Scanning Optical Microscopy:
  - a. The subsurface SI SiC grating features have been proven to be below the surface and a phase-only index change.
6. Diffraction Efficiency Experiments:
  - a. For the subsurface gratings a phase only diffraction orders were created owing to  $\eta \sim 0.5\%$ .
  - b. The subsurface gratings also follow VPH theory as a function of diffraction angle and magnitude of  $\Delta n = 0.032$ .
  - c. For the surface gratings, phase and amplitude diffraction is the result.
7. Zscan Experiments:
  - a. Successful nonlinear  $\beta$  and  $n_2$  measurements were made, which support a phase-induced index modification.
  - b. Confirmation of the  $\Delta n$  measurement was made from the  $n_2$  result.
8. Transverse Electron Microscopy:
  - a. Support of the AFM results:

- i. Surface SI SiC grating features resulted in protruding rises caused by the creation of a carbon-dome that should have a different index of refraction from that of the bulk.
    - ii. Subsurface SI SiC grating features resulted lattice deformation, thus the primary cause for index change is likely due to crystal lattice dipole changes.
  - b. The TEM results also provided the true grating modulation depth of 0.5 $\mu$ m.
9. EDS:
- a. No chemical changes occurred, which supports the Raman, X-ray, and TEM results.
10. Time Study:
- a. These unexpected observations proved to be valuable in the fact that they provide support of the TEM, X-ray, Raman, and EDS measurements – no chemical alterations in the SiC, but rather a lattice deformation.
  - b. The amorphous substrate time study supports the idea that the electron-hole pairs are slowly recombining causing the index modified subsurface structures to completely disappear.

In conclusion, index changes exist in the amorphous and crystalline materials studied. In the amorphous substrates the index modifications are likely due to electron trapping created from high intensity/fast pulses causing multiphoton absorption/ionization, which is the mechanism for creating free electrons then quickly cool those electrons to form electron-hole pairs in the substrate. This fast electron cooling caused electron-hole pairs that eventually re-combine after time and/or annealing since the substrate is unorganized.

The crystalline subsurface index changes are likely due to the crystal lattice bond deformation, again caused by the short-pulse multiphoton ionization process, which redistributes the electron dipoles to new locations from the deformed lattice, which causes the incident photons to interact with these new dipoles resulting in a new index of refraction. There is no evidence of new elements, compounds, or impurities within the

processed regions of the crystal. Surface crystalline index modifications are most probably due to localized broken bonds between Si and C causing a "carbon-dome" and/or randomly oriented polycrystalline resulting in average  $n_e$  and  $n_o$  indices.

## CHAPTER 6

### SiC Grating Temperature Sensor

In this chapter the SiC temperature sensor design, testing, and characterization is discussed. Also shown here is the theoretical model and measurement of the coefficient of linear and nonlinear thermal expansion. A new technique for measuring the linear and nonlinear coefficient of expansion is presented.

#### 6.1 Introduction

An optical temperature sensor was developed using a femtosecond micro-machined diffraction grating inside transparent bulk 6H-SiC. In addition to the temperature sensor, a measurement of the 6H-SiC thermal coefficient was made by means of the grating first order diffracted beam. A HeNe laser beam was used with the SiC grating to produce a first-order diffracted beam where the change in deflection height was measured as a function of temperature. The grating was micro-machined with a  $20\mu\text{m}$  spacing and has dimensions of approximately  $500\mu\text{m} \times 500\mu\text{m}$  (l x w) and is roughly  $0.5\mu\text{m}$  deep into the 6H-SiC bulk. A maximum temperature of  $399^\circ\text{C}$  was measured, which gives a  $\Delta T$  of  $372.3^\circ\text{C}$ . The sensitivity of the technique is  $\Delta T=5^\circ\text{C}$ . A maximum deflection angle of  $1.81^\circ$  was measured in the 1st order diffracted beam. The trend of the deflection with increasing temperature is a nonlinear polynomial of the 2nd order. This optical SiC thermal sensor has many high temperature electronic applications, such as, aircraft turbine and gas tank monitoring for commercial and military applications.



Diffraction gratings have a variety of applications, and are constructed by a number of techniques. The grating in this dissertation was fabricated using a femtosecond laser and an anamorphic lens,<sup>39</sup> and then this grating was used in a new method of measuring temperature and the thermal coefficient of a sample. Bulk transparent 6H-SiC was selected to have a 500 $\mu\text{m}$  length x 500 $\mu\text{m}$  width x 0.5 $\mu\text{m}$  deep grating with 20 $\mu\text{m}$  spacing micro-machined using the anamorphic lens technique.

SiC is an attractive alternative material for a variety of semiconductor devices where silicon (Si) lacks the environmental resistance that carbon furnishes when combined to Si.<sup>40</sup> These areas where SiC devices can be used include high-power high-voltage switching applications, high temperature electronics, and avionics where it is desired to keep sensitive Si-based electronics and temperature sensors away from extreme environments onboard aircraft (such as turbines and fuel compartments).<sup>40</sup> For these reasons, it is of interest to study the use of SiC as a noncontact high temperature sensor. The SiC used for this study has the following characteristics shown in Table 2.1.

As a comparison, different types of temperature sensors were investigated as a comparison to the noncontact optical SiC sensor. Compared to other temperature sensors, the SiC temperature sensor has a few advantages. The primary advantage is the measurement of temperature transparent/nontransparent materials. It is possible, using this technique, to measure nontransparent materials if a grating is pressed into a metal surface, for example, and the diffraction pattern is measured from the reflection. Other advantages is the measurement of extremely high temperatures remotely, the ability to measure the coefficient of thermal expansion of transparent/nontransparent materials, and

the ability to measure the coefficient of linear expansion of transparent/nontransparent materials.

## 6.2 Sample Mount Design

The SiC sample under test is  $340\mu\text{m}$  thick and  $\sim 0.75''$  square, therefore, the mount was designed to hold the sample with room for expansion. The mount was milled from copper for best conductivity.

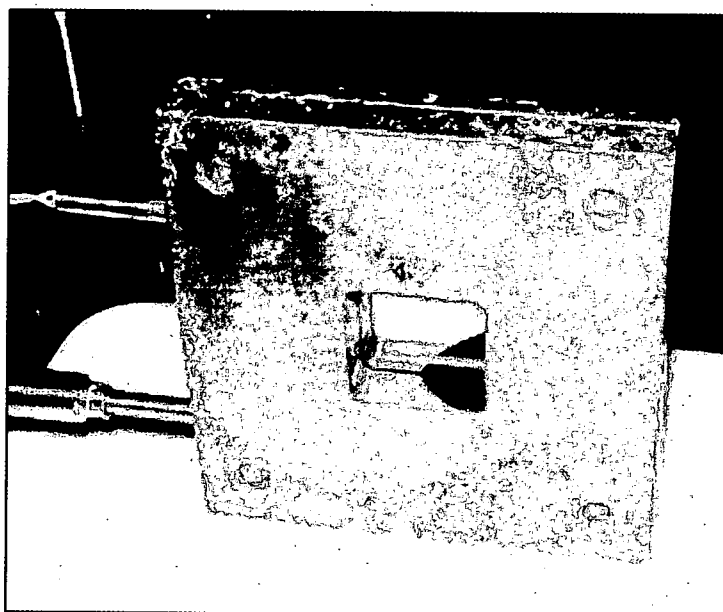
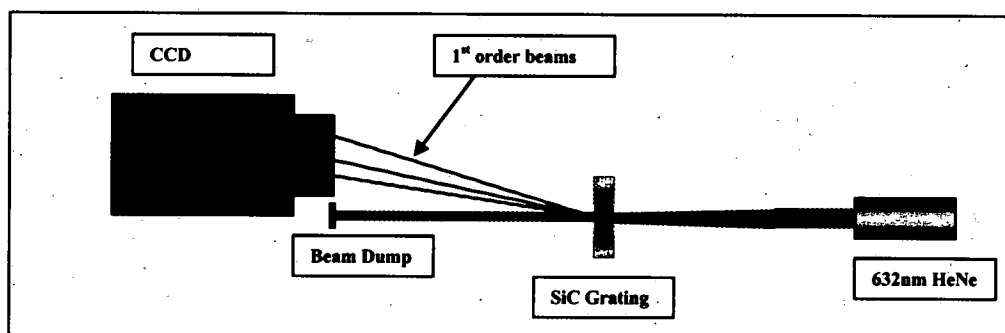


Figure 6.1: SiC sensor mount milled out of copper.

## 6.3 Experimental Setup

Below is the experimental setup for the SiC temperature sensor, which uses a 632nm HeNe source to illuminate the grating structure, embedded in the SiC surface.



**Figure 6.2: SiC temperature sensor experimental setup.**

Figure 6.2 shows the setup for the SiC temperature sensor, which consists of a 632.8nm HeNe, the SiC grating seated in a copper mount, and a CCD camera to record the change in the 1<sup>st</sup> order height ( $\Delta x$ ). The camera is a Cohu 4812 model and it utilizes Spiricon laser beam analysis software to measure the vertical centroid direction in microns. Each of the first order beams in the figure is representing different heights due to the increasing temperature (not to scale). The camera is calibrated against neutral density filters and the background lighting to a FieldMax power meter. The total power from the 0-order to the total power in the first order gives a measure of the grating efficiency; that was measured for completeness to be 0.6% ( $DE = 2P_1/P_0$  – where the 2 represents the  $\pm 1$  orders). The change in 1<sup>st</sup>-order beam height ( $\Delta x$ ) was measured and plotted as a function of temperature.

The 6H-SiC grating was mounted in a 2.25" x 2.25" copper mount with a 0.5" square hole where the sample was placed so that the HeNe beam could propagate through the grating. The copper mount had two 1/8" diameters by 2" deep holes for the J-type thermal couple and the cartridge heater. The copper mount and SiC sample together were insulated with ceramic shielding and the SiC temperature was also monitored with a K-

type thermal couple to ensure the grating was at the same temperature as the copper. The cartridge heater started at 26.7°C (about 10° above laboratory temperature) and in 50° increments was able to reach 399°C.

The temperature was measured and controlled with an Omega temperature controller CN7800 that has  $\pm 1^\circ \text{C}$  resolution and with the ceramic insulation the measurements were consistently within  $\pm 3^\circ \text{C}$  due to the temperature of the laboratory convection. Most of the error in measurement came from the Spiricon resolution, which has a spatial accuracy of  $\pm 0.5\%$  and a beam width accuracy of  $\pm 2\%$ . However, due to convection caused from the laboratory temperature, the 1<sup>st</sup> order deflected HeNe beam had a pointing stability of  $\sim 35\%$ . This was observed at higher temperatures and is due to air convection from the cooler lab temperatures and the heated sample. Because of the thermal convection, the beam centroid was averaged for over 88,000 images (45 minutes time average for each data point) in order to drop the error in  $\Delta x$  measurement down to a maximum of  $\pm 1.2\%$ . This measurement can be improved by imaging both the zero order and the 1<sup>st</sup> order spots so that the relative displacement can be measured. This would help to normalize out the effects of thermal convection. In addition, the 2<sup>nd</sup> or higher orders can be used to increase sensitivity.

## 6.4 Theoretical Results

The SiC temperature sensor is considered a volume transmission grating therefore standard diffraction grating theory was applied to predict the grating performance. The mechanism for the change in spacing of the grating is thermal expansion, which causes

the grating spacing to expand thus results in the 1<sup>st</sup> order deflected beam to drop back to the 0-order. Initially it was assumed that the thermal coefficient of 6H-SiC would be linear, but it becomes nonlinear when the  $\Delta T$  became too large for the linear approximation. Starting from the thermal coefficient and grating equations the change in grating spacing as a function of temperature,  $\Delta d$ , can be derived. The 6H-SiC grating spacing,  $d$ , is initially 20 $\mu\text{m}$  and changes by<sup>41</sup>

$$\Delta d = \alpha \cdot d \cdot \Delta T \quad \text{Equation 6.1}$$

Here  $\alpha$  is the coefficient of thermal expansion solved once  $\Delta d$  was found experimentally as shown in Figure 6.3. Equation 6.1 was applied to the grating equation as stated in Equation 6.2.<sup>42</sup>

$$m\lambda = d \cdot (\sin(\theta) + \sin(\beta)) \quad \text{Equation 6.2}$$

Here, in Equation 6.2,  $m$  is the order ( $m = 1$ ),  $\beta$  is the input angle into the grating and  $\theta$  is the reflection or transmit angle. The deflection ( $\Delta x$ ) is derived by solving for  $\theta$  in Equation 6.2 for the grating spacing and the change in the grating spacing as a function of temperature.

$$\Delta x = [\tan(\theta) \cdot L] - [\tan(\Delta\theta) \cdot L] \quad \text{Equation 6.3}$$

Where  $L$  is the distance from the grating to the CCD camera and  $\Delta\theta$  is given in Equation 6.3.

$$\Delta\theta = \sin^{-1} \left( \frac{\lambda}{(d + \Delta d)} - \sin(\beta) \right) \quad \text{Equation 6.4}$$

From these equations the  $\Delta x$  can be predicted for each given temperature. Given the experimental  $\Delta x$  the thermal coefficient,  $\alpha$ , can be calculated from backing out  $\Delta d$ . The change in the grating spacing,  $\Delta d$ , is derived from the following equation.

$$\Delta d = \frac{\lambda - \tan^{-1}\left(\frac{x - \Delta x}{L}\right)}{\tan^{-1}\left(\frac{x - \Delta x}{L}\right)} \cdot d \quad \text{Equation 6.5}$$

Where  $x$  is the original deflection before the temperature is increased. The experimental 2<sup>nd</sup> order polynomial thermal coefficient equation ( $\alpha$ ) can now be solved by relating the measured  $\Delta x$  values to derive Equation 6.5. Next,  $\Delta d$  can be substituted into Equation 6.5 and plotted as a function of temperature in Figure 6.4, where a polynomial fit to the trend is applied that is shown in Equation 6.6 below.

$$\alpha = -1.38 \times 10^{-11} \cdot \Delta T^2 + 1.23 \times 10^{-8} \cdot \Delta T + 3.84 \times 10^{-6} \quad \text{Equation 6.6}$$

## 6.5 Experimental Results

The experimental results conclude that a maximum deflection for 399°C (starting from 26.7°C) was 140µm as shown in Figure 6.3 below.

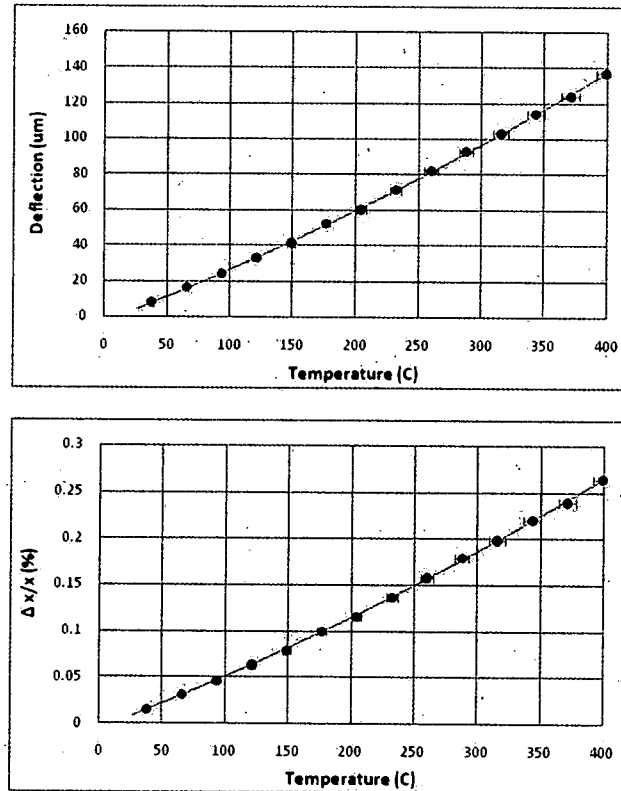


**Figure 6.3:** (Top) shows the deflection ( $\Delta x$ ) as a function of temperature, (bottom) shows the  $\Delta x/x$  ratio as a function of temperature, which is a common way of displaying the material expansion. The charts show a max ~5% error bars.

The error bars for each data point is  $\pm 1.2\%$  maximum as mentioned previously. The 1.2% error bars relate to  $5^\circ\text{C}$  absolute temperature variation. The maximum  $\Delta x$  for 1640mm from the grating is  $140\mu\text{m}$ , which corresponds to  $6.5 \times 10^{-6} \text{ } 1/^\circ\text{C}$  from Equations 53, 54, 58, and shown in Figure 6.4. The percentage of the  $\Delta x/x$  for  $400^\circ\text{C}$  is 0.26%, which corresponds to the same findings of Bhatt *et al.*<sup>43</sup>

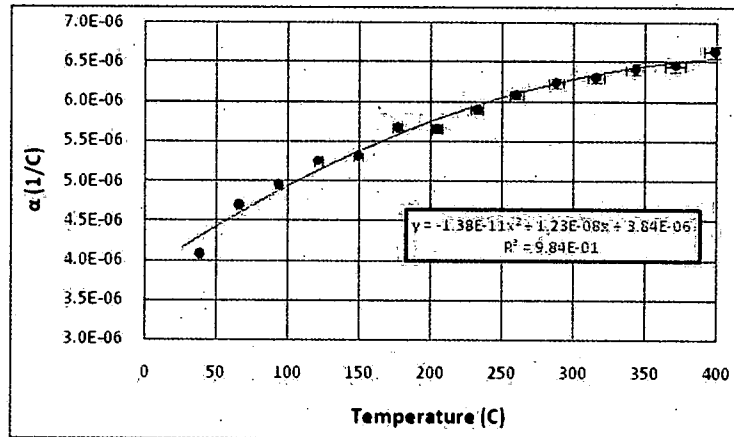


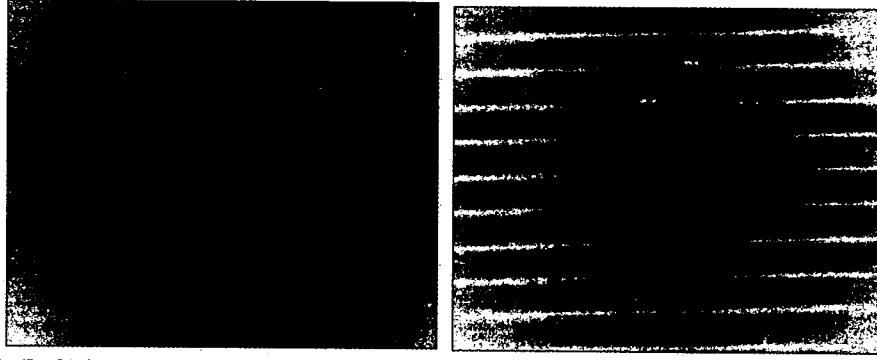
Figure 6.4: Shown here is the 6H-SiC thermal coefficient as a function of temperature with maximum 5% error bars. The 2<sup>nd</sup> order polynomial is given in Equation 49.

Figure 6.4 shows the nonlinear coefficient of thermal expansion as well as the coefficient of linear expansion ( $4.25 \times 10^{-6} \text{ } ^\circ\text{C}^{-1}$  – found by using room temperature thermal expansion) of 6H-SiC, which is in good agreement with Li *et al*, who also found the coefficient of thermal expansion to be a 2<sup>nd</sup> order polynomial trend for 4H-SiC<sup>44</sup> as well as a coefficient of linear expansion of  $4.47 \times 10^{-6} \text{ } ^\circ\text{C}^{-1}$ . In addition to Li *et al*, Talwar<sup>45</sup> *et al* also found a similar trend in the coefficient of thermal expansion plus the coefficient of linear expansion of  $3.5 \times 10^{-6} \text{ } 1/^\circ\text{K}$ .

## 6.6 SiC Volume Phase Grating

Here the 6H-SiC volume phase grating used in this dissertation is illustrated and no change occurred after being annealed up to 399°C. Shown below are optical microscope images of the SiC grating at 10X and 50X.





**Figure 6.5: (Left) is the SiC grating at 10X magnification, and (Right) is the SiC grating after 50X magnification. The images were processed to view easier, and the images were obtained using Nomarski DIC on an optical microscope.**

The 6H-SiC grating above was micro-machined using three anamorphic femtosecond laser lines in series with approximately 10 $\mu$ m of overlap between each anamorphic processed line. Each processed line has 3 $\mu$ m x 190 $\mu$ m dimensions and have a 20 $\mu$ m grating spacing. The overlap of the three lines causes a complex diffraction pattern described using Fourier analysis<sup>46</sup> of this grating convoluted with a Gaussian HeNe beam. The mathematical transmittance function of this grating convoluted with the HeNe beam is shown in Equation 55 below. See the Appendix for a detailed mathematical analysis and for the Matlab code used to generate the theoretical plots.

$$t_a(x, y) = \left[ \left\{ e^{-\pi \left( \frac{x^2}{A^2} + \frac{y^2}{B^2} \right)} + e^{-\pi \left( \frac{(x \pm x_0)^2}{A^2} + \frac{y^2}{B^2} \right)} \right\} \otimes \left[ \left[ \frac{1}{L} \cdot \text{comb} \left( \frac{y}{L} \right) \cdot \delta(x) \right] \cdot \text{rect} \left( \frac{y}{L} \right) \right] \right] \cdot e^{-\pi \frac{r^2}{\omega_0^2}} \quad \text{Equation 6.7}$$

The first two terms in Equation 64 represent the femtosecond micro-machined processed anamorphic lines (3 lines) shifted from x by  $\pm x_0$ , which is convoluted with the grating comb function and multiplied by the HeNe Gaussian function for spot size,  $\omega_0$ . The variables A and B represent the width and length of the processed grating lines, and L is the grating spacing. The rectangular (rect) function represents the grating width and

length dimensions ( $500\mu\text{m} \times 500\mu\text{m}$ ). In summary, the first term sets up the x-dimension anamorphic processed lines, which is convoluted with the repeating processed lines in the y-dimension; the convoluted x and y terms are then multiplied by the HeNe Gaussian term. The femtosecond beam is also represented using a Gaussian function for simplicity, but is actually a secant-squared function. Below gives the theoretical and experimental results of the diffraction pattern as stated above; more details on the Matlab code used for this analysis is presented in the Appendix.

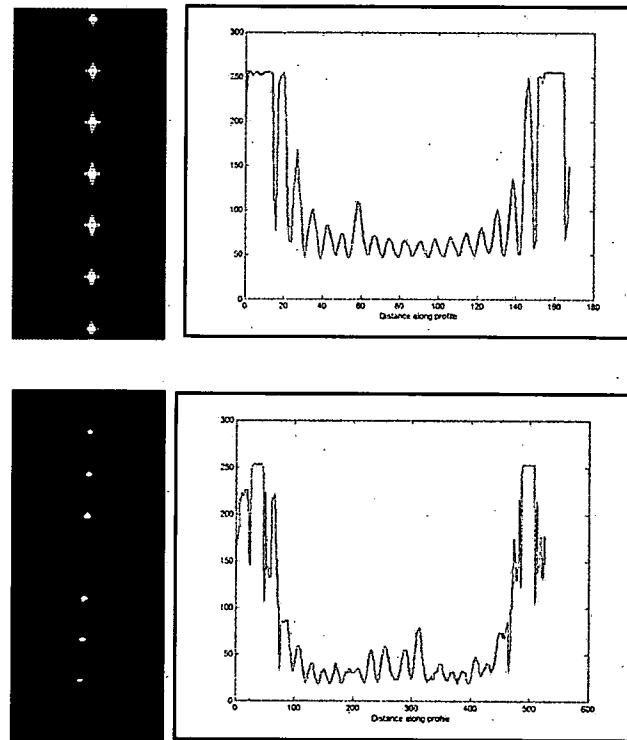


**Figure 6.6: (Above) is the theoretical Fraunhofer diffraction pattern with a lineout of two of the orders, (Below) is the experimental Fraunhofer diffraction pattern with a lineout of two of the orders.**

Figure 6.6 above shows very good agreement with theory and experimental results.

Order spacing and number of minor orders agree, however, the 1<sup>st</sup> and 2<sup>nd</sup> order peaks saturate the CCD camera so it is uncertain if their amplitudes agree, but considering they both saturate and the minor orders agree it can be assumed that they are in close

agreement considering the method of which the data was acquired with a common digital camera. The experimental results were collected using a common digital camera and a lineout performed using Matlab code. From the model the grating structure can be designed to provide the desired diffraction pattern if needed. These results show primarily that the SiC grating structure morphology is understood since the optical microscope may not illustrate or provide enough evidence as to what the structure is exactly. See the Appendix and Section 4.3 Diffraction Efficiency for more details on the Fourier transform of the grating structures.

## **6.7 Conclusion**

In this work we report a new noncontact method of measuring the thermal coefficient of transparent and nontransparent materials using diffraction gratings. This dissertation also reports the measurement of 6H-SiC coefficient of the nonlinear thermal expansion and coefficient of linear expansion. Finally, a new high temperature sensor using gratings micro-machined in 6H-SiC was developed that can be used for high temperatures.

The temperature sensor deflection results can also be improved by adding a lens one focal length away from the stop of the system to create a telescentric or parallel focused beams at the focus plane that representing each order. The lens will then provide an order of magnitude higher resolution, which will increase temperature measurement sensitivity.

Special thanks are given to AFRL personal at WPAFB, the University of Dayton, and Dr. Frank Baxely for assisting in discussions regarding these measurements.

## Appendix

### I. Approximation of $\Delta n$ from Zscan Measurements

To start, the  $\Delta n$  must be compared using similar fluence levels, so with that being said, the fluence chosen from Figure 2.15 is  $0.5 \text{ J/cm}^2$ . In Figure 4.6 (Top) the last data points for the 2 and 6 pulse trends were extrapolated data points done because the damage threshold from using a spherical 125mm lens is approximately 10-times larger for the DT using the anamorphic high-NA lens. So a  $0.5 \text{ J/cm}^2$  DT for the 125mm spherical lens results in a very similar morphology/modulation depth for a  $5.0 \text{ J/cm}^2$  DT with the anamorphic lens. The extrapolation was done by maintaining the 2<sup>nd</sup> order polynomial trend while extrapolating the data point up to  $5 \text{ J/cm}^2$ . The fluence of  $5 \text{ J/cm}^2$  is significant for one reason, that is to compare the  $\Delta n$  diffraction efficiency calculation with the  $\Delta n$  Zscan calculation, which they both closely agree.

Therefore, starting with Equation A.1, the linear index of refraction can be solved and is stated as

$$n_{\text{SiCProcessed}} = \frac{k_2 \cdot \sqrt{21eV}}{n_2 \cdot E_g^4} \cdot G_2 \quad \text{Equation A.1}$$

Since the theoretical  $n_2$  was found to be  $3.6 \times 10^{-6} \text{ cm}^2/\text{GW}$  and the measured was  $4.75 \times 10^{-6} \text{ cm}^2/\text{GW}$  so the difference between theory and measured was used to offset the processed area  $n_2$ . After the offset was taken into account the linear index of SiC processed area,  $n_{\text{SiCProcessed}}$ , was found:  $n_{\text{SiCProcessed}} = 2.594$ . Now, the difference between  $n_{\text{SiC}}$  and  $n_{\text{SiCProcessed}}$  is the  $\Delta n$  for the processed area, which is 0.034. The processed area used for this analysis was  $E_1 = 10 \mu\text{J}$  because this modulation depth is very similar to the

anamorphic processed area for 2 pulses. The other processed areas,  $E_2$  and  $E_3$ , were not giving results as agreeable as the  $E_1$  area since the modulation depth for those areas is unknown and considerably deeper (due to higher energies used). Thus, if the modulation depth was known (with TEM) then the  $\Delta n$  could be determined with the same two methods state in this chapter. Table A.1 summarizes these results.

**Table A.1: Results given for DE, Zscan, and  $\Delta n$  measurements.**

Sample/Processed Area	Modulation Depth ( $\mu\text{m}$ )	$\eta$	$n_2$ ( $\text{cm}^2/\text{GW}$ ) Measured	$\Delta n$ Measured from DE	$\Delta n$ Measured from Zscan	Average $\Delta n$ and % Difference
DE Measured 2 Pulse Grating	0.5	0.47%	-----	0.03	-----	0.032
Zscan Measured $E_1$ Area	$\sim 0.5$	-----	$4.79 \times 10^{-6}$	-----	0.034	12.5%

The results show an acceptable 12.5% difference between the two methods of calculating  $\Delta n$  from the DE and Zscan experiments. In conclusion, the SiC gratings have a modulation depth of  $0.5\mu\text{m}$  and a  $\Delta n$  magnitude of 0.032 on average.

## II. Focus Procedure

Each sample, prior to micromachining, needs to have the precise focus location determined. The following procedures are shown for reflective and transmissive samples.

### Reflective Samples:

For reflective samples the following procedure can be followed:

1. When the sample is not transmissive the focus position is found by use of an optical microscope and using a fluence level just above the DT of the sample under test.

2. As mentioned in number seven of the above section, damage will occur only within the Rayleigh range of the focus, which is between ~20mm and 24mm.

In this range damage will occur and the figure below illustrates this effect.



**Figure A.1: Focus test for a reflective sample with the assistance from an optical microscope to view increasing damage areas that represent focus position.**

3. Knowing how many focal positions and using a starting mark placed on the sample to show the initial shot at the first Z-position you can easily determine the ideal focal position. For transmissive samples the optical microscope is a “sanity check”, but for reflective samples this is the only way to confirm the focal position unless you use and trust SLG results, which would be acceptable for larger Rayleigh ranges.
4. For extremely short Rayleigh ranges (~10-100 microns) a portion of the sample should be sacrificed to confirm your focus location in addition to using an in-situ camera.

### Transmission Samples:

For transmission samples the following procedure is used:

1. Rough align the focusing beam onto a microscope slide (or soda lime glass, SLG) visually with a lens that is mounted on a micrometer stage. In the figure below, either the SLG sample or the lens can be automatically or manually moved through the geometrical focus with the energy constant and using single laser pulses. A single laser pulse is selected with a triggered chopper wheel and shutter combination. The energy is adjusted with the attenuator. The energy is recorded and calibrated with the  $E_{in}$  photodiode and the transmitted energy through the sample is measured using the  $E_{out}$  photodiode.

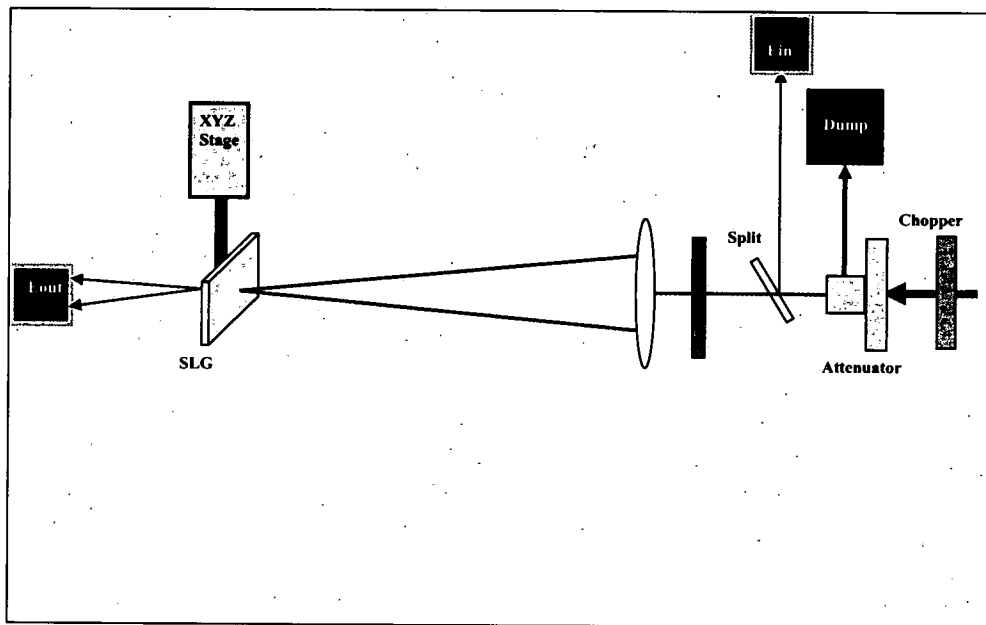


Figure A.2: Transmission focus test setup.

2. Set the micrometer stage past the Rayleigh range by 25-50% before the geometric focus.

3. Using single pulses, translate the sample, or lens, through the focus while recording the input energy,  $E_{in}$ , and output energy,  $E_{out}$ .
4. Plot the  $E_{out}$  versus the Z-position (or focus position) to form a chart given below.

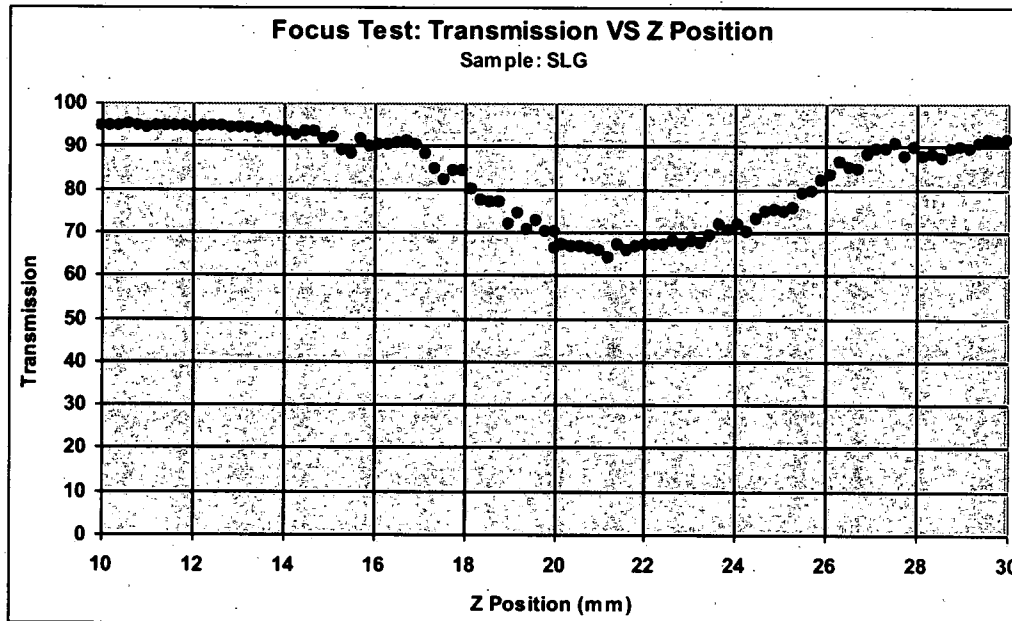


Figure A.3: Transmission test output to give an example of how the transmission (%) will vary as a function of focus distance (Z Position).

5.  $E_{in}$  is used to calculate the fluence because you want to keep the fluence level just above the damage threshold (DT) of the SLG or whatever sample being used.
6. The correct focus position depends on where you want the focus to be:
  - a. If on the surface of the sample choose Z-position to be between 18mm and 20mm (if the sample is in front of the focus initially).
  - b. If in the bulk of the sample choose Z-position to be between 20mm and 24mm (if the sample is in front of the focus initially).



- c. 10mm location is “zero” reading on the lens micrometer and 30mm is the final reading when the sample has moved through focus.
  - d. The Figure 1.4 illustrates the sample moving through the geometrical focus – the red is where the fluence is above the DT and where damage will occur.
7. The chosen Z-position can be verified (“sanity check”) using an optical microscope to confirm damage only when above the DT, which in this case, is from ~20mm to 24mm. An example of the optical microscope is shown below in the next section.

### III. Error Analyses

The error analyses for the DE and the SiC sensor experiments were done using standard error propagation analyses.

#### Diffraction Efficiency Experiment:

The DE experiment uses the previously mentioned DE equation to calculate the diffraction efficiency of the 1<sup>st</sup> order as compared to the zero-order, which also is including the losses due to the SiC sample transmission and Fresnel losses. The transmission and Fresnel reflections were embedded in the measurements of the zero and 1<sup>st</sup> orders so they do not appear in the following equation.

$$\eta = \frac{2 \cdot P_1 \cdot 10^{-(ND_0 - ND_1)}}{P_0} \cdot 100 \quad \text{Equation A.2}$$

Where  $P_1$  is the power emitted from the 1<sup>st</sup> order and  $P_0$  is the power emitted from the zero-order.  $ND_0$  is the neutral density filter(s) used to attenuate the zero-order beam and  $ND_1$  is the filter(s) used to attenuate the 1<sup>st</sup> order beam. The NDs were used to keep the CoHu CCD camera from saturating, thus were accounted for in these measurements. To calculate the uncertainties the following error propagation equations were employed.

For products and quotients:

$$\frac{\delta q}{|q|} = \sqrt{\left(\frac{\delta x}{x}\right)^2 + \left(\frac{\delta y}{y}\right)^2} = \sqrt{\left(\frac{\delta P_1}{P_1}\right)^2 + \left(\frac{\delta P_0}{P_0}\right)^2} \quad \text{Equation A.3}$$

For sums and differences:

$$\delta q = \sqrt{(\delta x)^2 + (\delta y)^2} = \sqrt{(\delta ND_1)^2 + (\delta ND_0)^2} \quad \text{Equation A.4}$$

For powers:

$$\frac{\delta q}{|q|} = x^n = n \frac{\delta x}{|x|} = 1 \frac{\sqrt{(\delta ND_1)^2 + (\delta ND_0)^2}}{10} \quad \text{Equation A.5}$$

The following table presents the uncertainties for each component.

**Table A.2: Uncertainties listed for the DE experimental measured quantities.**

$P_0$	$P_1$	$ND_0$	$ND_1$	Human Error
0.344 mW $\pm 1\%$	0.05mW $\pm 1\%$	3 $\pm 4\%$	2 $\pm 4\%$	$\pm 5\%$
$\pm 0.0084\text{mW}$	$\pm 0.0005\text{mW}$	$\pm 0.12$	$\pm 0.08$	$\pm 0.05$

Thus, the overall DE uncertainty is given below using the table and equations above:

$$\eta = \sqrt{\left(\frac{0.0084}{0.844}\right)^2 + \left(\frac{0.005}{0.05}\right)^2 + \left(\frac{\sqrt{(0.12)^2 + (0.08)^2}}{10}\right)^2} + (0.05)^2 \pm 5.4\% \quad \text{Equation A.6}$$

Therefore, the diffraction efficiency measurements are within  $\pm 5\%$  if a human error of 5% is included. The 5% human error is plausible and is a best guess due to common experimental techniques used.

### SiC Temperature Sensor Experiment:

Using the same equations for the DE experimental uncertainties above (except for the power error propagation) were used to calculate the uncertainties for the measurement of the SiC thermal expansion coefficient. The following table presents the uncertainties for the instruments used in these experiments.

**Table A.3: Uncertainties listed for the SiC temperature sensor experimental measured quantities.**

Omega Temp. Controller	HeNe Pointing Error	Centroid Measured Time	Centroid Measured Images	Human Error
$\pm 1^\circ\text{C}$	$\sim 35\%$ maximum	45 minutes	88,000	$\pm 5\%$
-----	$\pm 0.35$	-----	-----	$\pm 0.05$

As previously mentioned, the temperature was measured and controlled with an Omega temperature controller CN7800 that has  $\pm 1^\circ\text{C}$  resolution. Due to convection caused from the laboratory temperature, the 1<sup>st</sup> order deflected HeNe beam had a pointing stability of  $\sim 35\%$ . This was observed at higher temperatures and is due to air convection from the cooler lab temperatures and the heated sample. Because of the thermal convection, the beam centroid was averaged for over 88,000 images (45 minutes time

average for each data point) in order to drop the error in  $\Delta x$  measurement down to a maximum of  $\pm 1.2\%$ ; as shown below:

$$\frac{\delta q}{|q|} = \sqrt{\left(\frac{(3065)(35.3\%)^2}{88,000}\right)} = 1.2\% \quad \text{Equation A.7}$$

Here, 3065 is the centroid position of the 1<sup>st</sup> order diffracted beam at 400°C, and 35.3% is the combination of the 35% laser pointing stability and 5% human error.

The error also decreased as the temperature increased. This was because at lower temperatures the SiC was more affected by the laboratory convection currents, which made the 1<sup>st</sup> order diffracted beam, have a more unstable pointing stability. In other words, the amount the 1<sup>st</sup> order beam deviated from nominal was small at lower temperatures thus the deviation error was a significant amount. Therefore, as mentioned, the decreasing error as a function of temperature is shown below.

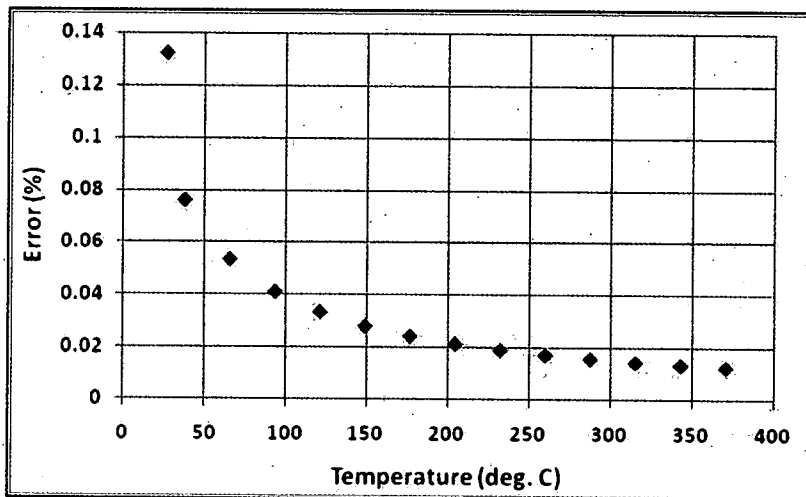


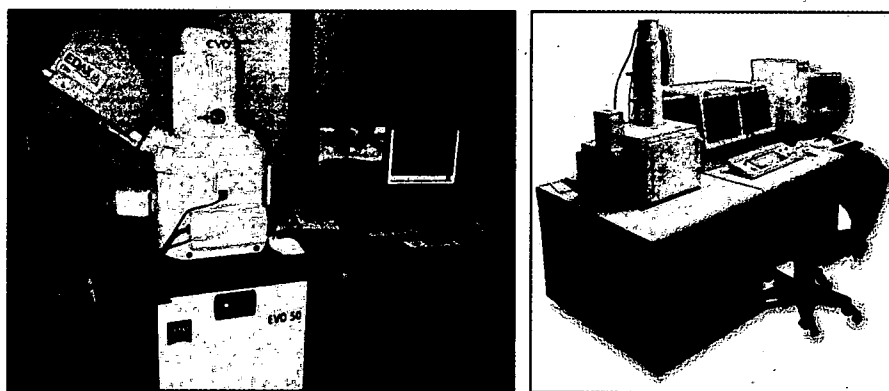
Figure A.4: Chart of how the measured error for the coefficient of thermal expansion decreases as a function of temperature.

Figure A.4 shows how the maximum error, 0.14%, decreases to ~0.015% once the temperature reaches 400°C. At the higher temperatures, the  $\Delta x$  of the 1<sup>st</sup> order diffracted beam is greater resulting in a more accurate measurement using the Cohu 4812 CCD camera and the Spiricon laser beam analyzer software that is used to record the beam centroid position in microns.

#### **IV. Energy Dispersive X-Ray Spectroscopy (EDS or EDAX) & Scanning Electron Microscope (SEM)**

In the absence of SIMS and in hopes that Energy Dispersive Spectroscopy (EDS) system will provide some indication of the chemical makeup of the SiC processed “dome”, EDS was performed. Unfortunately, the FIB milled area of the sample was too small and there was no way of knowing exactly what area was being probed by the EDS x-ray beam.

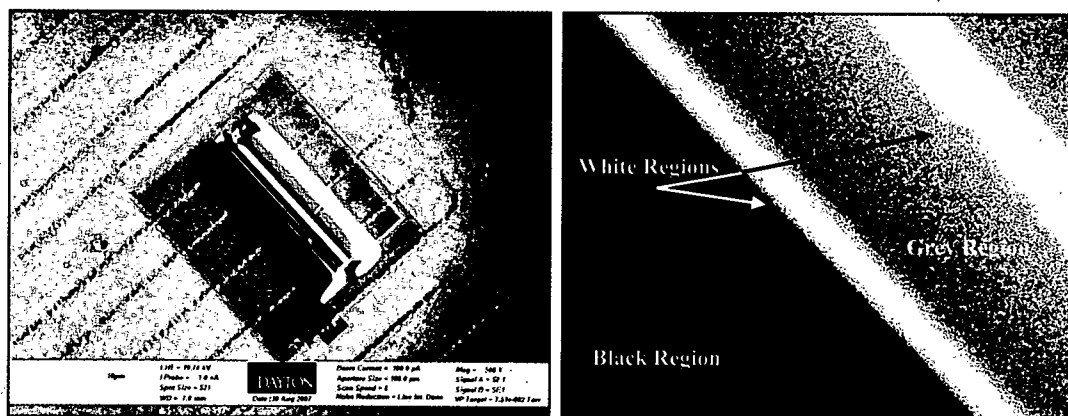
However, data was collected and will be presented here.



**Figure A.5: University of Dayton EDS system (Left) and SEM system (Right).**

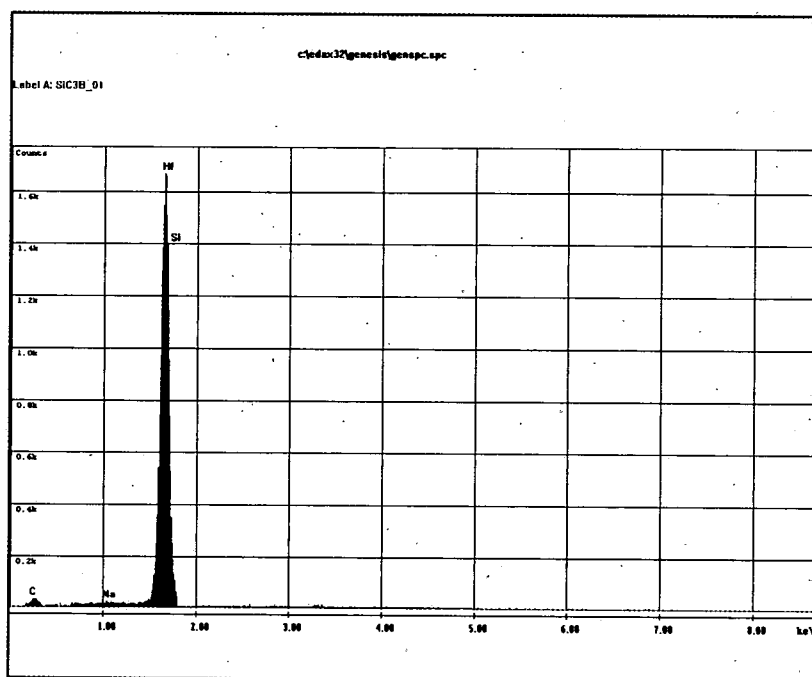
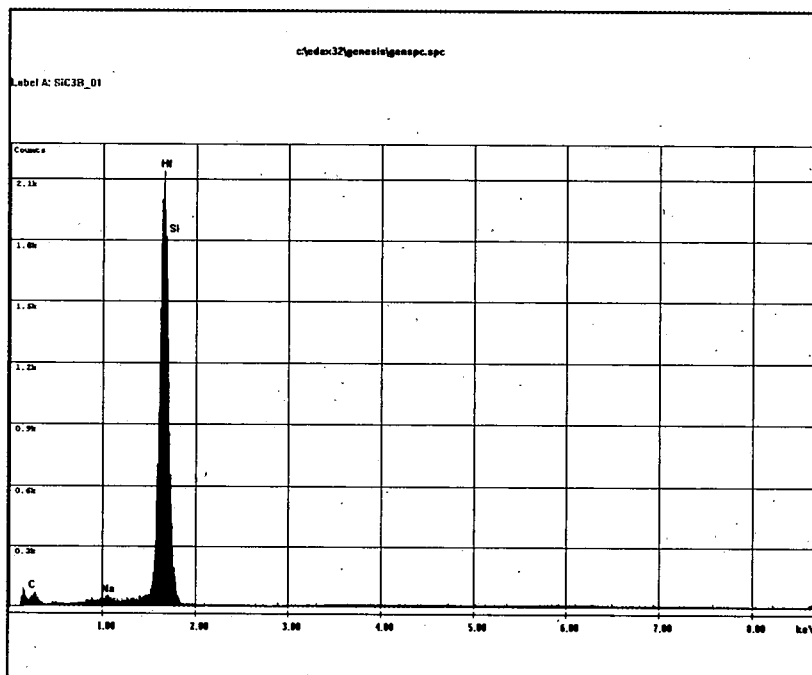
EDS systems include an x-ray detector, liquid nitrogen to cool the detector for sensitivity improvement (increase the signal to noise), software to collect and analyze the spectra. The detector and specimen are mounted in liquid nitrogen cooled chamber where the x-ray beam enters and radiates the specimen.

The data collected was taken on the following areas:



**Figure A.6: University of Dayton NEST Laboratory SEM (Left) and EDS (Right) images.**

Figure A.6 depicts the area of EDS processing. On the left is a SEM image showing the semi-insulating SiC grating lines with a FIB milled area done for the TEM data. On the right is an image provided by the EDS imager, which is used to direct the x-ray beam at the targeted area. In the EDS image, four areas were analyzed: the black region, the gray region, and two white regions. The white regions gave the same results so only one set of data will be shown.



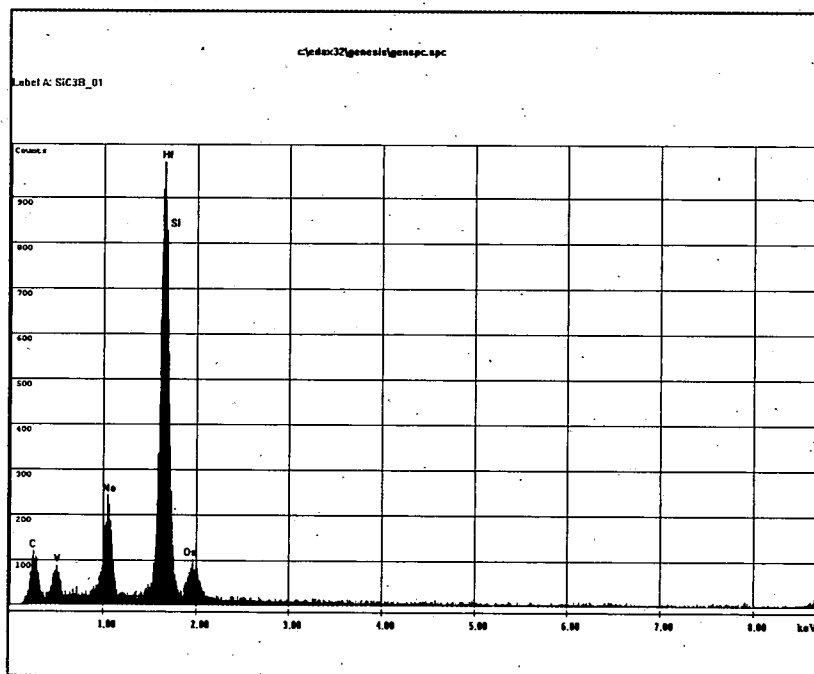


**Figure A.7: University of Dayton EDS results on the black (Top), gray (Middle), and white (Bottom) regions.**

Figure A.7 gives the results of the EDS spectroscopy. Table A.4 explains the elements found in the SiC processed areas.

**Table A.4: Elements found in the EDS black, gray, white regions.**

Region	Carbon	Vanadium	Sodium	Hafnium	Silicon	Osmium
Atomic Weight	12.011	50.9415	22.98977	178.49	28.0855	190.2
Common Uses	Fuel, Lubricant	V <sub>2</sub> O <sub>5</sub> catalyst, Tool steel	Lamps, Table salt	Nuclear control rods	IC, glass, Lubricant	Alloys, Phono. needles
Black	C	----	Na	Hf	Si	----
Gray	C	----	Na	Hf	Si	----
White	C	V	Na	Hf	Si	Os

Table A.4 gives the elements in each region. Carbon and silicon exist in each region, which is to no surprise. The EDS software assigns the most likely elements



corresponding to the spectra peaks, therefore, there is some question as to if the assigned elements are correct. Table A.4 also gives some common uses of these elements, which helps to identify if the EDS software assignments make sense – sort of a sanity check.

The known elements are silicon, carbon, sodium, hafnium, osmium, and vanadium. It is known that vanadium is used as part of the TEM FIB milling process, and sodium is also used in the FIB process to help purify molten metal (vanadium) and to improve alloy structures. Sodium may also have been used in cleaning the SiC sample during preparations. Osmium is also an alloy, which may explain its presence along with vanadium. The TEM process typically uses a platinum cap that uses osmium as an alloy, but knowing that vanadium is used and platinum presence was not found this suggests that it is a vanadium alloy. Finally, osmium is only found in the white regions where it is known that vanadium TEM prep material is located. Plus, there is a very low amount of osmium so it is not a concern. This brings us to hafnium, which is probably a mistake on the EDS software part since hafnium is common used as a nuclear reactor control rod material. Considering that the Hf peak is so close, if not the same, as to the Si peak it is assumed that this peak is actually the Si peak.

Therefore, the EDS results basically show that SiC is present along with the metallic materials used to FIB the sample for TEM preparation. There are two conclusions that are the same as the x-ray conclusions that are stated:

1. EDS data is only showing the bulk SiC and it does not have enough resolution to provide any information on what other elements may be within the processed regions

2. The processed SiC regions consist only of Si and C, which supports the x-ray crystallography, TEM, and Raman findings. Recall that the TEM results on the subsurface gratings only show SiC exist (no significant silicon and carbon separation) and a reconstruction of the SiC crystal has occurred owing to the SiC dipoles in new locations. Also recall that the Raman spectrum of the processed SiC had subtle differences in shifts and broadening. There does not seem to be any new elements or containments during the femtosecond micromachining process according to the EDS results.

The above EDS results provide support to other experiments even though the data itself is questionable due to the accuracy of the beam during the measurement process.

Nevertheless, these results hold some value and will be considered in the overall analysis of what the physical cause of the index of refraction modification in SiC crystal.

## V. Publications

- **Refereed Papers:**

- Institute of Physics:
  - **"High Power Large Bore CO<sub>2</sub> Laser Small Signal Gain Coefficient and Saturation Intensity Measurements"**
  - *Journal of Optics A: Pure Appl. Opt.* 5 96-101
- Optics Express:
  - **"Femtosecond micromachining in transparent bulk materials using an anamorphic lens"**
  - *Optics Express, Vol. 15, Issue 20, pp. 13139-13148*
- JOSA B
  - **"Femtosecond Laser Damage Threshold and Nonlinear Characterization in Bulk Transparent SiC Materials"**
  - *JOSA B, Vol. 25, Issue 1, pp. 60-66*
- Applied Optics – in review
  - **"Optical temperature sensor and thermal expansion measurement using a femtosecond micro-machined grating in 6H-SiC"**
  - *In Review*

- **Presentations:**

- SPIE:
  - Great Lakes 2006
    - **"Novel Material Processing Using Ultrafast Laser Technology"**
    - *Dayton Convention Center 2006.*
  - Photonics West 2008
    - **"Femtosecond Laser Damage Threshold and Nonlinear Characterization in Bulk Transparent SiC Materials"**
    - *Paper 6875-61 of Conference 6875*
  - IEEE 2003
    - **"Research and development of an integrated electro optical and radio frequency aperture"**
    - *Aerospace Conference, 2003. Proceedings. 2003 IEEE Volume 2, Issue , 5-12 March 2005 Page(s): 2\_987 - 2\_995*

## REFERENCES

- 1 Petite, G., Daguzan, P., Guizard, S., & Martin, P., "Femtosecond history of free carriers in the conduction band of a wide-bandgap oxide," 40-44, (1995).
- 2 An-Chun Tien, S. B., "Short-Pulse Laser Damage in Transparent Materials as a Function of Pulse Duration," *Phys. Rev. Lett.*, **82**, 3883 – 3886, (1999).
- 3 T. Norris, A. Galvanauskas, University of Michigan, Center for Ultrafast Optical Science, <http://www.eecs.umich.edu/CUOS/index.html?http://www.eecs.umich.edu/USL/HERCULES/index/index.html>, (2008).
- 4 P. Bado, W. Clark, A. Said, "Introduction to Micromachining," Clark-MXR, [www.clark-mxr.com](http://www.clark-mxr.com), (2007).
- 5 Wright-Patterson AFB (WPAFB) Air Force Research Laboratory/Materials and Manufacturing Directorate (AFRL/MLPS), WPAFB, OH 45433, 937-255-2227.
- 6 J. Copper, Purdue University College of Engineering: Purdue Wide Band Gap Semiconductor Device Research Program, <http://www.ecn.purdue.edu/WBG/Index.html>, (2004).
- 7 M. Dong, "Femtosecond Pulsed Laser Ablation of 3C-SiC Thin Film on Silicon", *Appl. Phys. A*, **77**, No. 6, 839-846, (2003).
- 8 Shaffer, P., "Refractive index, dispersion, and birefringence of silicon carbide polytypes," *Appl. Opt.* **10**, 1034-1036, (1971).
- 9 Z. Li, R. Bradt, "Thermal Expansion of the Hexagonal (4H) Polytype of SiC," *J. Appl. Phys.*, **60**, 612-614 (1986).
- 10 D.N. Talwar, J.C. Sherbondy, "Thermal expansion coefficient of 3C-SiC," *Appl. Phys. Lett.*, **67**, 3301-3303, (1995).
- 11 Specialty Glass Products, <http://www.sgpinc.com/sodalime.htm>, (2008).
- 12 P. Chappl, J. Staromlynka, J. Herman, T. McKay, R. McDuff, "Single-Beam Z-scan: Measurement Techniques and Analysis", *Journal of Nonlinear Optical Physics and Materials*, **6**, 251-293, (1997).
- 13 Mansoor Sheik-Bahae, Ali A. Said, Tai-Huei, Wei, David J. Hagan, E. W. Van Stryland, "Sensitive Measurement of Optical Nonlinearities Using a Single Beam," *IEEE Journal of Quantum Electronics*, **26**, 760-769, (1990).
- 14 M. Yin, H. P. Li, S. H. Tang, W. Ji, "Determination of Nonlinear absorption and Refraction by Single Z-scan Method," *Appl. Phys. B*, **70**, No. 4, 587-591, (2000).
- 15 Mansoor Sheik-Bahae, Ali A. Said, Tai-Huei, Wei, David J. Hagan, E. W. Van Stryland, "Dispersion of Bound Electronic Nonlinear Refraction in Solids," *IEEE Journal of Quantum Electronics*, **27**, 1296-1309, (1991).
- 16 M. Yamane, A. Yoshiyuki, "Glasses for Photonics," Cambridge University Press, ISBN: 0521580536 174-176, (2000).
- 17 J. Ashcom, C. Schaffer, E. Mazur, "Numerical Aperture Dependence of Damage and Supercontinuum from Femtosecond Laser Pulses in Bulk Fused Silica," *J. Opt. Soc. Am. B*, **23**, 2317-2322, (2006).

- 
- 18 J. T. Verdeyen, "Laser Electronics", 3<sup>rd</sup> Edition, Prentice Hall, Inc., (1995).
- 19 M. Lenzner, J. Kruger, S. Sartania, Z. Cheng, Ch. Spielmann, G. Mourou, W. Kautek, F. Krausz, "Femtosecond Optical Breakdown in Dielectrics," *Physical Review Letters*, **80**, No. 18, 4076-4079, (1998).
- 20 K. Zagorulko, P. Kryukov, Y. Larionov, A. Rybaltovsky, E. Dianov, "Fabrication of Fiber Bragg Gratings with 267nm Femtosecond Radiation," *Optics Express*, **12**, 5996-6001, (2004).
- 21 C. Palmer, "Diffraction Grating Handbook fourth edition," Richardson Grating Laboratory, [www.gratinglab.com](http://www.gratinglab.com), Rochester, NY, (2000).
- 22 S. Barden, J. Arns, W. Colburn, J. Williams, "Volume-Phase Holographic Gratings and Efficiency of Three Simple Volume-Phase Holographic Gratings," *Publications of the Astronomical Society of the Pacific*, **112**, 809-820, (2000).
- 23 Chan, Huser, Risbud, Krol, "Structural Changes in Fused Silica After Exposure to Focused Femtosecond Laser Pulses," *Optics Letters*, **26**, No. 21, (Nov. 2001).
- 24 J. Burton, L. Sun, M. Pophristic, S. Lukacs, F. Long, Z. Feng, I. Ferguson, "Spatial Characterization of Doped SiC Wafers by Raman Spectroscopy," *Journal of Applied Physics*, **84**, 6268-6273, (1998).
- 25 M. Alonso, K. Winer, "Raman Spectra of c-Si<sub>1-x</sub>Ge<sub>x</sub> Alloys," **39**, 10056-10062, (1989).
- 26 C. Tsai, C. Lin, J. Lin, J. Wang, "Vibrational Dephasing Dynamics of the Hydrogenated Si(100)-2x1 Surface Revisited: Multi-Mode Dephasing Model," **295**, 509-515, (1998).
- 27 NSC University, "Micro Physics," [http://www.micro.physics.ncsu.edu/raman\\_measurements.htm](http://www.micro.physics.ncsu.edu/raman_measurements.htm), (2008).
- 28 D. McCamant, P. Kukura, R. Mathies, "Corethane, Femtosecond Time-Resolved Stimulated Raman Spectroscopy: Application to the Ultrafast Internal Conversion in B," **107**, 8208-8214, (2003).
- 29 J. Kress, A. rose, J. Frey, W. Brocklesby, M. Ladlow, G. Mellor, M. Bradley, "Site Distribution in Resin Beads as Determined by Confocal Raman Spectroscopy," **7**, 3880-3883, (2001).
- 30 A. Arencibia, M. Taravillo, F. Perez, J. Nunez, V. Baonza, "Effect of Pressure on Hydrogen Bonding in Liquid Methanol," **89**, 1955041-1955044, (2002).
- 31 A. Kasuya, Y. Sasaki, Y. Saito, K. Tohji, Y. Nishina, "Evidence for Size-Dependent Discrete Dispersions in Single-Wall Nanotubes," **78**, 4434-4437, (1997).
- 32 Z. Feng, S. Chua, K. Tone, J. Zhao, "Recrystallization of Carbon-Aluminum Ion Coimplanted Epitaxial Silicon Carbide - Evidenced by Room Temperature Optical Measurements," **75**, 472-474, (1999).
- 33 R. Paschott, "Encyclopedia of Laser Physics and Technology," [http://www.rp-photonics.com/brillouin\\_scattering.html](http://www.rp-photonics.com/brillouin_scattering.html), (2008).
- 34 C. Kittel, "Introduction to Solid State Physics," Wiley and Sons, Inc., 4<sup>th</sup> edition, 673-675, (1969).
- 35 JPK Instruments, "Tutorial for Scanning Probe Microscopy in Life Science," <http://www.jpk.com/tutorial/afm.htm>, (2008).

- 
- 36 S. Mao, F. Quéré, S. Guizard, X. Mao, R. Russo, G. Petite, P. Martin, "Dynamics of Femtosecond Laser Interactions with Dielectrics," *Appl. Phys. A*, **79**, No. 7, 1695-1709, (2004).
- 37 Nanonics Imaging, Ltd., [http://www.nanonics.co.il/index.php?page\\_id=149A](http://www.nanonics.co.il/index.php?page_id=149A), (2008).
- 38 P. Goodhew, University of Liverpool, <http://www.matter.org.uk/tem/default.htm>, (2008).
- 39 L. DesAutels, C. Brewer, M. Walker, S. Juhl, M. Finet, P. Powers, "Femtosecond micromachining in transparent bulk materials using an anamorphic lens," *Optics Express*, **15**, 20, 13139-13148 (2007).
- 40 J. Copper, Purdue Wide Band Gap Semiconductor Device Research Program, <http://www.ecn.purdue.edu/WBG/Index.html>, Purdue University College of Engineering.
- 41 R. Serway, "Physics For Scientists & Engineers," 3<sup>rd</sup> edition, 513-515, (1999).
- 43 R.T. Bhatt, A.R. Palczer, "Effects of Thermal Cycling on Thermal Expansion and Mechanical Properties of SiC Fiber-Reinforced Reaction-Bonded Si<sub>3</sub>N<sub>4</sub> Composites," NASA Technical Memorandum 106665/Army Research Laboratory, 1-15, (1994).
- <sup>44</sup> Z. Li, R. Bradt, "Thermal Expansion of the Hexagonal (4H) Polytype of SiC," *J. Appl. Phys.*, **60**, 2, 612-614, (1986).
- 45 D.N. Talwar, J.C. Sherbondy, "Thermal expansion coefficient of 3C-SiC," *Appl. Phys. Lett.* **67**, 22, 3301-3303, (1995).
- 46 J.W. Goodman, "Introduction to Fourier Optics," Roberts and Company, ISBN 0-9747077-2-4, (2005).

R702034174